1506
UNIVERSITÀ
DEGLI STUDI
DI URBINO
CARLO BO

Università degli Studi di Urbino Carlo Bo
Dipartimento di Scienze Pure e Applicate

Corso di Dottorato di Ricerca in: Scienze di Base e Applicazioni
Curriculum: Scienza della complessità
Ciclo: XXXIV
Settore Scientifico Disciplinare: FIS01

Coating Thermal Noise Issue for Gravitational-Waves Detectors

Coordinatore:

Chiar.mo Prof. Alessandro Bogliolo

Supervisore:

Chiar.mo Prof. Filippo Martelli

Dottorando:

Dott. Matteo Bischi

Anno Accademico 2020/2021

Coating Thermal Noise Issue for Gravitational-Waves Detectors

Matteo Bischi

March 23, 2022

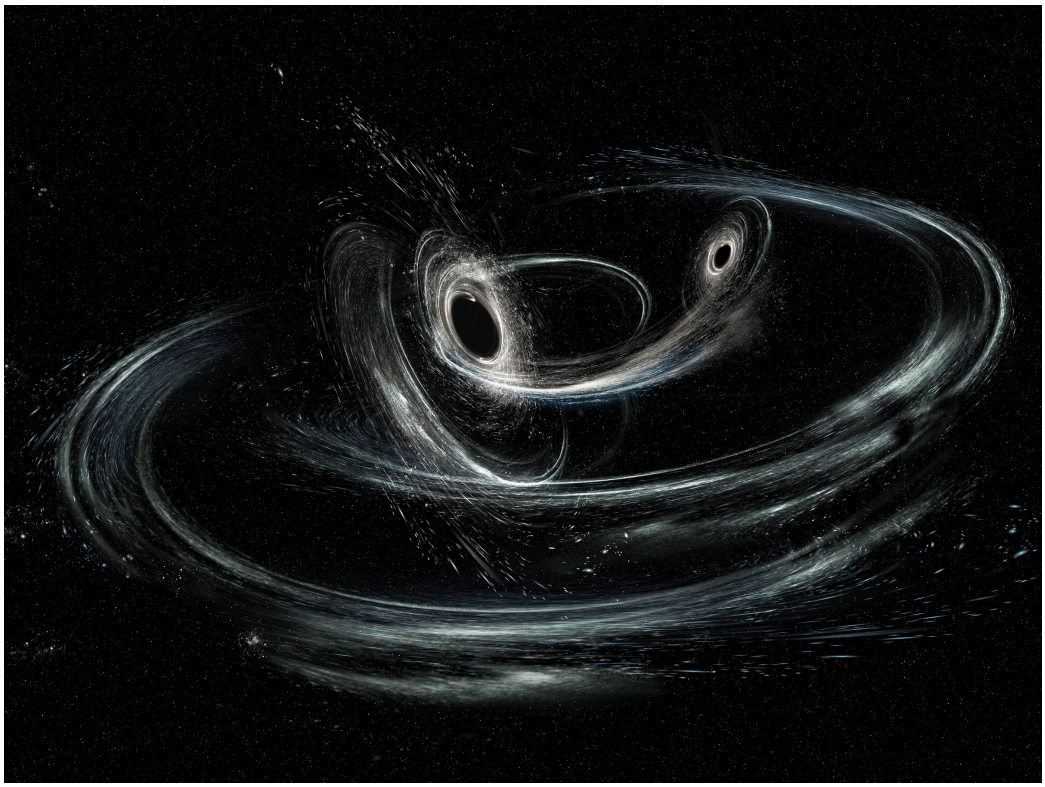

Figure 1: Aurore Simonnet, LIGO, Sonoma State University.

"The most important motive for work in school
and in life is pleasure in work, pleasure in its result
and the knowledge of the value of the result to the community."

Albert Einstein

Contents

Acknowledgements

First af all, I would like to express my gratitude to my supervisor – Dr. Filippo Martelli – for his support and feedback during the course of my PhD studies. Special thanks to Dr. Gianluca M. Guidi, Dr. Francesco Piergiovanni, Dr. Matteo Montani and Dr. Federica Fabrizi for their assistance at every stage of the research project and for making me independent in my work.

Additionally, I would like to express gratitude to Dr. Massimo Granata and Dr. Gianpietro Cagnoli (Geppo) for their support and advices, which were really influential in shaping my experimental methods.

I would like to extend my sincere thanks to Andri M. Gretarsson and Gabriele Vajente for their hospitality and precious teachings during my stay at the Embry-Riddle Aeronautical University (Prescott, Arizona) and at Caltech (Pasadena, California), respectively.

Of course, I am solely responsible for any inaccuracies included in this thesis.

Introduction

"We are just an advanced breed of monkeys
on a minor planet of a very average star.
But we can understand the Universe.
That makes us something very special."

Stephen Hawking
Der Spiegel Magazine, 1988

In 1916 Albert Einstein published the general theory of relativity [1], that generalizes special relativity and refines Newton's law of universal gravitation contained in *Philosophiae Naturalis Principia Mathematica*, first published in 1687 [2]. In General Relativity (GR) the idea of a gravitational force propagated between massive bodies is replaced by the idea that gravitation is a manifestation of curved spacetime.

According to GR, the spacetime can be distorted by the presence of massive objects and the resulting curvature of spacetime influences the motion of massive bodies within it. This behaviour is summed up by John Wheeler in 12 words: *"Space-time tells matter how to move; matter tells space-time how to curve"* [3]. From a mathematical point of view, this concept is summarized by the famous Einstein's field equation:

$$R_{\mu\nu} - \frac{1}{2}Rg_{\mu\nu} = \frac{8\pi G}{c^4}T_{\mu\nu} \tag{1}$$

where $R_{\mu\nu}$ is the Ricci tensor, R is the Ricci scalar, $g_{\mu\nu}$ is metric tensor, G is the gravitational constant, c is the speed of light and $T_{\mu\nu}$ is the energy-momentum tensor.

In 1916 Einstein also predicted the existence of metric deformation waves, called *gravitational waves* (GW) travelling at the speed of light and originated by mass acceleration, but a lot of scientists, including Einstein himself, were doubtful about the result.

A first indirect experimental proof of the existence of GW was provided in 1974 by the observation of the binary system PSR 1913+16 [4]. PSR 1913+16 includes a pulsar orbiting at high speed in the gravity field of a dark companion. According to GR, the system should emit gravitational radiation and loose energy. As a consequence, the orbital period P should progressively decay over time ($\dot{P} < 0$). This prevision is not in agreement with classical physics, where the orbital period is a constant of the motion ($\dot{P} = 0$). In Figure 2 the variation of the orbital period of the binary system PSR 1913+16 is compared with the prediction of GR and classical physics (the parabola and the line of zero orbital decay respectively).

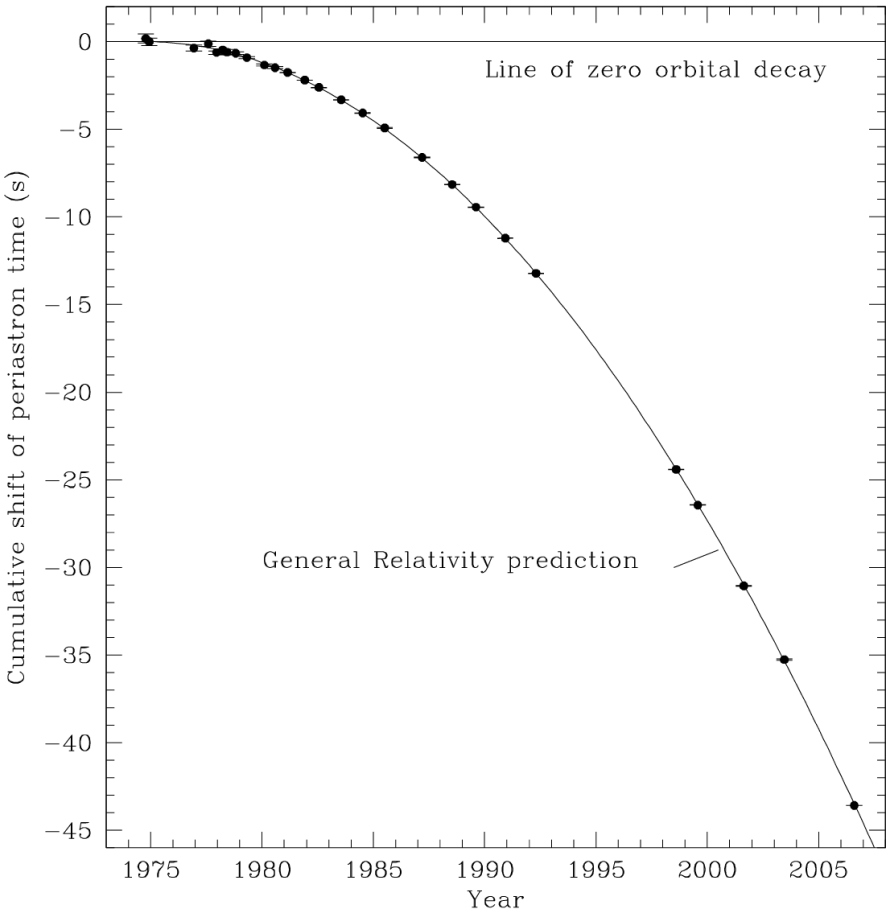

Figure 2: Time variation of the orbital period of the binary system PSR 1913+16. Dots represent measured variations, the curved line represents the expected orbital decay caused by the loss of energy by gravitational radiation and the horizontal line represents zero orbital decay as predicted by classical physics [5].

Direct observation of GW was not possible for many decades after they were predicted due to "vanishingly small" amplitude. A technique called interferometry was suggested in the 1960s to overcome this problem and the technology improved sufficiently to become feasible. A first direct observation of GW from a black-hole binary (BBH) was recorded in September 2015 [6]. This detection was possible thanks to the development of three giant ground-based interferometers in USA and Italy. Two twins Laser Interferometer Gravitational-Wave Observatory (LIGO) are operating in USA and another one, Virgo, is operating in Italy. Signals observed by two interferometers (Hanford and Livingston) are reported in Figure 3.

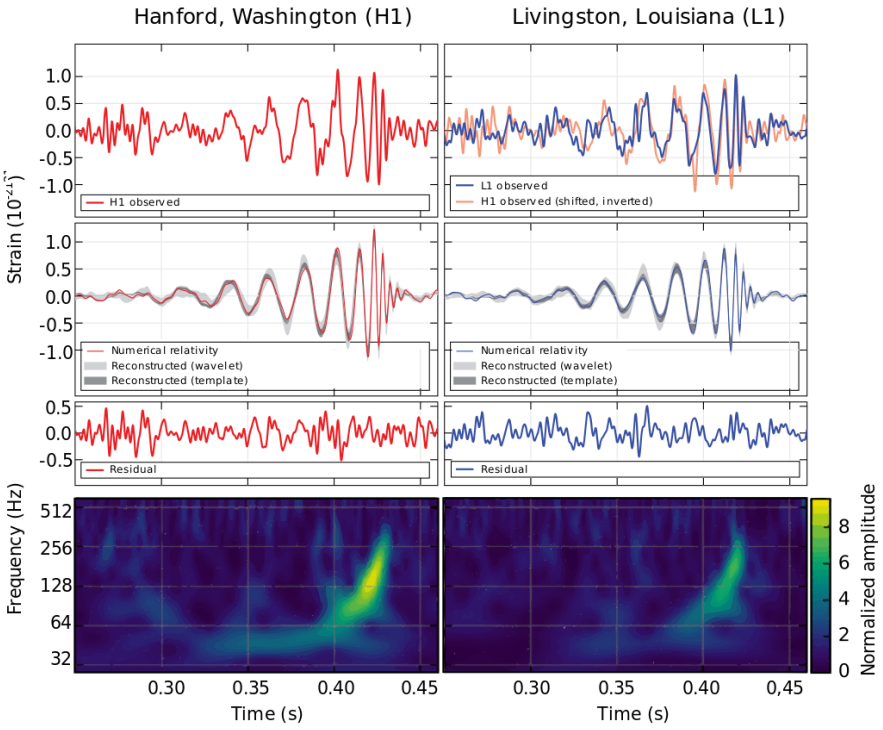

Figure 3: The first GW event (GW150914) observed by the LIGO Hanford (H1, left column panels) and Livingston (L1, right column panels). **Top row:** strain vs time graph. **Second row:** numerical relativity waveform for a system with parameters consistent with those recovered from GW150914. Shaded area show 90% credible regions for two waveform reconstructions. **Third row:** residuals obtained subtracting the graph on the second row (numerical relativity waveform) to the graphs on the first raw (strain waveform) **Bottom row**: time-frequency representation of the strain data [6].

During the first three observing runs, the LIGO/Virgo collaboration detected a lot of GW signals from BBH, Binary neutron stars (BNS) and objects of uncertain nature [7]. As an example, a summary of the signals detected in the first and second observing runs is shown in Figure 4.

One of the main goals of the LIGO-Virgo collaboration is to improve the sensitivity of each interferometer, enhancing the amplitude of the observable universe. One of the limiting noise sources is the so-called coating thermal noise (CTN) that affects the most sensitive region of the detection band (around 100 Hz). This thesis is focused on the CTN reduction, studying and testing the properties of alternative materials for the upgrade of existing interferometers and for the next generation of interferometers.

Outline of the Thesis

- **Chapter 1:** a brief introduction to GW theory and possible astrophysical sources.
- **Chapter 2:** description of the layout of a ground-based interferometer for GW detection and a brief overview of the noise sources that limit their sensitivity.
- **Chapter 3:** a deeper focus on thermal noise, that affects the most sensitive region of the detection band.
- **Chapter 4:** a description of experimental facilities that have been built in the Urbino Laboratory during my PhD period.
- **Chapter 5:** experimental results obtained using the facilities described in the previous chapter, divided in different research lines.
- **Chapter 6:** finite element analysis carried on during a visiting period at Caltech, to understand the impact on experimental results of different holders during the coating deposition.
- **Conclusions**

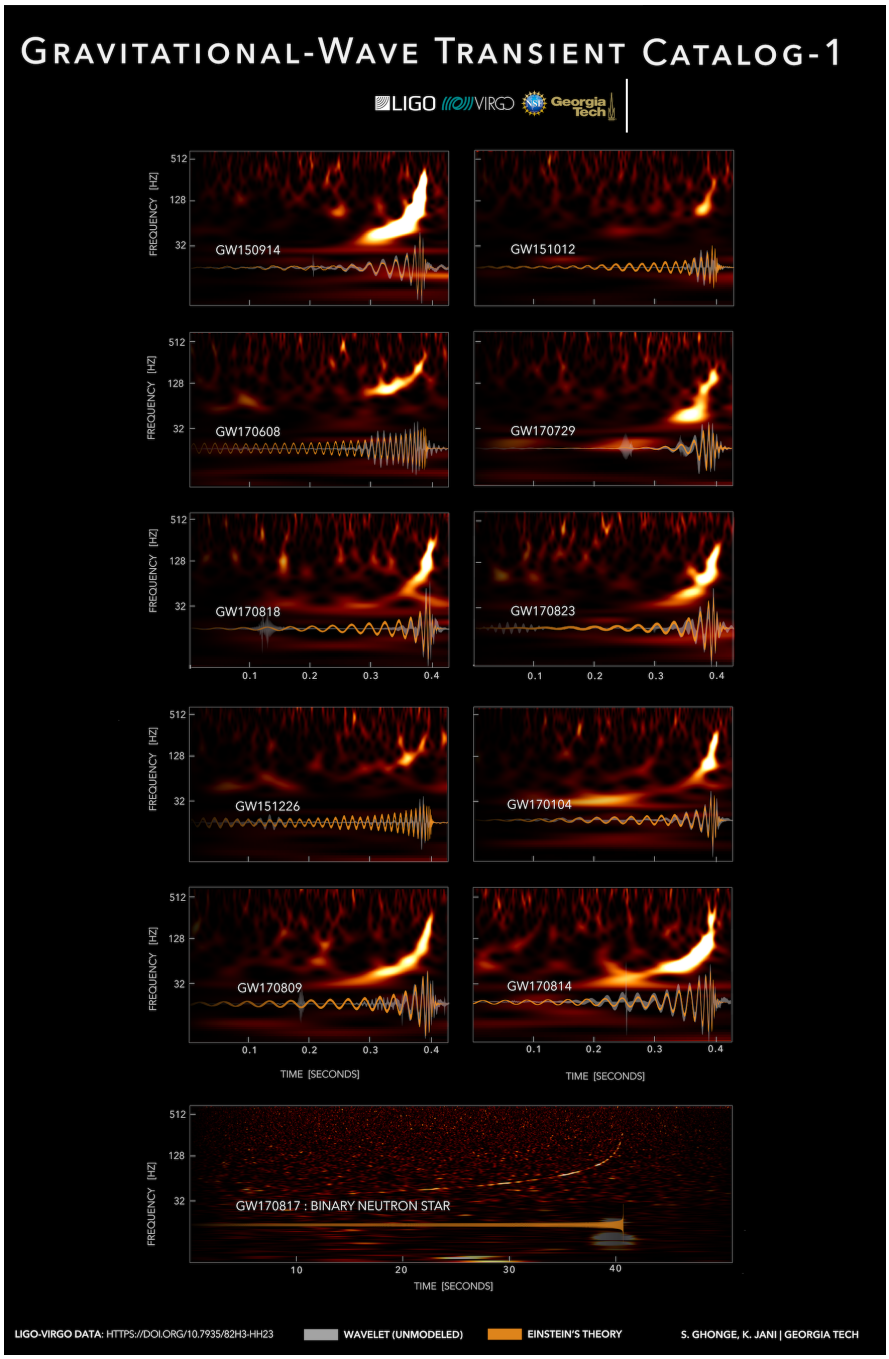

Figure 4: Time-frequency maps and reconstructed signal waveforms for ten BBH events and one BNS event detected during the first and second observing runs. The spectrogram colour indicates a measure of signal strength [8].

Chapter 1

Gravitational-Waves

"Look deep into nature,
and then you will understand everything better."

Albert Einstein

1.1 From General Relativity to the Gravitational-Wave Equation

According to relativity, the maximum speed of propagation for a signal is the speed of light c. Therefore, a variation of the curvature of the space-time does not change instantaneously at arbitrary distance, but the information is carried at the speed of light.

A fundamental concept is that the space-time interval ds between two events is given by:

$$ds^2 = g_{\mu\nu} dx^\mu dx^\nu \tag{1.1}$$

where $g_{\mu\nu}$ is the metric tensor and contains all of the informations about space-time curvature.

Starting from a simple special case, with a flat space-time described by the Minkowski metric $\eta_{\mu\nu}$ given by (in Cartesian coordinates):

$$g_{\mu\nu} = \eta_{\mu\nu} = \begin{bmatrix} -1 & 0 & 0 & 0 \\ 0 & 1 & 0 & 0 \\ 0 & 0 & 1 & 0 \\ 0 & 0 & 0 & 1 \end{bmatrix} \tag{1.2}$$

$$ds^2 = \eta_{\mu\nu} dx^\mu dx^\nu = -c^2 dt^2 + dx^2 + dy^2 + dz^2 \tag{1.3}$$

and adding a small perturbation $h_{\mu\nu}$, it is possible to write the metric in the form:

$$g_{\mu\nu} = \eta_{\mu\nu} + h_{\mu\nu}, \qquad |h_{\mu\nu}| << 1 \tag{1.4}$$

Considering useful gauge (called *harmonic gauge*), the weak field limit of Einstein's field equation becomes a wave equation:

$$\left(\bigtriangledown^2 - \frac{1}{c^2} \frac{\partial^2}{\partial t^2} \right) h_{\mu\nu} = 0 \tag{1.5}$$

which describes a plane-wave travelling at the speed of light. A general solution for equation 1.5 can be written in the form:

$$h_{\mu\nu} = A_{\mu\nu} e^{ik^\alpha x_\alpha} \tag{1.6}$$

where $A_{\mu\nu}$ is the polarization tensor and k^α is the wave vector. Using the *Transverse and Traceless gauge* gauge it is possible to express the polarization tensor as a linear combination of two independent components, corresponding to two possible polarization states of the GW:

$$A_{\mu\nu} = \begin{bmatrix} 0 & 0 & 0 & 0 \\ 0 & h_+ & h_\times & 0 \\ 0 & h_\times & -h_+ & 0 \\ 0 & 0 & 0 & 0 \end{bmatrix} = h_+ e^+_{\mu\nu} + h_\times e^\times_{\mu\nu} \tag{1.7}$$

defining:

$$e^+ = \begin{bmatrix} 0 & 0 & 0 & 0 \\ 0 & 1 & 0 & 0 \\ 0 & 0 & -1 & 0 \\ 0 & 0 & 0 & 0 \end{bmatrix}, \qquad e^\times = \begin{bmatrix} 0 & 0 & 0 & 0 \\ 0 & 0 & 1 & 0 \\ 0 & 1 & 0 & 0 \\ 0 & 0 & 0 & 0 \end{bmatrix} \tag{1.8}$$

e^+ and $e^\times$ represent the two orthogonal polarizations for waves propagating along the z-direction. For example, a monochromatic wave with a polarization h_+ travelling along the *z-axis* with an angular frequency ω produces a deformation pattern given by:

$$\begin{cases} x = x_0 \left(1 + \frac{h_+}{2} \cos(\omega t) \right) \\ y = y_0 \left(1 - \frac{h_+}{2} \cos(\omega t) \right) \end{cases} \tag{1.9}$$

The polarization h_+ momentarily stretches distances along the *x-axis* and simultaneously contract them along the *y-axis*. The polarization $h_\times$ produces a similar effect, but has its principal axes rotated by 45°. Therefore, a GW propagating in the z-direction produces a deformation on a ring of masses shown in Figure 1.1.

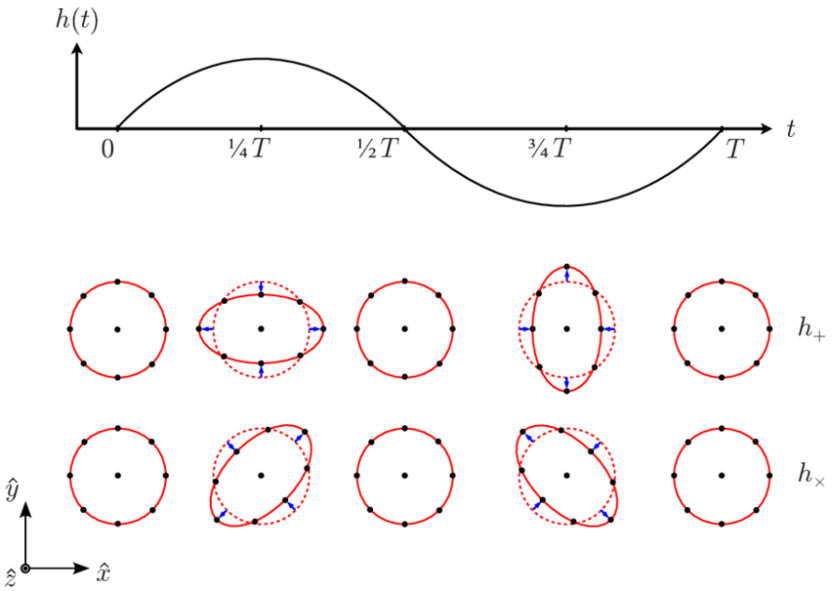

Figure 1.1: Effect of a gravitational wave (travelling in the z-direction) on a ring of test masses over a period T [9].

1.2 Sources of Gravitational-Waves

Similar to the emission of electromagnetic waves due to accelerated charged particles, the emission of gravitational waves is associated with accelerated masses. The mass and the linear angular momentum conservation imply that the first term to generate a GW is the quadrupole moment, given by [10]:

$$I_{\mu\nu} = \int dV (x_\mu x_\nu - \frac{1}{3}\delta_{\mu\nu} r^2)\rho(\boldsymbol{r}) \tag{1.10}$$

where $\rho(\boldsymbol{r})$ is the mass density. It is possible to express the amplitude of the small perturbation $h_{\mu\nu}$ in terms of the second-order temporal derivative of the quadrupole moment:

$$h_{\mu\nu} = \frac{2G}{Rc^4}\ddot{I}_{\mu\nu} \tag{1.11}$$

where G is the universal gravitational constant and R is the distance from the source to the observation point.

Applying equation 1.11 to man-size objects it is easy to see that it is quite impossible to have a laboratory source of gravitational waves and it is for this reason that the study of GW signals is focused on astronomical sources. A variety of objects and processes in the Universe could produce GW that are detectable on Earth as reported in Figure 1.2.

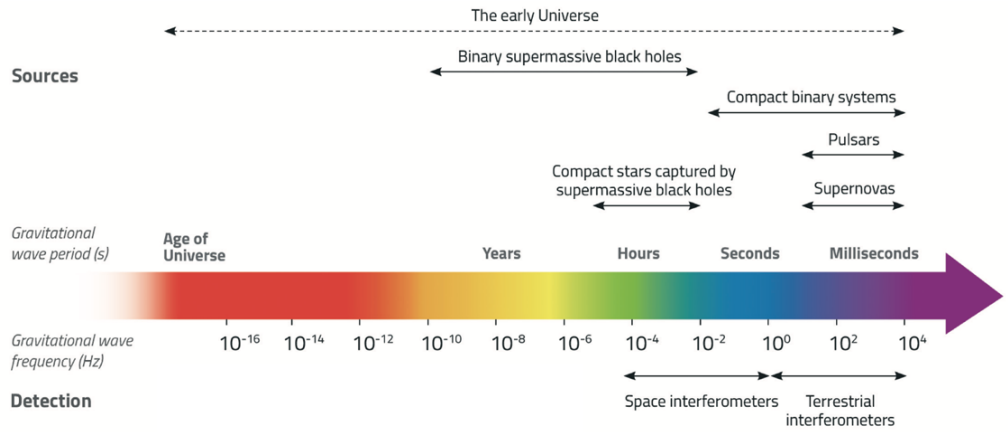

Figure 1.2: The GW spectrum. The x axis shows the frequency and the period on a logarithmic scale. Possible GW sources are reported above; interferometer detection bands are shown below. Adapted from: [11].

We can list sources that could produce GW in the sensitive frequency band of Gravitational-Wave Detectors (GWDs), between a few Hz and a few kHz, and classify them on the base of duration of their signal in that frequency band. Moreover, the signal amplitude must be compared with the interferometer noise level to understand if a successful detection can be made.

1. **Transient signals:** last for a short period (seconds or minutes) within the detector bandwidth.

    - **Coalescing binaries:** a compact binary system formed by a pair of black holes (BBH) or a pair of neutron stars (BNS) or a neutron star and a black hole (NS-BH) can lose energy by radiating GW and thus giving rise to a coalescence. The GW signal emitted by coalescing binaries is often called *chirp* waveform and is quasi-sinusoidal but sweeping in frequency and in amplitude as

shown in Figure 1.3. Mathematically the signal frequency $f(t)$ and amplitude $h(t)$ can be expressed by [10]:

$$f(t) \approx 2.1 \left(\frac{M_1 + M_2}{M_1^3 M_2^3} \right)^{1/8} \left(\frac{1\ day}{\tau} \right)^{3/8} \tag{1.12}$$

$$\begin{aligned} h(t) \approx 6.6 \cdot 10^{-24} \left(\frac{15\ Mpc}{R} \right) \left(\frac{M_1^3 M_2^3}{M_1 + M_2} \right)^{1/4} \cdot \\ \cdot \left(\frac{1\ day}{\tau} \right)^{1/4} (1 + 6cos^2\theta + cos^4\theta)^{1/2} \end{aligned} \tag{1.13}$$

where M_1 and M_2 are the masses of the two objects (BH or NS) in units of the solar mass, τ is the time until collision, R is the distance from the event to the observer and θ is the angle of inclination of the orbit of the system to the line of sight.

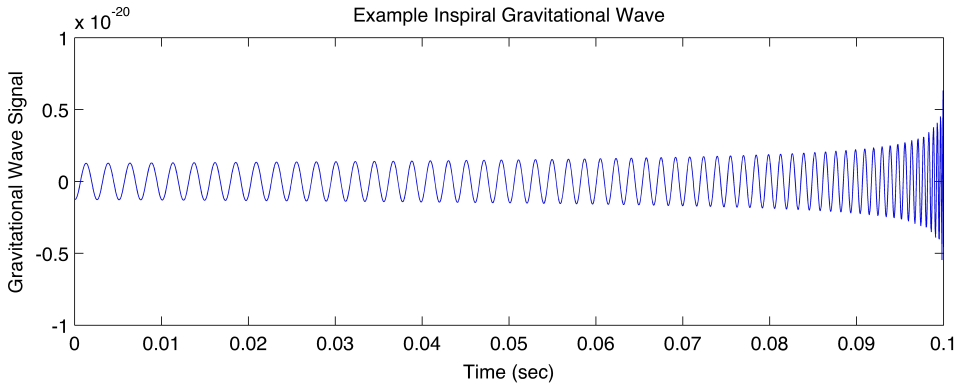

Figure 1.3: Example of a GW signal from coalescing binaries as a function of time [12].

- **Supernovae:** a GW burst can be emitted during a non-spherically symmetric gravitational collapse of typeII-supernovae followed by an asymmetric bounce. Typically the process is associated with an emission of light and the formation of a neutron star. The GW burst signal that is expected from this process is shown in Figure 1.4 and the amplitude h can be expressed as [13]:

$$h \approx 5 \cdot 10^{-22} \left(\frac{E}{10^{-3} M_{\odot} c^2} \right)^{1/2} \left(\frac{1\ ms}{\tau} \right)^{1/2} \cdot \cdot \left(\frac{1\ kHz}{f} \right) \left(\frac{15\ Mpc}{R} \right) \tag{1.14}$$

where $M_{\odot}$ is the mass expressed in solar mass units ($M_{\odot} \simeq 2 \cdot 10^{30}$ kg), R is the distance from the supernova, E is the total emitted energy, f and τ are the characteristic frequency and timescale respectively.

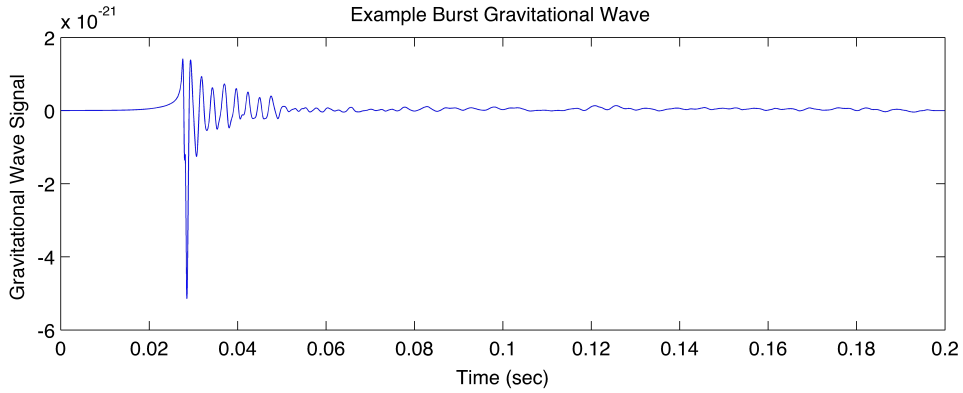

Figure 1.4: Example of a GW burst signal as a function of time [12].

2. **Long-lived signals:** last for a long period within the detector bandwidth.

   - **Pulsar:** GW can be emitted by non-axisymmetric neutron stars in rapid rotation. A NS has a radius of few tens of kilometres, a mass above 1.4 $M_{\odot}$ and a strong magnetic field. While rotating, a NS emits collimated radio waves from its magnetic poles and an external observer can detect a regular pulsating signal, hence the name. The expected continuous GW strain signal is reported in Figure 1.5 and its amplitude is given by [13]:

$$h \approx 4 \cdot 10^{-24} \left(\frac{1\ ms}{T} \right) \left(\frac{1\ kpc}{R} \right) \left(\frac{I}{10^{38} kg \cdot m^2} \right) \left(\frac{\epsilon}{10^{-6}} \right) \tag{1.15}$$

where ϵ is the equatorial ellipticity and T is the rotational period.

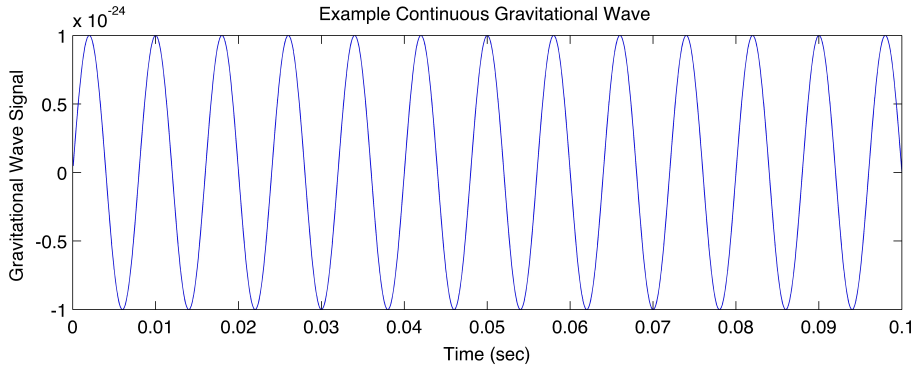

Figure 1.5: Example of a GW signal from a periodic source as a function of time [12].

- **Cosmological background from the big bang:** it is a non periodic signal with a roughly constant amplitude (also called stochastic background). It is predicted by currently accepted cosmological theories as a gravitational fossil background produced by strong space-time anisotropies in the early Universe (analogue of the microwave cosmic background radiation). The expected signal is reported in Figure 1.6 and its amplitude is given by [14]:

$$h \approx 10^{-20} \frac{h_g}{f} \tag{1.16}$$

where h_g is the amplitude of the initial inhomogeneity in the early Universe that is estimated to be around $\sim 10^{-5}$ [14].

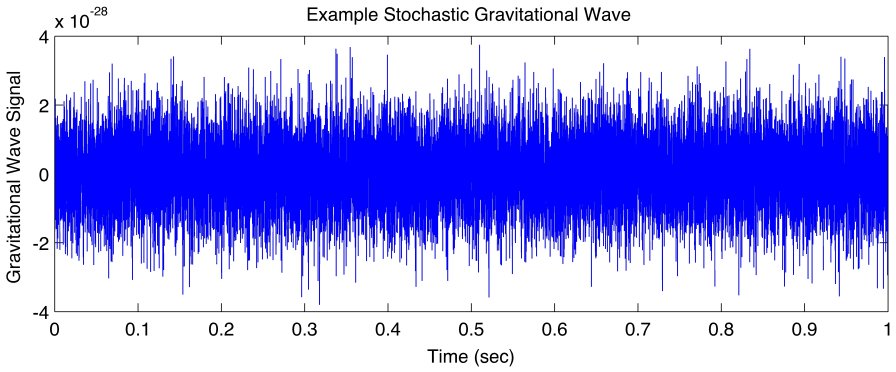

Figure 1.6: Example of GW signal from stochastic background as a function of time [12].

Ninety events detected during the third observing run are reported in Figure 1.7. All of them involve coalescing binaries: black holes are represented in blue, neutron stars in orange and compact objects of uncertain nature in grey. Each event involves three compact objects: the two coalescing bodies and the final merger remnant.

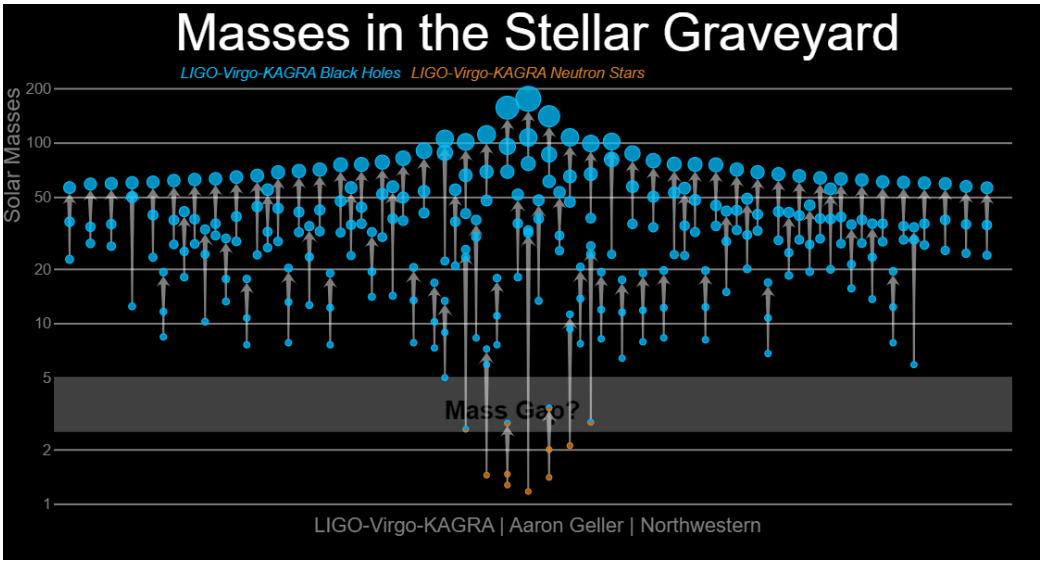

Figure 1.7: Ninety events observed during three observing runs, concerning black holes (blue), neutron stars (orange) and compact objects of uncertain nature (half blue and half orange) located in the grey region. Each event involves three compact objects. The mass of each object is reported on the y-axis in solar mass units [7].

Chapter 2

Interferometric Gravitational-Waves detectors

"Tre specchi prenderai; e i due rimovi
da te d'un modo, e l'altro, più rimosso,
tr'ambo li primi li occhi tuoi ritrovi.

Rivolto ad essi, fa che dopo il dosso
ti stea un lume che i tre specchi accenda,
e torni a te da tutti ripercosso."

Dante
Paradiso, Canto II, 1321

As explained in section 1.1, a GW can modify periodically the space-time in the plane perpendicularly to the direction of propagation. For example, a GW propagating on the z-direction with h_+ polarization, will cause alternating stretches and contractions in the x and y directions. Hence, one way to detect a GW is to measure the variation of distances using, for instance, the travel time of light in two orthogonal directions. An L-shaped Michelson interferometer (sketched in Figure 2.1) offers the possibility to compare the travel time of light propagating in its arms and therefore their length. The induced variation in length of the interferometer arms due to a GW propagating perpendicularly to the interferometer plane, results in a small change in the phase accumulated by the laser light travelling in the two arms and therefore in the intensity of the output light. In other words, an interferometric GWD acts as a transducer from travel time difference to output optical power and offers the opportunity of very high sensitivity over a wide range of frequencies.

2.1 Detection principle

To detect a GW it is necessary to measure the distance between two test masses. Figure 2.1 shows a simple Michelson interferometer. The laser source emits a beam of monochromatic light. A "50/50" beam splitter represents one free mass and divides the laser in two beams. There are two mirrors at the end of each arm, in the free-falling condition, that constitute two end test masses (ETM). Fabry-Perot cavities are implemented using two partially reflective mirrors, named input test mass (ITM).

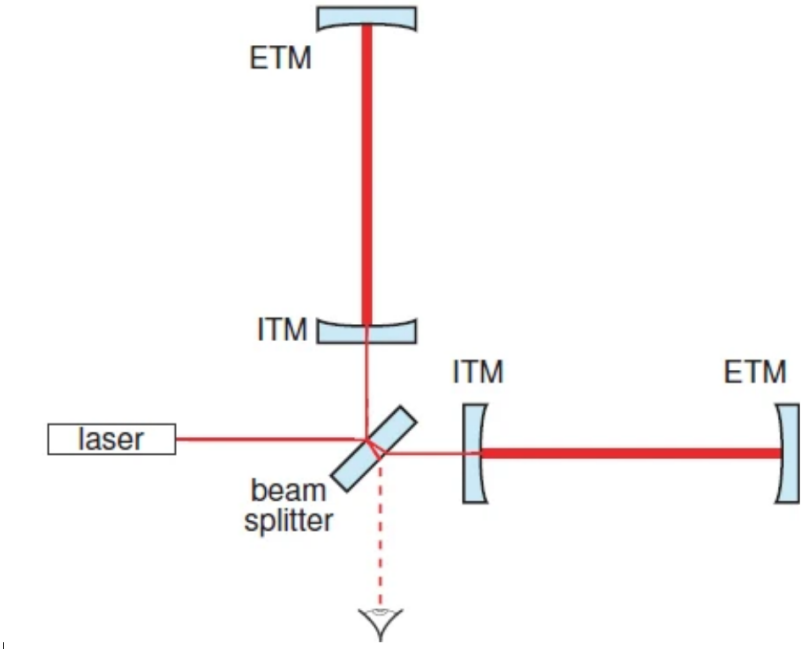

Figure 2.1: A sketch of a L-shaped Michelson interferometer with Fabry-Perot cavities. In GWDs the two arms are several kilometers long. Waves propagating perpendicular to the interferometer plane (e.g. entering the sheet) will result in one arm being increased in length while the other is decreased (and vice versa) [15].

We can consider the two arms aligned along the x and y axes, the beam splitter at the origin and a GW propagating along the *z-axis*. The space-time interval ds between two points connected by a light beam is equal to zero. So, recalling equation 1.1 and 1.4 and considering the light propagating in the x-arm we have:

$$\begin{aligned} ds^2 = 0 = g_{\mu\nu}dx^\mu dx^\nu = (\eta_{\mu\nu} + h_{\mu\nu})dx^\mu dx^\nu \\ = -c^2dt^2 + (1 + h_+(2\pi ft - \boldsymbol{k}\cdot\boldsymbol{x}))dx^2 \end{aligned} \tag{2.1}$$

as expected, the effect of the GW is to modify the distance dx between two neighbouring objects by an amount h_+. It is possible to evaluate the light travel time of the total round trip along the x-arm (from the beam splitter to the ETM and back):

$$\tau_{rtx} = \frac{2L}{c} + \frac{1}{2c}\int_0^L h_{11}(2\pi ft - \boldsymbol{k}\cdot\boldsymbol{x})dx - \frac{1}{2c}\int_L^0 h_{11}(2\pi ft - \boldsymbol{k}\cdot\boldsymbol{x})dx \tag{2.2}$$

a similar expression can be written for the y-arm using h_{22} instead of h_{11}. Moreover, if the GW has a + polarization, a frequency f_{gw} and amplitude $h_{11} = h_{22} = h(t) = he^{i2\pi f_{gw}L/c}$ then the total travel time difference between the two arms results to be:

$$\Delta\tau_{rt} = \tau_{rtx} - \tau_{rty} = h(t)\frac{2L}{c}sinc(2\pi f_{gw}L/c) \tag{2.3}$$

The phase shift results to be:

$$\Delta\phi = 2\pi f\Delta\tau_{rt} = h(t)\frac{4\pi L}{\lambda}sinc(2f_{gw}L/c) \tag{2.4}$$

where f and λ are the frequency and wavelength of the light inside the interferometer. The *sinc* function is defined as:

$$sinc(x) = \begin{cases} \frac{sin\pi x}{\pi x} & \text{if } x \neq 0 \\ 1 & \text{if } x = 0 \end{cases} \tag{2.5}$$

As expressed by Equation 2.4 the phase shift and hence the sensitivity are proportional to the length of the two arms L: this is why large scale interferometer were built. Moreover, introducing resonant optical Fabry-Perot cavities instead of classical arms it is possible to trap photons inside the cavity and cover the arm length multiple times before they recombine.

When the two beams recombine at the beam splitter, the resulting beam is reflected towards the photodetector and the phase shift between the two beams, due to the GW signal, will produce a modulation of the output power given by:

$$P_{out} = P_{in}sin(\phi_0 + \Delta\phi) \tag{2.6}$$

A control loop can lock the interferometer output on a dark fringe and the detection signal is obtained by the feedback signal given to the mirrors in order to maintain the interferometer locked on that dark fringe.

2.2 Operating ground-based detectors

At the moment there are five operating ground-based detectors as shown in Figure 2.2:

Figure 2.2: Operating ground-based detectors (blue dots): two aLIGO in the USA, AdV in Italy, GEO600 in Germany and KAGRA in Japan. LIGO India (yellow dot) is a replica of Advanced LIGO and will be built in the near future. Adapted from: [16].

- The LIGO project comprises two interferometers in U.S. (located in Hanford, Washington and Livingston, Louisiana) with arms of 4 km. LIGO project started in 1994 and some enhancements to improve the sensitivity of a factor of 10 were completed in 2015 with the advanced LIGO (aLIGO) project [17].
- Virgo interferometer in Italy (located in Cascina, near Pisa) has arms of 3 km. The Virgo project started as a scientific collaboration between

Italy and France and is now extended to several European countries. The upgrade to advanced Virgo (AdV) was completed in 2015 [18].

- KAGRA interferometer in Japan (located at Kamioka, in the Gifu prefecture) has arms of 3 km. KAGRA is situated underground and uses cryogenic mirrors [19].
- GEO600 in Germany (located in Hannover) has arms of 600 m (and is not considered a large-scale detector). GEO600 has features of observing detectors, but is also used as a prototype for new technologies under development [20].

Figure 2.3: Operating large scale detectors: LIGO Hanford (top left), KAGRA (top right), Virgo (bottom left) and LIGO Livingston (bottom right) [21].

A way to quantify the sensitivity of a GWD is to calculate its *horizon distance*: it is defined as the maximum range out to which it could see the coalescence of two 1.4 $M_{\odot}$ NS. Up to now, during the third observing run (O3), Virgo reached a sensitivity of 60.4 Mpc [22], LIGO Hanford and Livingstone 111 Mpc and 134 Mpc respectively [23] and KAGRA between 8 and 25 Mpc [24].

All the GWDs mentioned above form a network of operating detectors, located in different parts of the world, in order to observe GW signals and localize the position of their sources in the sky using the triangulation technique. In this way it is possible to observe also the electromagnetic counterpart of some GW events (in particular BNS coalescence and supernovae explosions). Up to now, only one event was observed by three interferometers at the same time and showed an electromagnetic counterpart: it is the GW170817 event produced by a BNS merging system, followed by gamma-ray burst, radio signals, X-rays and optical radiation. This event represents the birth of the multi-messenger astronomy [25].

2.3 Next generation of ground-based detectors

A new generation of more sensitive GWDs is planned for the near future:

- Einstein Telescope (ET) is the project to build in Europe a third generation detector. It should be arranged as an equilateral triangle with 10-km-long sides, built underground. This facility can host 3 detectors as outlined in Figure 2.4. Each detector will be made of 2 interferometers, one using a cryogenic system to cool some of the main optics to 10 – 20K. The start of observation is foreseen around 2035. Two candidate sites are under investigation: one in Sardinia and the other one in the Euregio Meuse-Rhine. The aim is to improve the detection frequency bandwidth and the sensitivity [26].

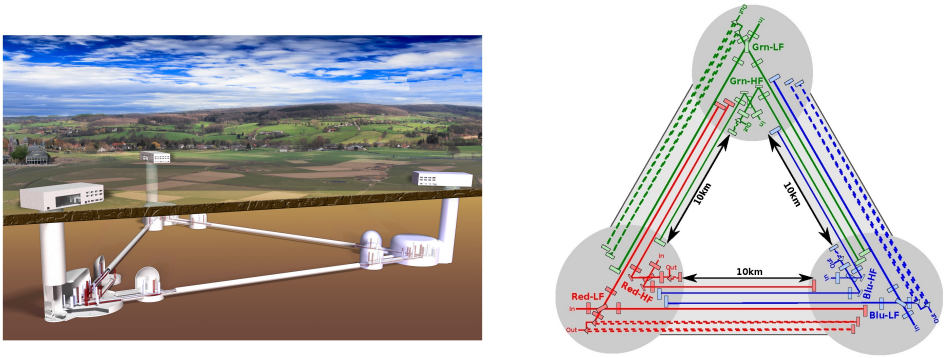

Figure 2.4: Left: artistic view of the ET observatory that would be built underground with a triangular shape. **Right:** draft scheme of the full ET observatory consisting of three interferometers represented with different colours [27].

- Cosmic Explorer will be built in U.S. and would consist of a L-shaped cryogenic ($\sim$ 120 K) detector with 40 km arms [28]. The expected improvement in sensitivity should allow us to reveal for the first time the complete population of stellar-mass black holes, starting from an era when the universe was still assembling its first stars [29].

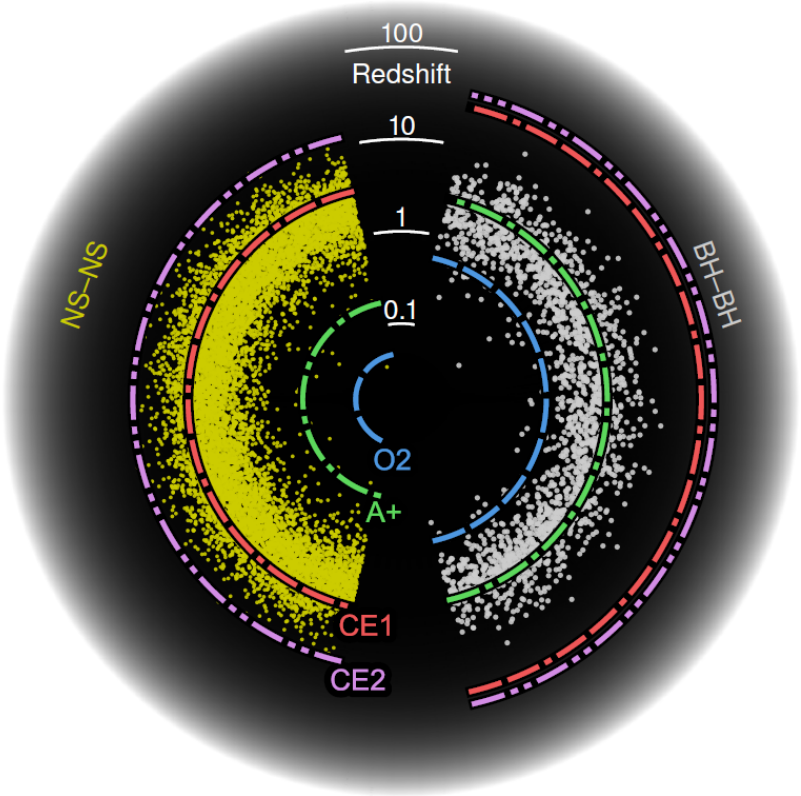

Figure 2.5: Comparison of astrophysical response distance between aLIGO during the second observing run (blue line), LIGO A+ (green line) and Cosmic Explorer in stage 1 and 2 (orange and purple lines). The population of $1.4 - 1.4M_{\odot}$ NS mergers and $30 - 30M_{\odot}$ BH mergers are reported in yellow and grey respectively [30].

2.4 Main noise sources

The only theoretical limitation to the measurement performed using an interferometer is the *Heisenberg Uncertainty Principle*. However, there are many practical issues to take into account that can generate noises and limit the sensitivity of an interferometer as described in Figure 2.6. A GW signal can be detected only if it has an amplitude higher than the total noise curve represented in black. This section briefly describes the main noise sources.

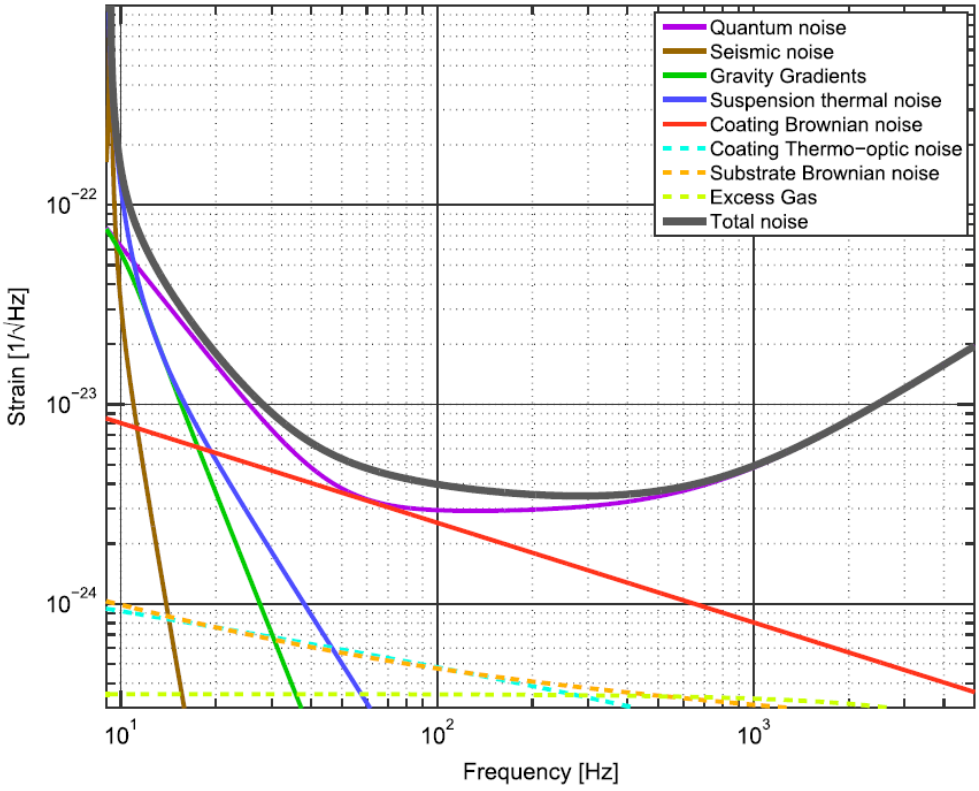

Figure 2.6: Sensitivity curve (black) obtained as the sum of different noise sources (coloured lines) listed at top-right [17]. At the moment, the most important limitations to sensitivity result from seismic and other ground-borne noises (at low frequencies), thermal noise due to test masses and their suspensions (in the mid range frequencies) and quantum noise, subdivided in shot noise (at high frequencies) and radiation pressure noise (at low frequencies). The coating thermo-optic noise also includes the contribution of the thermoelastic noise which will be discussed in more detail in the following.

2.4.1 Seismic noise

There are many sources that can produce ground movements, such as earthquakes, sea waves, wind, human activities, etc. The displacement spectral density due to seismic noise follows the empirical law:

$$S_x^{seismic}(f) \simeq \frac{A}{f^2} \tag{2.7}$$

where A is in the order of 10^{-6} mHz$^{1/2}$.

To reduce this kind of disturbance, each test mass is isolated with a pendulum system called super attenuator that can filter this displacement noise over 10 Hz [31]. Below 10 Hz seismic noise represents a detection limit to ground-based detectors.

2.4.2 Gravity gradient noise

A direct gravitational coupling of mass density fluctuations (e.g. seismic surface waves) with suspended mirrors can produce the so-called gravity gradient (or Newtonian) noise, that can limit the sensitivity at low frequencies. It is not possible to shield this kind of noise: one approach is to monitor the ground motion with some seismometers and produce a subtraction signal; another way is to choose a quiet location or going underground (as proposed for ET observatory 2.3).

2.4.3 Quantum noise

Quantum noise is produced by two effects that are related to the corpuscular nature of light:

- **Shot noise.** As explained in section 2.1, it is possible to measure the path length difference between the two arms of the interferometer by a measurement of the optical output power. It is equivalent to count the mean number of photons arriving at the detector (per unit time) and this quantity is characterized by a Poisson distribution. The statistical variability in the number of photoelectrons generated inside the photodetector produces the so-called shot noise. Its amplitude depends on arms length L, the laser wavelength λ and power P_{in} [10]:

$$h_{shot}(f) = \frac{1}{L}\sqrt{\frac{\hbar c\lambda}{2\pi P_{in}}} \tag{2.8}$$

Shot noise is frequency-independent (white) and can be reduced by increasing the laser power.

- **Radiation pressure noise.** Radiation pressure is a mechanical pressure due to exchange of momentum between photons and the mirror. This kind of noise arises from the same statistical uncertainty in the number of photons emitted by the laser outlined for the shot noise: the number of photons hitting the mirror can fluctuate and therefore the momentum transferred between photons and mirrors is not constant. The amplitude of the radiation pressure noise depends on the mirror mass m, on the arm length L, on the laser wavelength λ and power P_{in} [10]:

$$h_{rp}(f) = \frac{1}{mf^2L}\sqrt{\frac{\hbar P_{in}}{2\pi^3 c\lambda}} \tag{2.9}$$

  Radiation pressure noise is proportional to $1/f^2$, therefore dominates at low frequencies. One way to reduce the radiation pressure noise is to use heavier mirrors or decreasing the laser power.

Since the shot noise decreases when increasing the laser power, but the radiation pressure noise increases, quantum noise sets a fundamental limit to the sensitivity of GWDs. For a certain operational frequency, there will be an optimal laser power which minimizes the quantum noise: this limit is called *Standard Quantum Limit* and corresponds to the Heisenberg Uncertainty Principle [32].

2.4.4 Thermal noise

Thermal noise affects mirrors and the last stage of their suspensions, due to thermally induced dissipation mechanisms. Thermal noise in mirrors is subdivided in:

- **Brownian thermal noise.** It is associated to the random motion of the molecules inside every material: in GWDs it will produce fluctuations of mirror surfaces and hence a reduction in the sensitivity. Brownian thermal noise due to the substrate is an order of magnitude lower than that associated to the coating materials (orange dashed line and red solid line in Figure 2.6 respectively).

  The power spectral density of thermally induced surface fluctuations is determined by the rate of energy dissipation in each coating material,

as stated by the *fluctuation-dissipation theorem* [33]: the higher the energy loss, the higher the coating thermal noise (CTN). The CTN power spectral density S_{CTN} can be written in the form [34]:

$$S_{\mathrm{CTN}}(f) \propto \frac{k_B T}{2\pi f} \frac{d}{w^2} \phi_c(f, T) \tag{2.10}$$

where k_B is the Boltzmann constant, f is the frequency, T is the temperature, d is the coating thickness, w is the laser beam radius (where intensity drops by $1/\mathrm{e}^2$), and $\phi_c(f, T)$ is the loss angle associated with energy dissipation in the coating that will be better described in the next chapter, and corresponds to its internal mechanical friction for Brownian CTN.

- **Thermoelastic noise.** Any mechanical fluctuation, through thermal expansion, transforms elastic energy in heat, thus producing additional noise. The substrate thermoelastic noise for an entire coating stack is given by [35]:

$$S_{\mathrm{TE}}^{\mathrm{sub}}(f) = \frac{4 k_B T^2 \alpha_s^2 (1+\sigma_s)^2 k_s}{\pi^{5/2} (C_s \rho_s)^2 w^3 f^2} \tag{2.11}$$

where k_B is the Boltzmann constant, T is the temperature, α_s is the coefficient of thermal expansion of the substrate, σ_s is the Poisson ratio, k_s, C_s and ρ_s are the thermal conductivity, the heat capacity and the density of the substrate material respectively, w is the laser beam radius and f is the frequency.

- **Thermo-optic noise.** Thermal fluctuations in mirrors can produce a change in the coating thickness, but also a variation of its refractive index n, changing the overall optical path length of each coating material. The coating thermo-optic noise is given by [36]:

$$S_{\mathrm{TO}}^{\Delta z} \simeq S_{\mathrm{TO}}^{\Delta T} \left(\bar{\alpha}_c d - \bar{\beta} \lambda - \bar{\alpha}_s d \frac{C_c}{C_s} \right)^2 \tag{2.12}$$

where d is the coating thickness, C_c and C_s are the heat capacity per unit volume of the coating and substrate respectively, λ is the laser wavelength, $\bar{\alpha}_c$ and $\bar{\alpha}_s$ are the effective coefficient of thermal expansion of the coating and the substrate respectively, $\bar{\beta}$ is the effective thermorefractive coefficient that will be defined in section 3.2, $S_{\mathrm{TO}}^{\Delta T}$ is

the power spectrum of the coating thermal fluctuations responsible for thermo-optic noise and is given by [36]:

$$S_{\mathrm{TO}}^{\Delta T} = \frac{2}{\pi\sqrt{\pi}} \frac{k_B T^2}{w^2 \sqrt{k_s C_s f}} \tag{2.13}$$

where w is the laser beam radius, k_s is the substrate thermal conductivity and f is the frequency.

The design of test masses (substrates and coatings) and their suspensions is crucial for the most sensitive frequency bandwidth (around 100 Hz): low optical absorption, high reflectivity, low scattering and low internal friction are required at the same time. The state of art for GWDs mirrors and their suspensions is reported below:

- Suspensions: in advanced Virgo four monolithic fibres made of fused silica, with a diameter of 400 μm, are attached to each mirror (weighing 42 kg) using the silicate bonding technique [37, 18] as reported in Figure 2.7. LIGO adopts similar solutions.

- Substrate: at room temperature and using a 1064 nm laser wavelength, the best material found so far is high purity synthetic fused silica Suprasil© with ultra low optical absorption, very low internal friction and a flatness under 0.5 nm rms in the central area. The substrate has a diameter of $\sim$ 30 cm and a mass of $\sim$ 40 kg.

- Coating: in order to have a Bragg mirror, a stack of two alternating materials, with different refractive indices n, is required as shown in Figure 2.8. The reflectivity of a stack consisting of N doublets of materials with high and low refractive indices (n_H and n_L) deposited on a substrate with a refractive index n_{sub} is given by:

$$R \simeq 1 - 4 n_{sub} \left(\frac{n_L}{n_H} \right)^{2N} \tag{2.14}$$

From the previous equation, it is clear that it is possible to increase the reflectivity of the Bragg mirror using materials with a wide separation in their refractive indices.

The best materials found so far are silica (SiO_2) and titania-doped tantala ($Ti : Ta_2O_5$) presenting low ($n_L = 1.45$) and high ($n_H = 2.09$) refractive indices respectively (measured at 1064 nm). The loss angle of

$Ti : Ta_2O_5$ and SiO_2 coatings are $\phi \sim 3 \cdot 10^{-4}$ and $\phi \sim 4 \cdot 10^{-5}$ respectively [38]. These coating materials are produced at *Laboratoire des Matériaux Avancés* (LMA) using the ion-beam sputtering technique.

Thermal noise will be further explored in the next chapter.

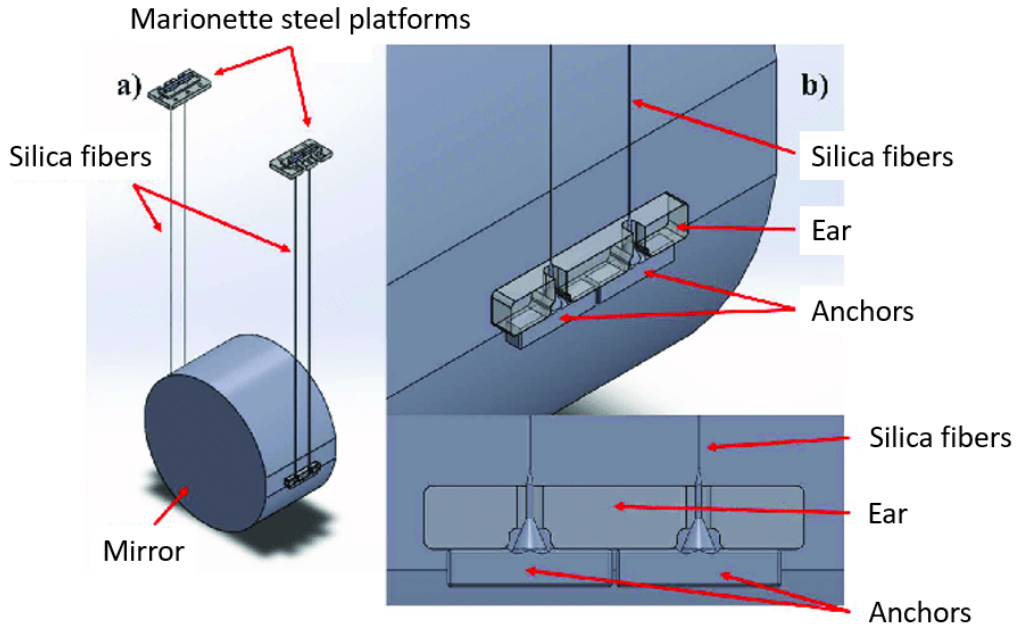

Figure 2.7: Sketch of the monolithic suspension. **On the left** a scheme of the monolithic suspension attached to the mirror. **On the right** details of anchors and ear [39].

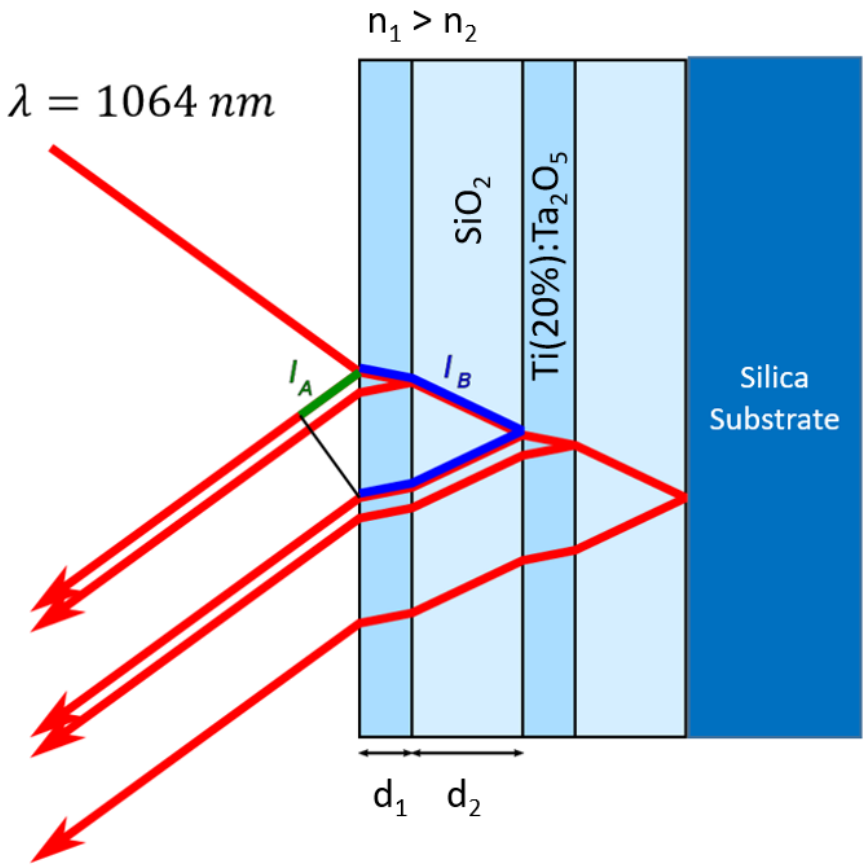

Figure 2.8: Sketch of a Bragg mirror formed by a stack of two alternating materials (with different refractive indices) deposited on a substrate. I_A and I_B represent two possible paths followed by the laser light: the geometry of the coating stack is such that the two beams are in phase. Currently, in LIGO and Virgo interferometers, the substrate is made of fused silica and the two coating materials are silica ($n = 1.45$) and titania-doped tantala ($n = 2.09$) [38].

Chapter 3

Thermal noise

"Les miroirs feraient bien de réfléchir un peu plus avant de renvoyer les images."

Jean Cocteau
Le sang d'un poète, 1932

In this chapter the theory of thermal noise is reviewed and treating separately in Brownian thermal noise, thermo-optic noise and thermoelastic noise. This thesis will deal with the first two types of noises.

3.1 Brownian thermal noise

Brownian thermal noise is due to small thermally driven random changes of the mirror's shape and produces a random displacement of the mirror's surface. The so called fluctuation-dissipation theorem, formulated by Callen and Welton [33, 40], is one of the most fundamental theorem in this research field and applies to any linear system at thermodynamic equilibrium. It establishes a proportionality relation between the microscopic thermal fluctuations of some degree of freedom $\hat{x}$ and the damping coefficient for the macroscopic motion when $\hat{x}$ is driven externally.

In the case of a mirror inside a GWD, where a laser measures the position of a test mass, $\hat{x}$ can be expressed as:

$$\hat{x} = \int f(\vec{r}) x(\vec{r}, t) d^2 r \tag{3.1}$$

where $\vec{r}$ is the location of a point on the mirror surface, t is the time, $x(\vec{r}, t)$ is the displacement along the direction of the laser beam (at a certain

point and time) and $f(\vec{r})$ is the form factor that depends on the laser beam profile. The integration is performed over the mirror surface.

It is possible to perform a mental experiment applying an oscillatory pressure to the surface of the test mass (with an amplitude F_0) and measure the average dissipated power (W_{diss}) in the test mass due to the action of this oscillatory pressure. The fluctuation-dissipation theorem establishes that the spectral density of fluctuations in $\hat{x}$ can be computed from:

$$S_{\hat{x}}(f) = \frac{2k_B T}{\pi^2 f^2} \frac{W_{diss}}{F_0^2} \tag{3.2}$$

where k_B is the Boltzmann constant, T is the temperature of the mirror and f is the frequency at which the spectral density is evaluated. In this way it is possible to reduce the problem of measuring thermal fluctuations to a problem in elasticity theory. In the case of a mirror inside a GWD, one common way to dissipate power is the internal friction in the test mass material [41]:

$$W_{diss} = 2\pi f U_{max} \phi(f) \tag{3.3}$$

where U_{max} is the elastic energy stored in the test mass when it is maximally contracted or extended under the action of the oscillating pressure, and $\phi(f)$ is the loss angle that characterizes the internal friction.

Internal friction occurs in every anelastic material and can arise from many internal properties such as the density of point defects, dislocations and grain boundaries. If the internal stress is varied, these properties typically require a finite interval of time to respond to the new state of stress, so when a stress is applied to an anelastic material, the strain response is not instantaneous, but shows a temporal shift called *relaxation time* [42]. Applying an oscillating stress σ with an amplitude σ_0 and a frequency f given by $\sigma = \sigma_0 e^{i2\pi ft}$, the resulting strain ϵ will be periodic with the same frequency (since the stress-strain relationship is linear), with an amplitude ϵ_0, but with a phase lag ϕ with respect to the stress: $\epsilon = \epsilon_0 e^{i(2\pi ft - \phi)}$. The phase lag between the stress and the resulting strain is known as the mechanical *loss angle*. For a mechanical system oscillating at a resonant frequency f_0, $tan(\phi)$ can be approximated to ϕ if $\phi << 1$ (as is the case in the following) and can be defined as:

$$\phi \equiv \frac{E_{\text{lost}}}{2\pi E} \equiv \frac{\Delta f}{f_0} \equiv \frac{1}{Q} \tag{3.4}$$

where E is the total energy stored in the oscillating system, E_{lost} is the energy dissipated in each cycle, Δf is the full width at half maximum (FWHM) of the resonance peak and Q is the *quality factor*.

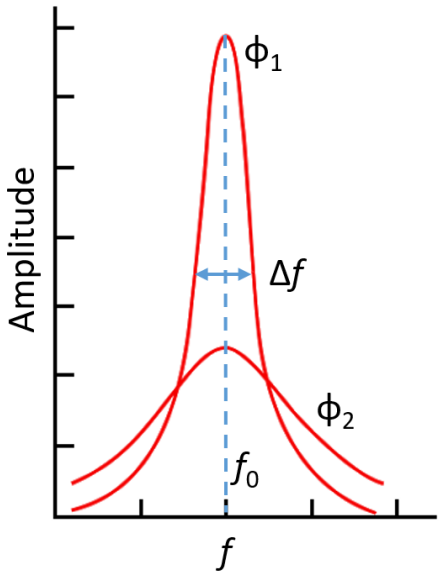

Figure 3.1: Example of two resonant peaks at the same frequency f_0, but with different Δf. Following definition (3.4) it is evident that $\phi_1 < \phi_2$ because the first peak is sharper than the second one (Δf is smaller).

If the frequency band being measured is much smaller than the mechanical resonant frequencies of the test mass (as is often the case in a GWD) the thermal noise is given by [34]:

$$S_{\hat{x}} = \frac{2k_B T}{\sqrt{\pi^3} f} \frac{1-\sigma^2}{Y w_m} \left[\phi_s(f) + \frac{1}{\sqrt{\pi}} \frac{d}{w_m} A \phi_c(f) \right] \tag{3.5}$$

where

$$A = \frac{Y'^2(1+\sigma)^2(1-2\sigma)^2 + Y^2(1+\sigma')^2(1-2\sigma')}{YY'(1-\sigma'^2)(1-\sigma^2)} \tag{3.6}$$

w_m is the laser beam width (defined as the radius at which the field amplitude of the Gaussian laser beam is reduced by a factor e) Y and Y' are the Young's moduli of the substrate and the coating, σ and σ' are their Poisson's ratios, d is the coating thickness, ϕ_s and ϕ_c are the loss angles of the substrate and coating respectively.

Looking at equations 3.5 and 3.6 it is possible to find some strategies for reducing the coating thermal noise. The most intuitive one is by cooling the mirror, but the temperature dependence of the loss angle must be taken into account. For example, fused silica shows a huge loss peak at cryogenic temperature and could not be used for this purpose.

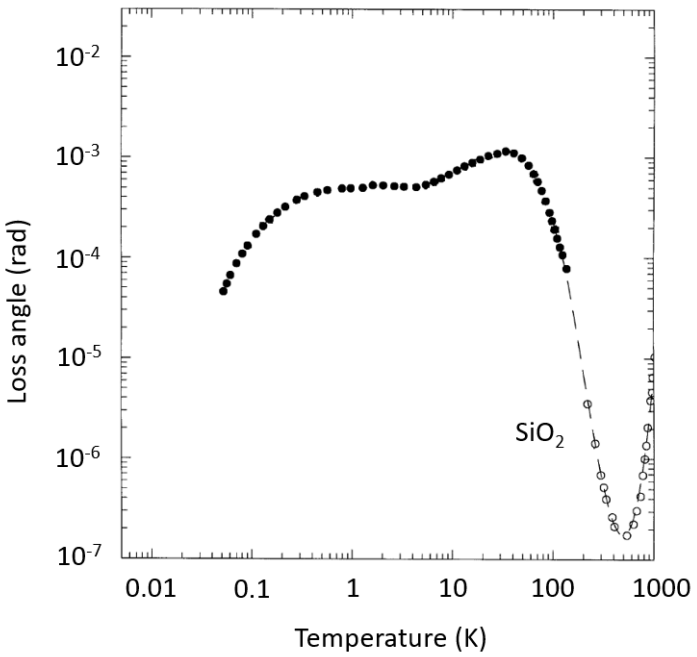

Figure 3.2: Temperature dependence of silica loss angle. Adapted from: [43].

Another approach is to enhance current coating materials (using for example doping, annealing treatments or new deposition techniques) or to identify alternative coating materials in order to lower the loss angle. Another possibility is the use of a laser beam with a larger radius w_m to sense the position of the mirror: the coating thermal noise depends on w_m^{-2}. Moreover, looking at equation 3.6, the coating thermal noise depends also on how well matched Young's moduli of the substrate and the coating are.

3.1.1 Measuring Brownian thermal noise

Brownian thermal noise is difficult to measure directly, but the fluctuation-dissipation theorem relates the magnitude and frequency spectrum of thermal fluctuations to the internal friction of the mirror material that is easier to measure using a *ring-down* technique [42]. In a ring-down experiment a resonant mode of the sample is excited and the exponential decay in amplitude $A(t)$ is recorded. Assuming that all the external sources of damping are minimized, the mechanical loss angle ϕ at the resonant frequency f_0 is related to the amplitude decay in time as:

$$A(t) = A_0 e^{-t/\tau} = A_0 e^{-\pi\phi(f_0) f_0 t} \tag{3.7}$$

where A_0 is the amplitude at $t = 0$ (when the external excitation is removed) and τ is the time constant (defined as the time at which the amplitude is reduced by a factor e).

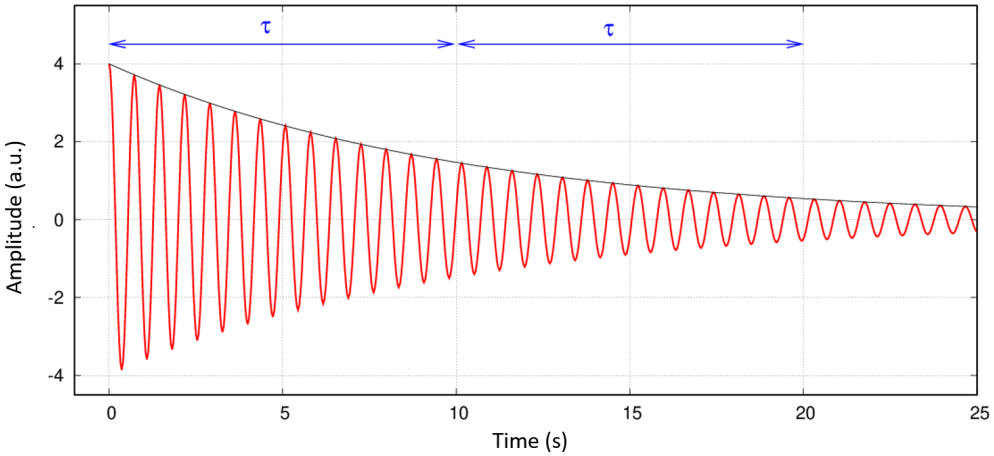

Figure 3.3: Example of a ring-down [44]. At the beginning the sample is forced to oscillate at a certain resonant frequency, then the external excitation is removed and the amplitude evolution in time is recorded. The black curve represent the exponential decay of the oscillation amplitude: after a time $t = \tau$ the amplitude is reduced by a factor e: $A(\tau) = A_0/e$.

Intrinsic losses of a coating material ϕ_c are measured comparing the sample losses before and after the coating deposition (assuming that losses of a silica substrate are stable in time and lower than that of the coating material). In Equation 3.4 E_{lost} can be divided in two components (the substrate s and the coating c). Moreover, it is possible to use Equation 3.4 to express $E_{\text{lost}} = 2\pi\phi E$. In this way, Equation 3.4 can be rewritten as:

$$\phi = \frac{E_{\text{lost c}} + E_{\text{lost s}}}{2\pi E} = \frac{2\pi\phi_c E_c + 2\pi\phi_s E_s}{2\pi E} \tag{3.8}$$

Moreover E_s can be replaced by $E - E_c$ and so:

$$\phi = \frac{2\pi\phi_c E_c + 2\pi\phi_s (E - E_c)}{2\pi E} = \phi_c D + \phi_s (1 - D) \tag{3.9}$$

where D is called *dilution factor* and is defined as the ratio between the energy stored in the coating and the total energy:

$$D = \frac{E_c}{E} \tag{3.10}$$

Therefore, from an experimental point of view, it is possible to derive a value of the coating loss angle associated with each resonant frequency:

$$\phi_c = \frac{\phi + (D-1)\phi_s}{D} \tag{3.11}$$

where $\phi = (\pi f \tau)^{-1}$ is the measured loss angle of the coated disk at a certain resonant frequency, $\phi_s = (\pi f_s \tau_s)^{-1}$ is the measured loss angle of the bare substrate at the same resonant frequency, D is the measured *frequency-dependent dilution factor* [45]:

$$D = 1 - \left(\frac{f_s}{f}\right)^2 \cdot \frac{m_s}{m} \tag{3.12}$$

where m_s and m are the sample masses as measured before and after the coating deposition respectively; f_s and f are the resonant frequencies as measured before and after the coating deposition respectively.

Underlying assumptions and a general proof of Equation 3.12 are provided by Gabriele Vajente in a technical note [46]. Equation 3.12 is valid provided that:

1. The mechanical loss in the system is low.
2. The substrate and coating can both be described in the thin plate approximation.
3. The substrate thickness and material properties are uniform.
4. The coating thickness and material properties are uniform.
5. The coating is thin enough so that the shape of each resonant mode of the substrate is not significantly changed after the film deposition.

It is possible to describe the motion of a resonator (a disk, for example) in terms of a set of eigenmodes $w_i(x, y, z)$, where w_i describes the displacement field for each point in the resonator. Each eigenmode can be considered as independent from all the others, assuming the assumption 1. In this way, the motion of the entire resonator can be described as the linear superposition of an infinite set of harmonic oscillators, each one with a frequency f_i and a deformation field $w_i(x, y, z)$. The potential energy of each oscillator is given by the elastic strain energy of the system when vibrates at that particular

mode and its averaged value over a cycle is equal to the average kinetic energy $\langle K_i \rangle$. It is possible to express the averaged elastic strain energy of the substrate $\langle E_{s_i} \rangle$ and the total averaged elastic strain energy $\langle E_i \rangle$ of the coated substrate in terms of their resonant frequencies f_i, densities ρ and eigenmodes w_i:

$$\langle E_{s_i} \rangle = \langle K_{s_i} \rangle = \frac{1}{2} f_{s_i}^2 \iiint_V \rho_s(x,y,z)(w_{s_i}(x,y,z))^2 dxdydz \tag{3.13}$$

$$\langle E_i \rangle = \langle K_i \rangle = \frac{1}{2} f_i^2 \iiint_V \rho(x,y,z)(w_i(x,y,z))^2 dxdydz \tag{3.14}$$

Therefore, using the dilution factor general definition 3.10 to each resonant mode:

$$D_i = \frac{\langle E_{c_i} \rangle}{\langle E_i \rangle} = 1 - \frac{\langle E_{s_i} \rangle}{\langle E_i \rangle} = \left(\frac{f_{s_i}}{f_i} \right)^2 \frac{\iiint_V \rho_s(x,y,z)(w_{s_i}(x,y,z))^2 dxdydz}{\iiint_V \rho(x,y,z)(w_i(x,y,z))^2 dxdydz} \tag{3.15}$$

Assuming the assumption 2, the deformation field depends only on the transverse coordinates and the deformation is in the direction perpendicular to the plane containing the resonator (z direction).

Moreover, assuming assumptions 3 and 4, the integration in the z direction can be factorized and Equation 3.15 simplifies to:

$$D_i = \left(\frac{f_{s_i}}{f_i} \right)^2 \frac{\rho_s h}{\rho_s h + \rho_c t} \frac{\iint_S (w_{s_i}(x,y))^2 dxdy}{\iint_S (w_i(x,y))^2 dxdy} \tag{3.16}$$

where h and t are the substrate and coating thicknesses respectively; ρ_s and ρ_c are the surface densities of the substrate and coating respectively. Finally, assuming the assumption 5, it is possible to say that $w_{s_i}(x,y) \simeq w_i(x,y)$ and so Equation 3.16 simplifies to:

$$D_i = \left(\frac{f_{s_i}}{f_i} \right)^2 \cdot \frac{m_s}{m} \tag{3.17}$$

It is possible to conclude that Equation 3.17 allows us to measure experimentally the frequency-dependent dilution factor and is derived from the general definition 3.10, under the five assumptions listed above that are typically met by the used samples.

3.2 Coating thermo-optic noise

Coating thermo-optic noise manifests itself as a change in the reflection phase from the mirror, resulting from temperature fluctuations in the coating material. The reflection phase from the coating can change due to two effects that are produced by the same temperature fluctuations:

- **The thermoelastic effect**. The thickness of a coating can change due to thermal expansion driven by temperature fluctuations in the material. Changes in thickness produce a displacement of the reflection phase of the coating with respect to a reference plane: it is indicated in Figure 3.4 as $\varphi_{c\ TE}$. If the temperature increases, then the coating surface moves towards the laser beam. The resulting variation in the reflection phase φ_{cTE} as a function of temperature is given by [49]:

$$\frac{\partial \varphi_{\mathrm{c\ TE}}}{\partial T} = 4\pi \bar{\alpha}_c \frac{d}{\lambda} \tag{3.18}$$

  where d is the coating thickness, λ is the wavelength and $\bar{\alpha}_c$ is the effective thermal expansion coefficient. Assuming that the coating elastic coefficients are similar to those of the substrate material, the effective thermal expansion coefficient simplifies to [49]:

$$\bar{\alpha}_c \sim 2\alpha_c(1+\sigma_c) \tag{3.19}$$

  where α_c and σ_c are the coating thermal expansion coefficient and Poisson ratio respectively.

- **The thermorefractive effect**. Thermal fluctuations in mirrors can produce a change in the coating thickness, but also a variation of its refractive index. Thermorefractive effect takes into account both those effects inside the coating, producing a variation in the optical path length of each coating layer [36]: it is indicated in Figure 3.4 as $\varphi_{c\ TR}$. If the temperature increases, then the coating optical length increases and the laser light will travel for a longer path inside the coating. The resulting variation in the reflection phase $\varphi_{\mathrm{c\ TR}}$ as a function of temperature for a Bragg mirror due to thermorefractive effect is given by:

$$\frac{\partial \varphi_{\mathrm{c\ TR}}}{\partial T} = \pi \frac{(\beta_H + n_H \alpha_H) + (\beta_L + n_L \alpha_L)(2(n_H/n_L)^2 - 1)}{4(n_H^2 - n_L^2)} \tag{3.20}$$

where n is the refractive index, α is the thermal expansion coefficient and β is the thermo-optic coefficient defined as:

$$\beta(T) = \frac{dn(T)}{dT} \tag{3.21}$$

Subscripts H and L stand for high and low refractive indices respectively.

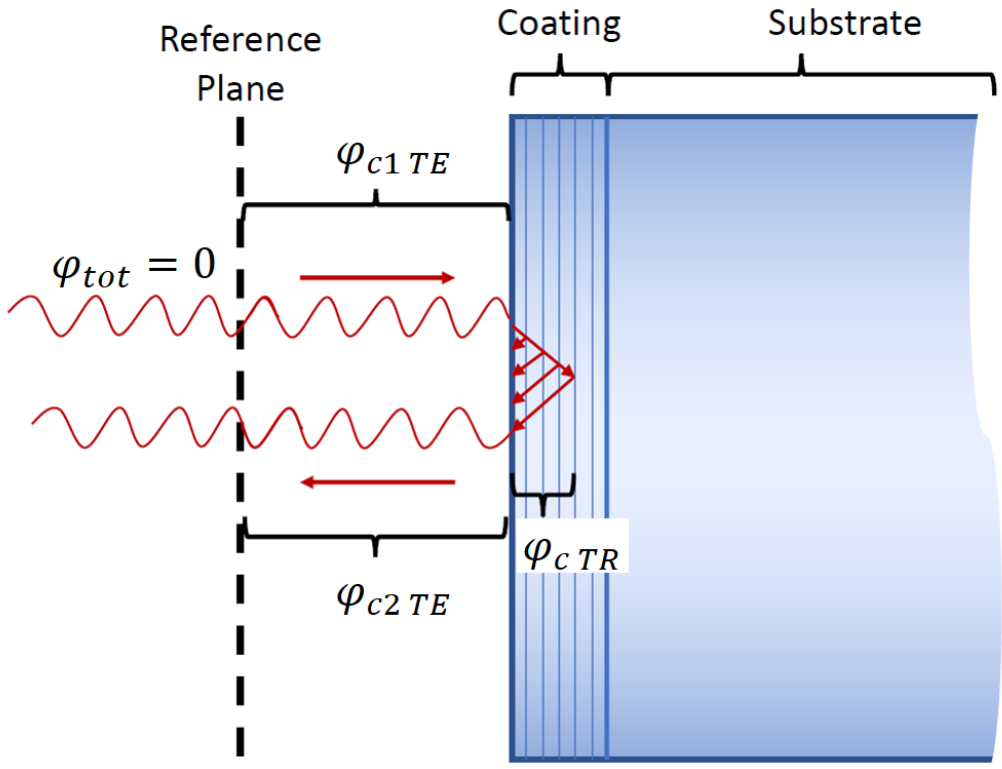

Figure 3.4: Representation of a laser beam reflected by a Bragg mirror. The coating surface can move with respect to a reference plane due to the thermoelastic effect, producing a variation in the phase indicated as $\varphi_{c\ TE}$. Moreover, the thermorefractive effect can cause a variation of the thickness and refractive index of each coating layer, producing a variation in phase indicated as $\varphi_{c\ TR}$. Adapted from: [50].

The thermo-optic noise is the coherent sum of thermoelastic and thermorefractive effects. The total phase accumulation for a round trip between the reference plane and the coating is $\varphi_{tot} = \varphi_{c1\ TE} + \varphi_{c2\ TE} + \varphi_{c\ TR}$ as represented in Figure 3.4. The thermoelastic noise can produce a variation of

phase $\varphi_{c1\ TE} + \varphi_{c2\ TE}$ outside the coating and the thermorefractive noise can produce a variation of phase $\varphi_{c\ TR}$ inside the coating. Thermoelastic and thermorefractive effects can partially cancel each other out: in this way, the thermo-optic noise for an entire mirror may be smaller than both contributing noises and it is given by [36]:

$$\begin{aligned} S_{\mathrm{TO}}^{\Delta z} &\simeq S_{\mathrm{TO}}^{\Delta T} \left[\frac{\lambda}{4\pi} \left(\frac{\partial \varphi_{\mathrm{c\ TE}}}{\partial T} + \frac{\partial \varphi_{\mathrm{c\ TR}}}{\partial T} \right) - \bar{\alpha}_s d \frac{C_c}{C_s} \right]^2 \\ &\simeq S_{\mathrm{TO}}^{\Delta T} \left(\bar{\alpha}_c d - \bar{\beta} \lambda - \bar{\alpha}_s d \frac{C_c}{C_s} \right)^2 \end{aligned} \tag{3.22}$$

where d is the coating thickness, C_c and C_s are the heat capacity per volume of the coating and substrate respectively, $S_{\mathrm{TO}}^{\Delta T}$ is the power spectrum of the coating thermal fluctuations responsible for thermo-optic noise, given by [36]:

$$S_{\mathrm{TO}}^{\Delta T} = \frac{2}{\pi\sqrt{\pi}} \frac{k_B T^2}{w^2 \sqrt{kCf}} \tag{3.23}$$

$\bar{\alpha}_c$ is the effective coefficient of thermal expansion of the coating given by 3.19 (the same expression is valid for the effective coefficient of thermal expansion of the substrate $\bar{\alpha}_s$), $\bar{\beta}$ is the effective thermorefractive coefficient defined as [36]:

$$\bar{\beta} \simeq \frac{(\beta_H + n_H \alpha_H) + (\beta_L + n_L \alpha_L)(2(n_H/n_L)^2 - 1)}{4(n_H^2 - n_L^2)} \tag{3.24}$$

where n_H and n_L are the high and low refractive indices of the coating materials, β_H and β_L, α_H and α_L are the thermo-optic coefficients and the coefficients of thermal expansion of high and low refractive indices materials in the coating stack. It is clear that for a proper evaluation of the thermo-optic noise it is important to measure α, β and n of each coating material, which may be different from those of the corresponding bulk materials.

The coating thermo-optic noise of the current coating materials is about ten times smaller than the Brownian thermal noise (as reported in Figure 2.6). In any case, it is important to take the thermo-optic noise into account for the next generation of coating materials and to compare its amplitude with that of the Brownian noise.

3.2.1 Measuring $\alpha + \beta/n$ of a coating

In our laboratory we use an experimental technique similar to the one developed by Gretarsson [50] at the Embry-Riddle Aeronautical University to exploit the thin film interference phenomenon in order to estimate the optical thickness of a coating defined as:

$$L = n \cdot D \tag{3.25}$$

where n is the refractive index of the coating material and D is its nominal thickness. The optical thickness of the coating can change because both n and D can vary due to thermal fluctuations, so the dependence of L with temperature can be expressed as:

$$\frac{dL}{dT} = \frac{dn}{dT}D + \frac{dD}{dT}n \tag{3.26}$$

Dividing both sides by L we have:

$$\frac{1}{L}\frac{dL}{dT} = \frac{dn}{dT}\frac{D}{L} + \frac{dD}{dT}\frac{n}{L} = \frac{1}{n}\frac{dn}{dT} + \frac{1}{D}\frac{dD}{dT} \tag{3.27}$$

and we can express the relative variation of the optical length with temperature as:

$$\frac{1}{L}\frac{dL}{dT} = \alpha + \frac{\beta}{n} \tag{3.28}$$

where $\alpha = \frac{1}{D}\frac{dD}{dT}$ is the thermal expansion coefficient and $\beta = dn/dT$ is the thermo-optic coefficient.

It is possible to measure L by using the thin film interference phenomenon in which broadband light waves are reflected or transmitted by the upper and lower boundaries of the coating and interfere with one another, either enhancing or reducing the reflected light, producing a pattern of maxima and minima. This kind of experiment can be performed in two configurations: in reflection using a silicon substrate or in transmission using a silica substrate. In Fig 3.5 a simple scheme of the interference produced by two reflected beams is reported.

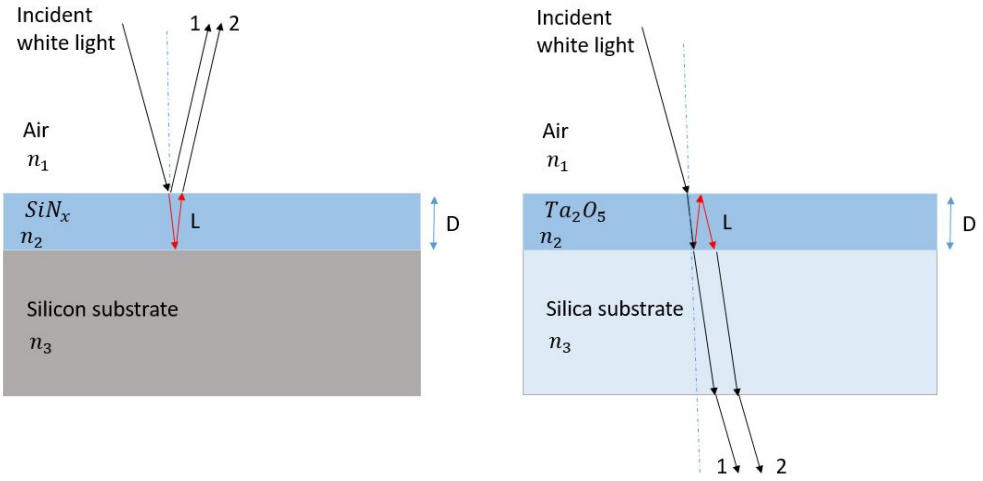

(a) **(b)**

Figure 3.5: Thin film interference phenomenon in reflection (a) and in transmission (b).

Let's focus on the measurement of reflected light using a silicon substrate (Fig 3.5 a). In this case we have an interference phenomenon because the incident white light can follow two different paths:

1. The incident white light from the air can be reflected off the coating surface
2. The incident white light is transmitted in the coating, reflected off the substrate surface, travelling back through the coating and out into the air again.

There is a difference in the path followed by the two beams: the second one travels twice across the coating and so it is shifted by $2L$ from the first one. In this way, if we use a broadband incident light, we can observe an interference pattern. The conditions to have maxima and minima are the following:

- If $2L$ is equal to an even multiple of $\lambda/2$ the two beams will be in phase and constructive interference is observed.
- If $2L$ is equal to an odd multiple of $\lambda/2$ the two beams will be out of phase and destructive interference is obtained.

The same behaviour is also observed for transmitted light measurements using a silica substrate (3.5 b).

So, in general, using broadband white light on a thin film with an optical length L we will observe extrema located at:

$$\lambda_j = \frac{4L}{N} \rightarrow \begin{cases} maximum & \text{for even N} \\ minimum & \text{for odd N} \end{cases} \tag{3.29}$$

Moreover, reflected waves undergo a 180° phase shift when $n_2 > n_1$. Usually, using a silicon substrate, both reflected beams will have a 180° phase shift because $n_2 > n_1$ and also $n_3 > n_2$ producing a total 360° shift. So, for this particular configuration of materials with ($n_1 < n_2 < n_3$), the total phase shift is not considered.

An example of a measured interference pattern observed using a ~ 4300 nm SiN_x coating deposited on a silicon substrate at room temperature is shown in Figure 3.6 (a). From the location of these extrema it is possible to estimate the coating optical thickness. First of all, the raw reflected spectrum is normalized with the lamp spectrum represented in Figure 3.6 (b). The result is shown in Figure 3.6 (c) and maxima and minima positions are identified performing a parabolic fit.

The peak wavelengths in equation (3.29) can be identified by an index j as following: if N_1 is the number of quarter-wavelength contained in the coating at the longest wavelength, equation (3.29) can be rewritten as:

$$\lambda_j = \frac{4L}{N_1 + j - 1} \tag{3.30}$$

In this way j=1 identifies the extrema with the higher wavelength and increasing j all the extrema at lower wavelengths are identified as well (from right to left in Figure 3.6 (c).

The coating optical length at a certain temperature is obtained by fitting equation (3.30) using extrema wavelengths λ_j identified in Figure 3.6 (c). The goal of this experiment is to measure the coating optical length (from the locations of the spectrum extrema) for different temperatures. According to equation (3.28), the relative variation of the optical length with temperature is equal to the combination of thermo-optic parameters $\alpha + \beta/n$.

Moreover, from the value of the coating nominal thickness D provided by the developer and from the value of the coating optical thickness L measured at room temperature it is possible to evaluate the coating refractive index n.

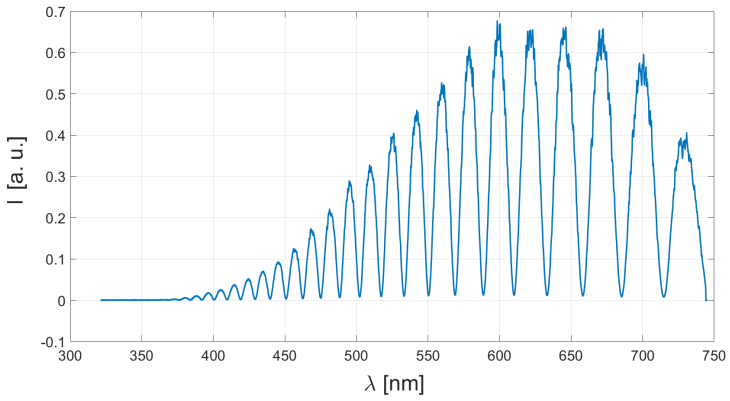

(a) *raw reflected spectrum*

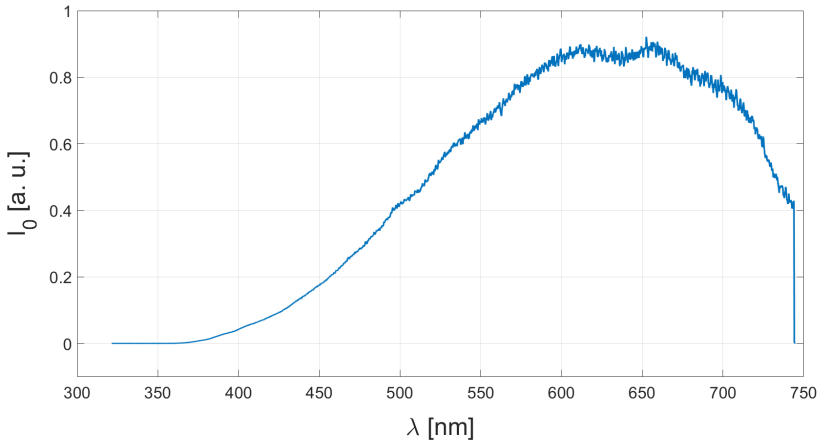

(b) *raw lamp spectrum*

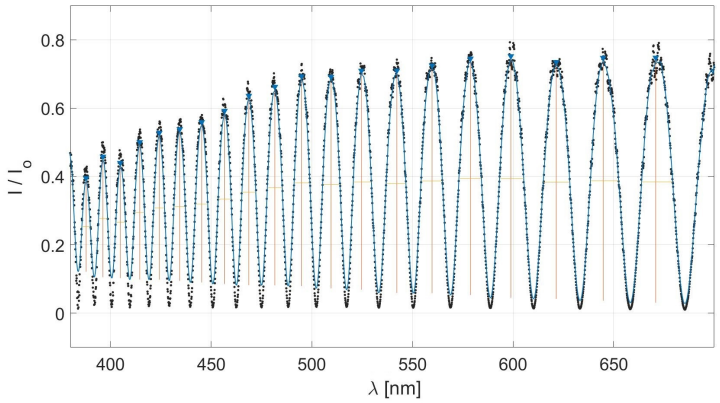

(c) *Normalized reflected spectrum*

Figure 3.6: Top: raw reflected spectrum from a $\sim$ 4300 nm silicon nitride coating deposited on a silicon disk at room temperature. **Middle:** raw lamp spectrum. **Bottom:** normalized reflected spectrum.

3.2.2 Measuring α of a coating

It is possible to determine the thermal expansion coefficient α_c of a coating material depositing it upon a cantilever substrate with a different thermal expansion coefficient α_s. Increasing the temperature, the dimensions of the two materials increase by different amounts, resulting in bending as represented in Figure 3.7. The Stoney's equation relates the coating stress to the radius of curvature at a certain temperature [51, 52]:

$$\sigma_c = \frac{1}{6} B_s \frac{t_s^2}{t_c} \left(\frac{1}{R_0} - \frac{1}{R} \right) \tag{3.31}$$

where B_s is the biaxial modulus of the substrate, defined as $B = Y/(1-\sigma)$, t_s and t_c are the thicknesses of the substrate and coating respectively, R_0 and R are the radii of curvature of the uncoated and coated substrate respectively.

Some of this stress is related to the thermal expansion mismatch between coating and substrate materials [52]:

$$\sigma_c = \sigma_I + (\alpha_c - \alpha_s) B_c \Delta T \tag{3.32}$$

where σ_I is the coating intrinsic stress from non-thermal sources, B_c is the biaxial modulus of the coating and ΔT is the temperature variation. Therefore, the variation of coating stress with temperature is given by:

$$\frac{d\sigma_c}{dT} = (\alpha_s - \alpha_c) B_c \tag{3.33}$$

In this way, knowing B_s, t_s, t_c and measuring the variation of curvature with temperature, it is possible to determine the linear dependence of the coating stress with temperature and hence to calculate α_c from the slope of the linear fit, knowing B_c and α_s.

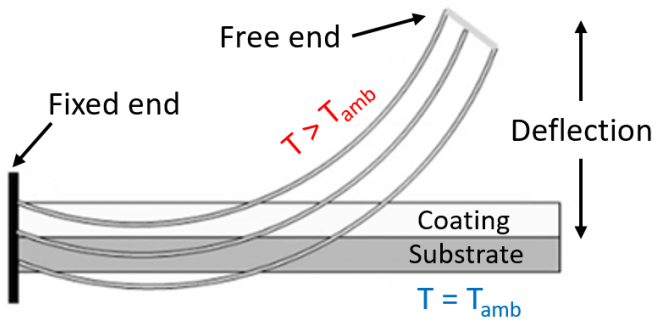

Figure 3.7: Bending of a bi-material cantilever fixed at one end due to the α mismatch between the two materials. Adapted from: [53].

3.3 Thermoelastic noise

Thermoelastic noise is created by the stochastic flow of heat within each mirror, which produces stochastically fluctuating hot and cold spots inside test masses. The test-mass material expands in the hot spots and contracts in the cold spots, creating fluctuating bumps and valleys on the mirror faces that can affect the measurement of the position of test masses in an interferometer [47]. Moreover, an irreversible heat flux between those two region can be generated, giving rise to dissipation. The main feature of the thermoelastic noise is represented by the characteristic time of heat migration τ_{th} that depends on material properties and on the vibrational mode geometry:

$$\tau_{th} = Cd^2 \frac{c_V}{k} \tag{3.34}$$

where C is the adimensional form factor (that depends on the shape of the vibrational mode), d is the distance between expansion and contraction regions, c_V is the specific heat per unit volume and k is the thermal conductivity. The associated thermoelastic loss angle is given by:

$$\phi_{th}(f) = \phi_0 \frac{f \cdot f_{th}}{f^2 + f_{th}^2} \tag{3.35}$$

where f is the vibrational frequency and f_{th} is the reciprocal of τ_{th}. If f is small with respect to f_{th}, the thermalization between expanded hot spots and contracted cold spots occurs almost instantaneously; if f is higher with respect of f_{th}, there is not enough time to establish an heat flux. The maximum dissipation happens when $f = f_{th} = 1/\tau_{th}$ originating the so-called *Debye peak* represented in Figure 3.8. Thermoelastic noise is particularly important for crystalline materials like silicon or sapphire which have a large thermal conductivity and a high coefficient of thermal expansion.

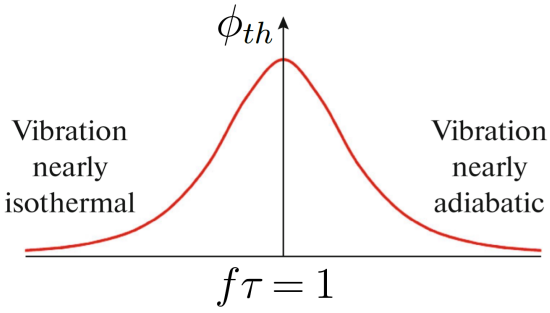

Figure 3.8: Example of a Debye peak. Maximum dissipation is located at $f\tau = 1$. Adapted from: [48].

Chapter 4

Experimental facilities

"Misura ciò che è misurabile,
e rendi misurabile ciò che non lo è."

Galileo Galilei

4.1 Coating loss angle evaluation using GeNS

As explained in chapter 3, a lot of efforts are dedicated in identifying coating materials with low mechanical dissipation and hence low Brownian thermal noise. Loss angle measurements can be performed using the ring-down technique explained in section 3.1.1. The sample must be held during the measurement by some kind of suspension or clamping, but it is necessary that the energy transferred from the sample to the suspension is negligible. The Gentle nodal suspension system (also called GeNS) [54] allows to measure the loss angle of a disk-shaped material in a ring-down experiment, minimizing all external damping sources. In this system the sample is suspended on the top of a sapphire sphere (or hemisphere) touching on one of its nodal point of vibration as shown in Figure 4.1. Another advantage is that any damage to the thin film surface can be avoided.

The contact area between the sphere and the sample can be evaluated by:

$$r_c = \left[\frac{3}{4} MgR \left(\frac{1-\sigma^2_{sample}}{Y_{sample}} + \frac{1-\sigma^2_{sphere}}{Y_{sphere}}\right)\right]^{1/3} \tag{4.1}$$

where r_c is the contact surface radius, M is the mass of the sample, R is the radius of the sphere, Y_{sample}, Y_{sphere}, σ_{sample} and σ_{sphere} are the Young's moduli and the Poisson's ratios of the sample and the sphere respectively.

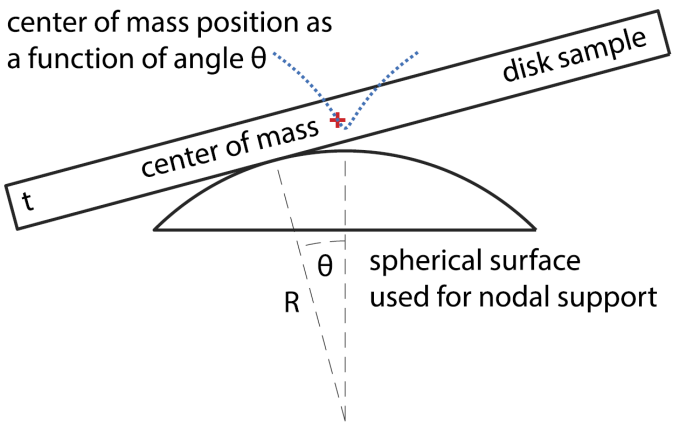

Figure 4.1: GeNS scheme: a disk with a thickness t is suspended on the top of a spherical surface. The red cross and blue dots show the centre of mass position for a given inclination angle θ (not to scale) and its shift as a function of the inclination angle [55].

A stable equilibrium is achieved whenever $R > t/2$, where R is the radius of curvature of the spherical suspension and t is the thickness of the disk. If the static friction between the sample and the suspension is large enough, the angular range where stable oscillations are possible is [54]:

$$\theta \sim \pm\sqrt{3\frac{2R-t}{t}} \tag{4.2}$$

that is a large stability interval compared with the induced small oscillations of the sample. Disks modes are excited using an electrostatic actuator held at about 1 mm from the disk surface and driven with high AC voltage. Typically, a laser with an optical lever of some meters is used to sense the amplitude of disk vibrations. Since the sample is suspended in its centre, only resonant modes that do not have a significant deformation in the centre are measurable. Some of them are represented in Figure 4.2.

There are different resonant mode *families*: *butterfly modes* have zero radial nodal lines and are also reported with the notation (0,n) or *family 0*; *mixed modes* have one or more radial nodal lines and are reported with the label (1,n) or *family 1*, (2,n) or *family 2*, etc... Butterfly modes and mixed modes are measurable with a GeNS facility, because the centre is a nodal point. There are also resonant modes in which the centre is not a nodal point and can not be measured using this system.

This kind of facility, initially developed by the INFN Urbino-Firenze Group, is currently the preferred solution of the Virgo and LIGO Collab-

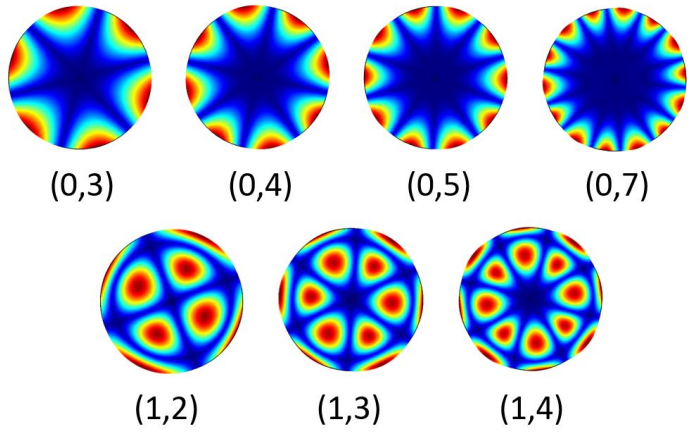

Figure 4.2: Resonant modes identified with the (r,a) notation. In the first line some *butterfly modes* are represented; in the second line some *mixed modes* are reported. The colour scale represent the oscillations amplitude from blue (no movement) to red (wider movement).

orations for performing internal friction measurements because it avoids systematic extra-damping and consequently an overestimation of the loss angle [38, 55].

4.1.1 Room temperature GeNS

A new facility for ring-down measurements was designed and created specifically for the Urbino laboratory. A 3D representation of the vacuum chamber, a scheme of the connections and the laser beam path are reported in Figure 4.6. Two GeNS are installed on the experimental plate: on the first one a sample is suspended in equilibrium near an electrostatic actuator (~ 1 mm below its surface) for dissipation measurements; on the other one an identical sample is suspended with a thermometer fixed on its surface. In this way it is possible to measure at the same time the temperature and the loss angle of a suspended sample, under the assumption that the two samples are at the same temperature.

Vacuum system

A scroll pump (Agilent Varian *TriScroll PTS03001*) is linked to the turbo-molecular pump and directly to the chamber for the primary vacuum. A turbo-molecular pump (Agilent Varian *Turbo-V 550*) is connected to the bottom of the chamber via a mechanical attenuator in order to avoid sample

movements due to vibrations induced by the pump. Moreover, and an ion-pump (Agilent Varian *Vaclon Plus 55 StarCell*) is linked to a flange on one side of the chamber. In this way it is possible to create a primary vacuum with the scroll pump, turn on the turbo-molecular pump (around 10^{-1} mbar) and reach a high vacuum. At the end, when the pressure is below 10^{-5} mbar, it is possible to turn on the ion-pump and turn off all the other pumps, eliminating all undesired noises and vibrations. The vacuum level is measurde by a Pirani/cold cathode gauge (Thyracont *Smartline VSM-79DL*) covering a range from 1200 to $5 \cdot 10^{-10}$ mbar. A small venting valve is linked to a flange on one side of the chamber. A scheme of the vacuum system is reported in Figure 4.3.

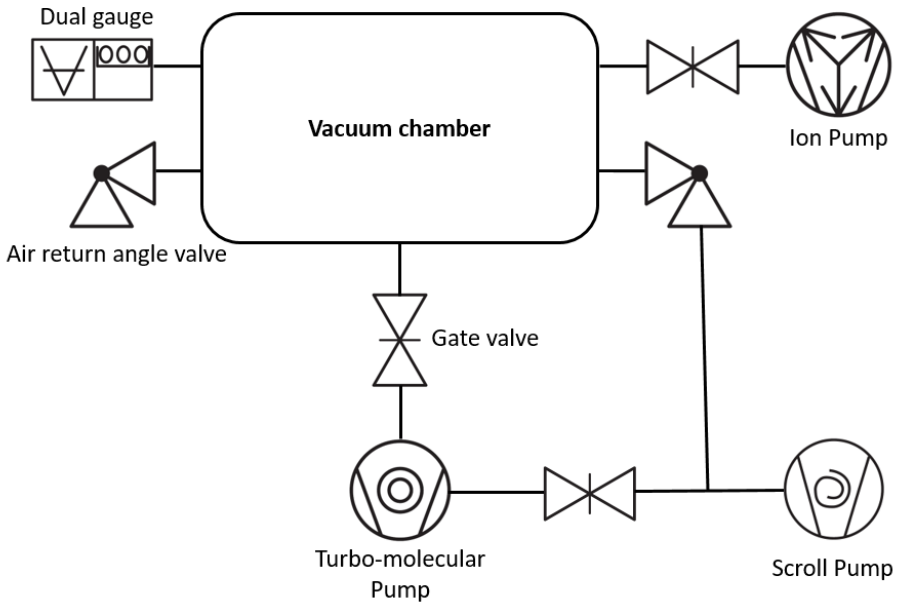

Figure 4.3: Scheme of the vacuum system.

Temperature evaluation on a twin sample

A platinum resistance thermometer (Pt-1000) is used to evaluate the temperature on a twin sample inside the vacuum chamber. The circuit diagram is represented in Figure 4.4.

In this circuit R_1 and R_2 are equal to 20 kΩ and R_3 is equal to 1 kΩ. The resistance value of the Pt-1000 depends on the temperature: it is equal to 1 kΩ at 0°C and increases for higher temperatures. The platinum material has

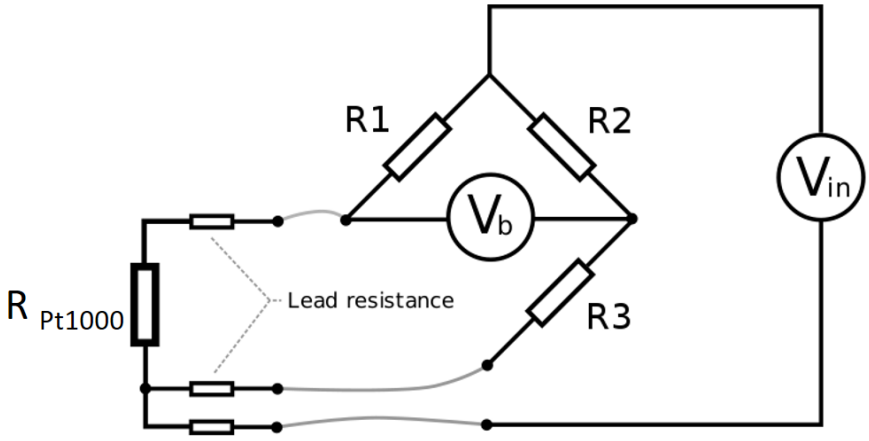

Figure 4.4: Circuit scheme for the temperature readout, using a platinum resistance thermometer. R_1, R_2, R_3 represent three resistances with known constant values and R_{Pt1000} is the resistance of the platinum thermometer that depends on temperature. V_{in} is the input voltage and V_b is the acquired voltage. This configuration is called *Wheatstone bridge* and allows to measure the R_{Pt1000} value with a good accuracy.

a very well known resistance/temperature relationship in the range from -200 to 1000°C. This configuration of four resistances is also known as *Wheatstone bridge*. The input voltage V_{in} is set to 5 V and the signal V_b is amplified by a factor 100 using an INA 131 operational amplifier: in this way $V_{out} = 100 \cdot V_b$. The output signal is acquired and processed using a software developed in the *LabVIEW* environment. If the temperature is 0°C, the resistance of the Pt-1000 is equal to 1 kΩ and so the potential difference V_b is equal to 0 V (the Wheatstone bridge is balanced). For different temperatures, it is possible to evaluate the Pt-1000 resistance measuring V_b and using the equation:

$$R_{Pt-1000} = \frac{R_2 V_{in} - (R_1 + R_2)V_b}{R_1 V_{in} + (R_1 + R_2)V_b} R_3 \tag{4.3}$$

and then the resistance value is converted to a temperature value by using the relationship:

$$R_{Pt-1000} = R_0(1 + At + Bt^2) \tag{4.4}$$

where R_0 is 1 kΩ, A and B are two constants equal to $3.9083 \cdot 10^{-3}$ and $-5.775 \cdot 10^{-7}$ respectively.

High Voltage excitation

An electrostatic actuator is placed $\sim$ 1 mm below the sample surface (Figure 4.7) and linked to a high voltage (HV) amplifier (0 - 800 V): in this way it is possible to polarize the sample. Moreover, a sinusoidal signal with a desired frequency is added to the high voltage signal (using an Agilent *3220A* Function Waveform Generator) in order to excite a resonant mode of the sample. It is possible to estimate some resonant frequencies of the sample using a finite element analysis simulation (as explained in chapter 6) and use those values to generate a HV sinusoidal signal. When the amplitude of the oscillations is sufficiently high, the sinusoidal signal is removed, the cable is grounded and the acquisition starts.

Optical readout

A 30 mW He-Ne laser enters horizontally from an optical window and is divided in two beams by a beam splitter (b.s.). One beam is directed on the upper surface of the suspended disk, close to the edge, where resonant modes have larger displacements as represented in Figure 4.2. Then the beam is reflected out of the chamber by a mirror and is directed on a quadrant photodetector. The laser beam path is represented in Figure 4.6 by a red dashed line. The signal is then acquired by a digital oscilloscope, by a spectrum analyzer (Stanford Research System *SR770*) and by a LabVIEW^{TM} software. The spectrum analyzer allows to produce a Fast Fourier Transformation of the signal and to detect resonance peaks with high sensitivity as reported in Figure 4.5.

The other laser beam produced by the beam splitter will be used in the future to measure multiple samples at the same time.

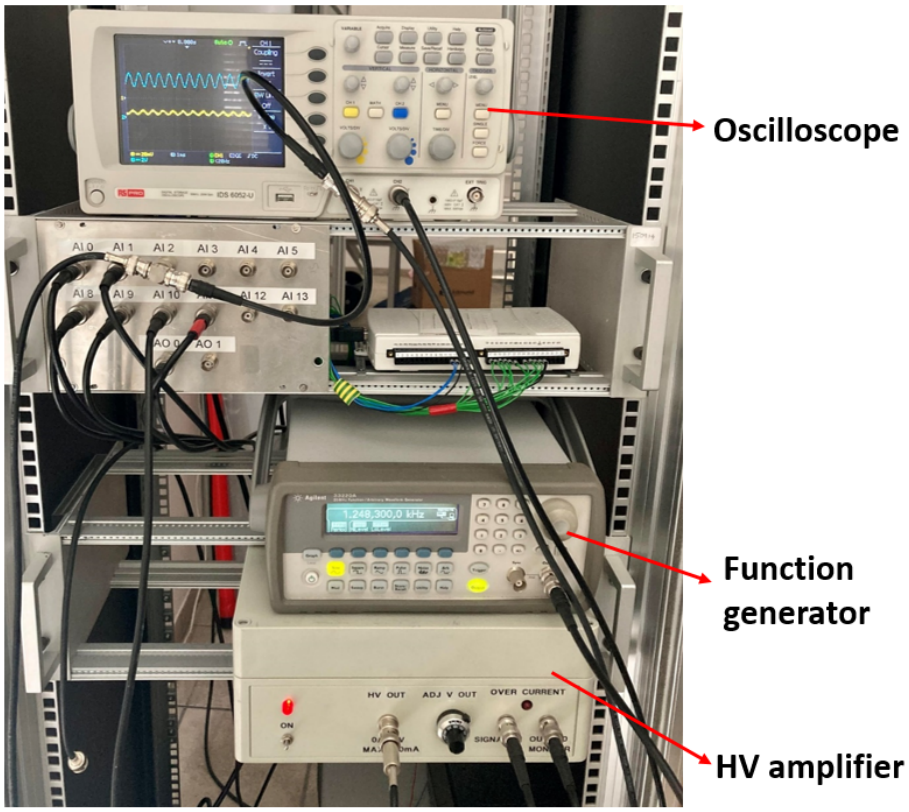

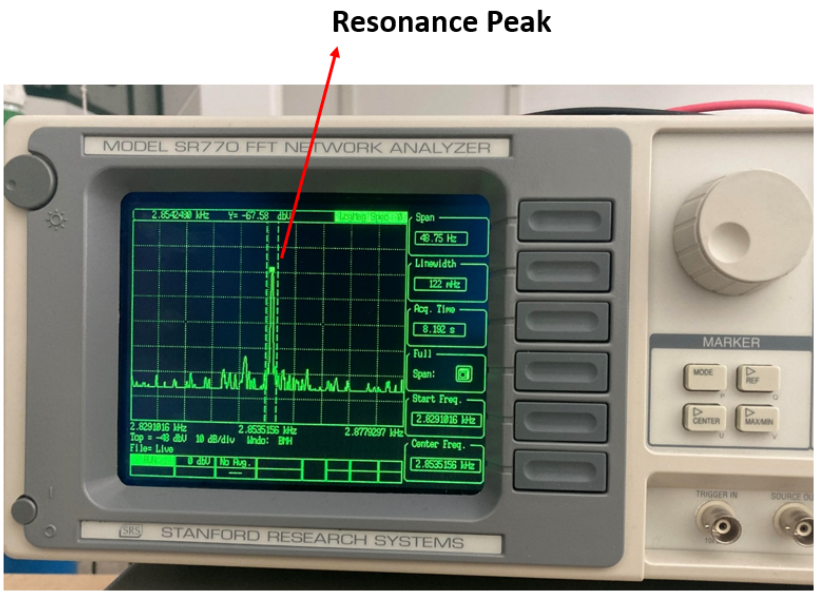

Figure 4.5: Top: Oscilloscope (yellow signal from the photodetector, blue signal from the function generator); HV amplifier linked to a function generator to create a sinusoidal signal. **Bottom:** amplitude vs frequency signal from *FFT SR770* spectrum analyzer. A resonant peak is visible in the central region of the acquired spectrum.

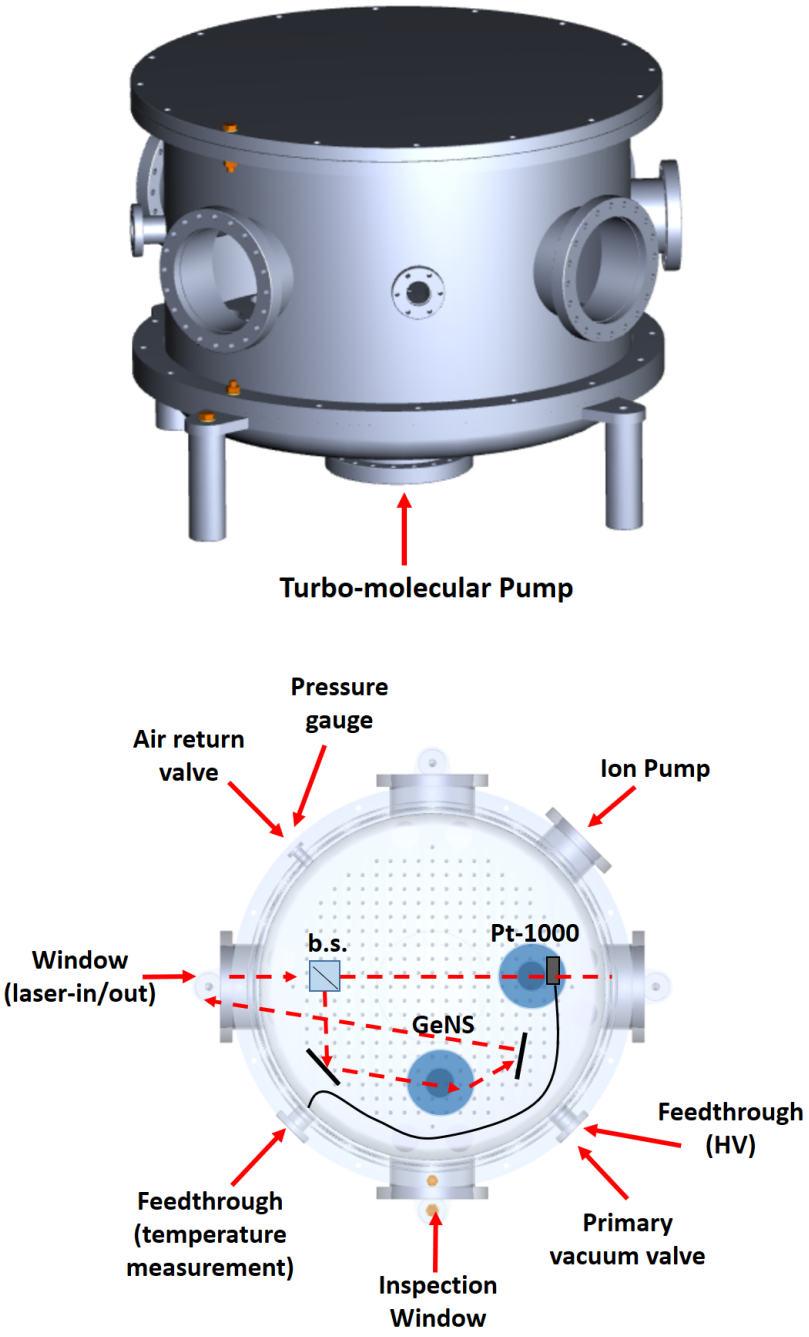

Figure 4.6: Top: 3D representation of the vacuum chamber used for the room temperature GeNS. The turbo-molecular pump is connected on the bottom flange. **Bottom:** scheme of the connections for the room temperature GeNS facility and the laser optical path (represented by a red dashed line). Two GeNS are installed: on the first one a sample is suspended for a the ring-down measurement, on the second one a sample is suspended with a Pt-1000 thermometer fixed on its surface. A beam splitter could be used to install multiple GeNS systems in the future.

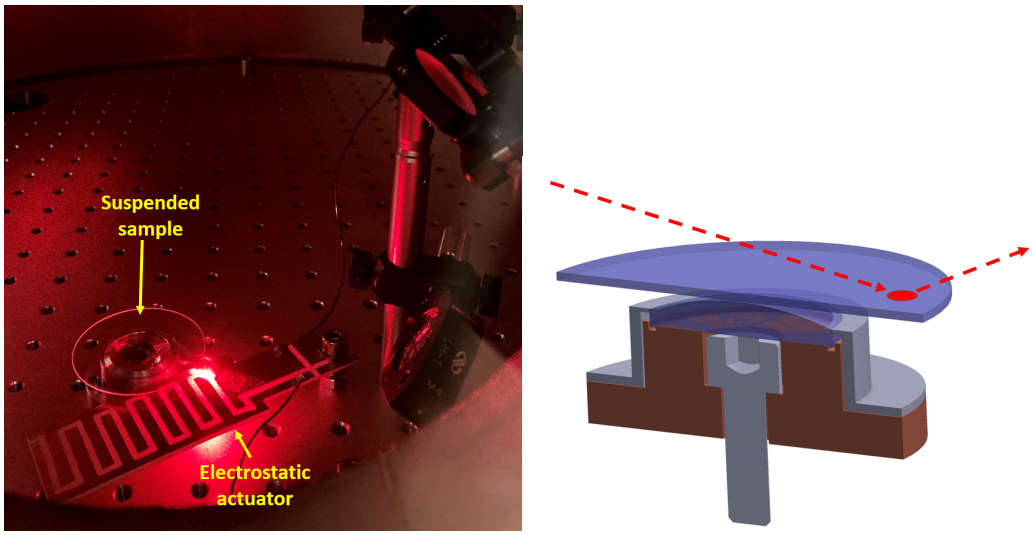

Figure 4.7: Left: a silica sample suspended on GeNS with an electrostatic actuator ~ 1 mm below its surface. A laser beam hits the upper face of the disk close to the edge. **Right:** a section view of the 3D representation of the GeNS installed inside the vacuum chamber. The red dashed line represents the laser beam.

4.1.2 Cryogenic GeNS

The cryogenic GeNS facility is similar to the room temperature one, but the experimental plate is enclosed inside a cryostat as shown in Figure 4.8. An an aluminium tank is filled with cryogenic liquids (liquid nitrogen or liquid helium). The tank is shielded by a copper shell, kept to low temperature by a surrounding pipe used to bring out the vapours from the cold inner tank. Some mylar sheets are placed around the copper shield to improve the thermal insulation. Everything is then hosted inside an external steel vacuum chamber. In this configuration the laser beam enters vertically from an optical window on the top of the chamber. One thermometer is fixed to a twin sample inside the experimental chamber (as shown in Figure 4.9) and another one is placed outside the aluminium tank to check the cryogenic liquid level. In this case two turbo-molecular pumps and two vacuum gauges are used: one for the experimental chamber and another one for the insulating environment (between the aluminium tank and the steel vacuum chamber).

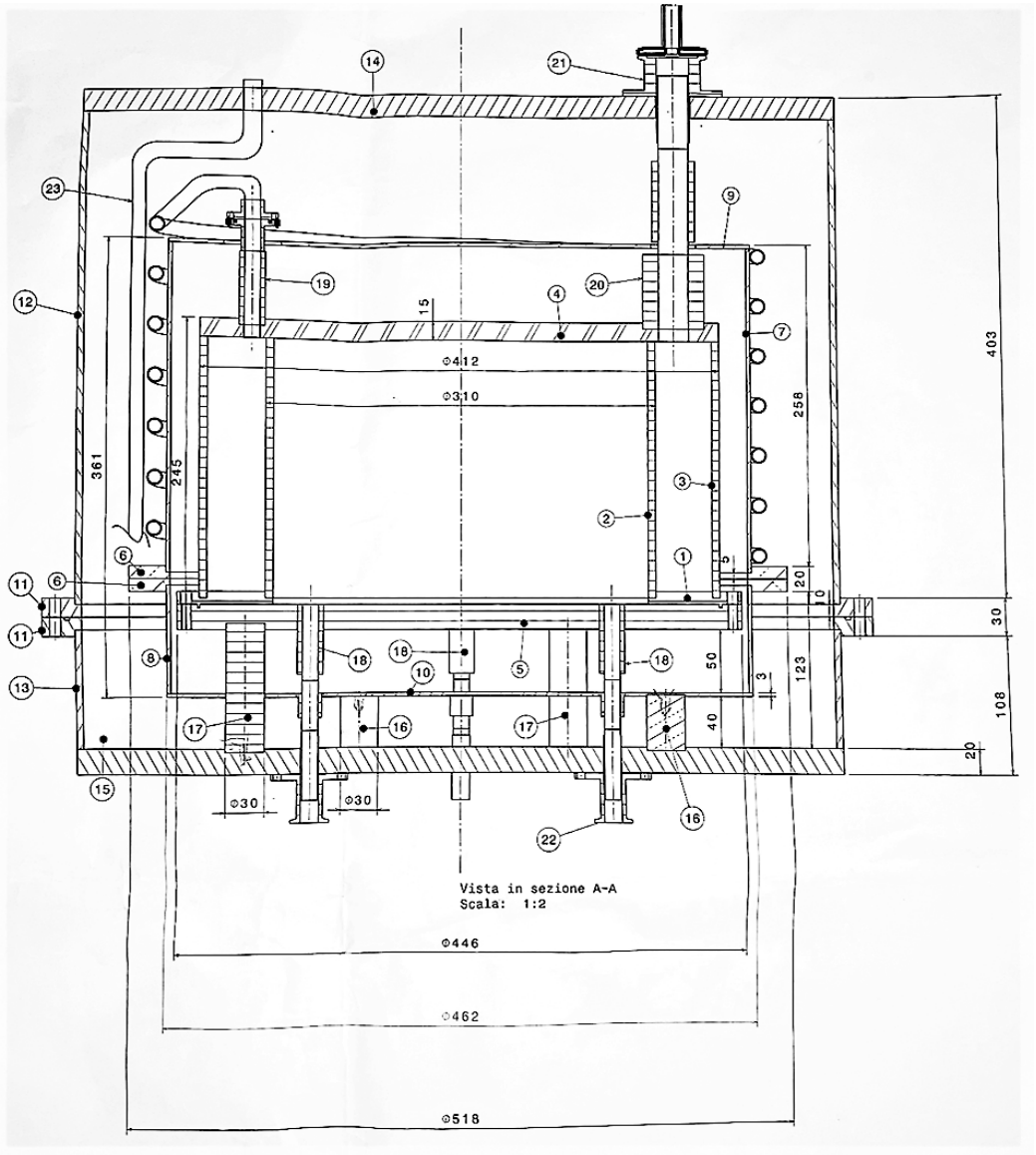

Figure 4.8: Scheme of the Cryostat used for cryogenic dissipation measurements. Liquid nitrogen or liquid helium are inserted into the internal aluminum tank from (21) and their vapours exit from (19). Those vapours pass through a pipe around the intermediate copper shield (7) and go out into the external environment (23).

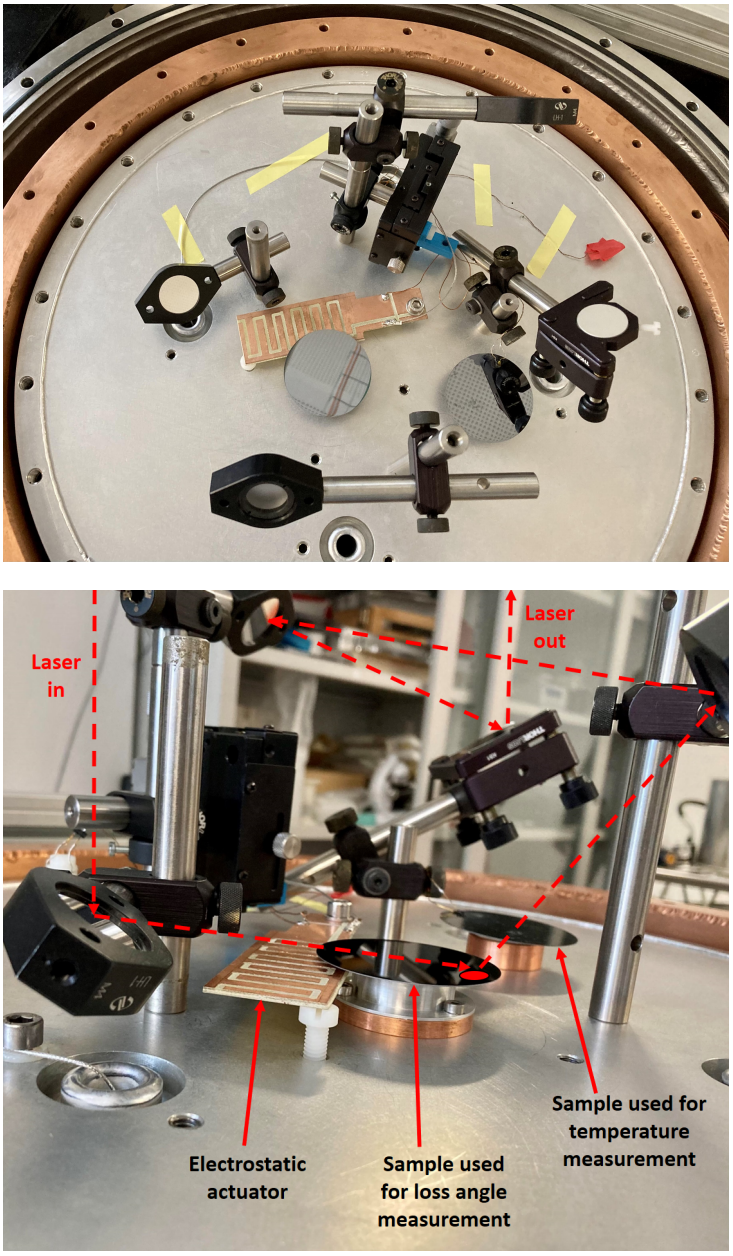

Figure 4.9: Internal view of the cryogenic GeNS facility. The laser beam (represented as a red dashed line) enters and exits vertically from two optical windows on the top of the vacuum chamber. On the experimental plate there are two twin silicon samples: the laser beam hits the first one, used for loss angle measurements; on the other one there is a thermometer fixed on its surface (barely visible in the picture).

4.2 Computer-controlled oven

It is known that post-deposition thermal treatments have an impact on optical and mechanical properties of thin film materials [56]. For this purpose, a Carbolite computer-controlled oven is used in the Urbino laboratory. This kind of oven can reach a maximum temperature of 1200 °C and thermal treatments can be performed in air, in vacuum or in controlled atmosphere (e.g. using an inert gas) depending on the kind of material that is annealed. If the annealing treatment is performed in air, two caps made of insulating wool are used to insulate the inner part of the oven. A small hole is left on the wool in order to insert a type-K thermocouple and measure directly the temperature during the treatment. If the annealing is performed in a controlled atmosphere, the configuration is that reported in Figure 4.11 is used. In this case a vacuum pump is used to remove air from the oven, then the corresponding ball valve is closed and an inert gas is inserted opening the other ball valve. The relief valve ensures that the inert gas does not exceed a critical pressure during the annealing treatment. Samples are kept inside a quartz or sapphire box (with rectified surfaces) during the treatment. Those materials have a softening temperature above typical annealing temperatures. The standard procedure (represented in Figure 4.10) is controlled using a LabVIEW software:

- the temperature is increased by 100 °C/h until the plateau temperature;
- the plateau temperature is kept constant for 10 or 20 hours;
- the temperature is decreased by 100 °C/h until room temperature.

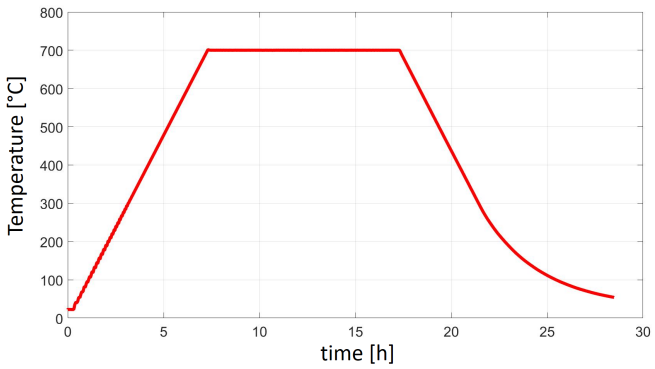

Figure 4.10: Example of an annealing treatment. The temperature is increased by 100 °C/h from room temperature to a plateau temperature, maintained constant for 10 hours and then decreased by dropping 100 °C/h.

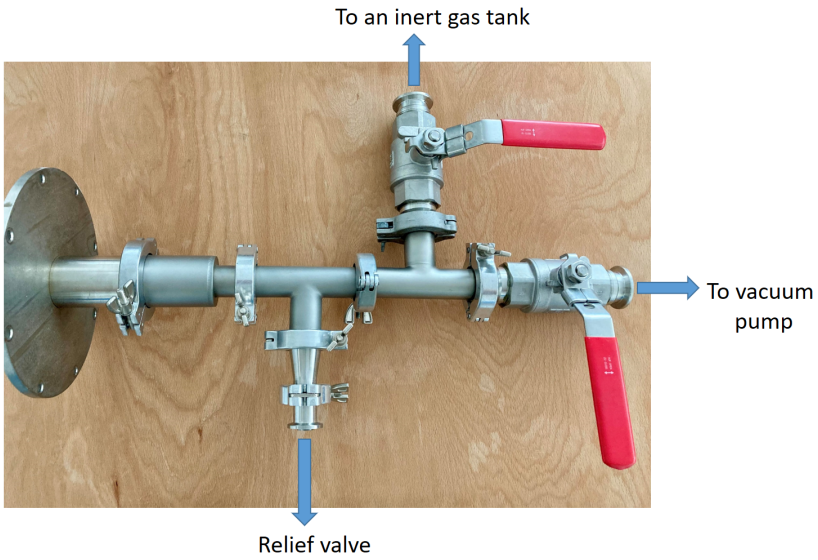

Figure 4.11: Top: configuration for annealing treatments in a controlled atmosphere. One side of the oven is closed with a blind flange and the other side is linked to an argon tank, a vacuum pump and a relief valve. **Bottom:** scheme of connections on one side of the oven. First of all, the vacuum pump is used to remove air from the oven, then the corresponding ball valve is closed and an inert gas is inserted opening the other ball valve. The relief valve ensures that the inert gas does not exceed a certain pressure value during the annealing treatment.

4.3 Curvature evaluation of a sample

A facility for measuring a sample curvature is realized using a He-Ne laser, a beam splitter, a mirror, a sample holder and a screen as represented in Figure 4.12. The laser beam is divided in two parallel beams using the beam-spitter and a mirror at 45°. The two beams are then reflected by the sample (that could be a disk or a slab) on a screen at a distance L. At the beginning a flat reference surface is used to identify the distance x between the two laser spots on the screen, then a sample with an unknown curvature is mounted and the associated distance between the two beams D is measured. The quantity δ is defined as $\delta = D - x$. If D is greater than x, then the beams are divergent (as represented in Figure 4.12) and the sample is convex; otherwise the beams are convergent and the sample is concave. The radius of curvature R can be evaluated using the relation:

$$R = 2Lx/\delta \tag{4.5}$$

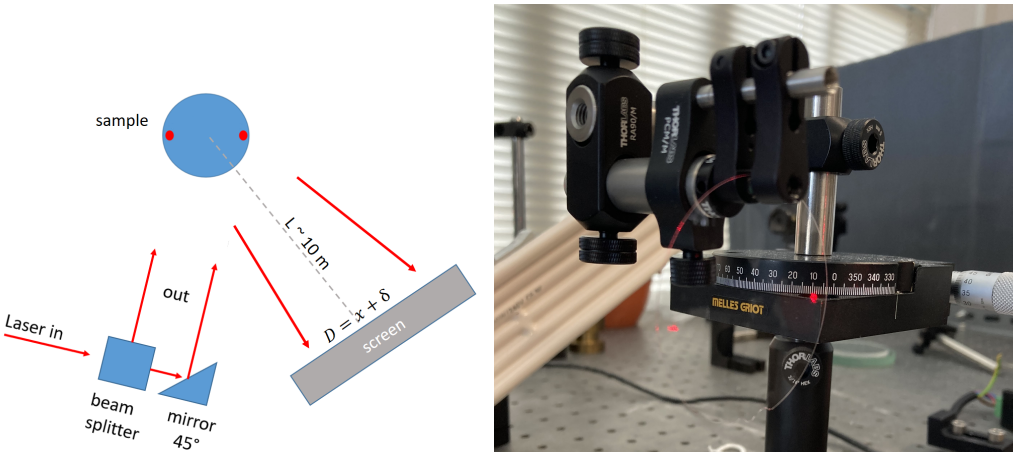

Figure 4.12: Left: scheme of the facility (not to scale). A laser is divided in two parallel beams using a beam splitter and a mirror. The two beams are reflected by the sample on a screen at a distance L. x represents the distance of the two beams reflected by a flat reference surface and D represents the distance of the two beams reflected by the sample. **Right:** a vertically held silica disk during a curvature measurement. Two laser beams are reflected from opposite sides of the sample.

4.4 Coating thermo-optic parameters evaluation

4.4.1 $\alpha + \beta/n$ evaluation

The experimental setup used for the evaluation of a linear combination of the thermo-optic parameters α and β is shown in Figure 4.13. The sample is kept in vertical position inside the tube furnace. A collimated broadband white light is reflected by the sample and focused on a fiber-coupled spectrometer. The sample temperature is measured using a Pt-1000 thermometer fixed on its surface. This facility is similar to the one developed by Gretarsson at the Embry-Riddle Aeronautical University [50]: the main difference is that the white light source and the spectrometer are on the same side of the furnace: in this way it is possible to measure the reflected light by a coated silicon substrate (instead of the transmitted light by a coated silica substrate). During a measurement the sample is heated up to 300°C and then the reflected spectra are acquired during the cooling process every 10°C. As explained in section 3.2.1 it is possible to observe the thin film interference phenomenon from the reflected broadband light by a coated silicon substrate and to have an evaluation of the coating optical length. From the variation of the optical length with temperatre it is possible to obtain the linear combination of thermo-optic parameters $\alpha_c + \beta_c/n$.

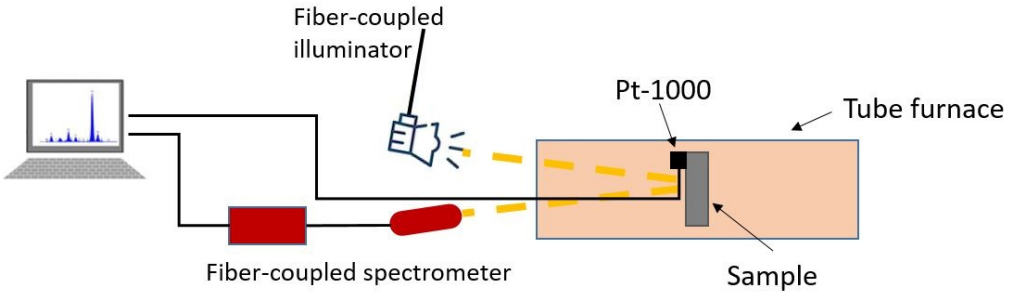

Figure 4.13: Scheme of the experimental setup.

The broadband white light source is the *OSL2* high intensity fiber-coupled illuminator by Thorlabs (Figure 4.14). This light source emits a broadband spectrum in the wavelength range of 400-1600 nm using a 150 W halogen lamp (with variable intensity control on the front panel) with an output stability of 0.5%. A fiber bundle allows to easily direct the light beam inside the oven. The light spectrum is acquired by the *CCS100/M* compact spectrometer by Thorlabs (Figure 4.14) with a wavelength range from 350 to 700 nm and a spectral accuracy of 0.5 nm. The *OSL2* lamp spectrum acquired by the *CCS100/M* spectrometer is reported in Figure 4.15.

Figure 4.14: Left: *OSL2* high intensity fiber-coupled illuminator by Thorlabs. **Right:** *CCS100/M* compact spectrometer by Thorlabs.

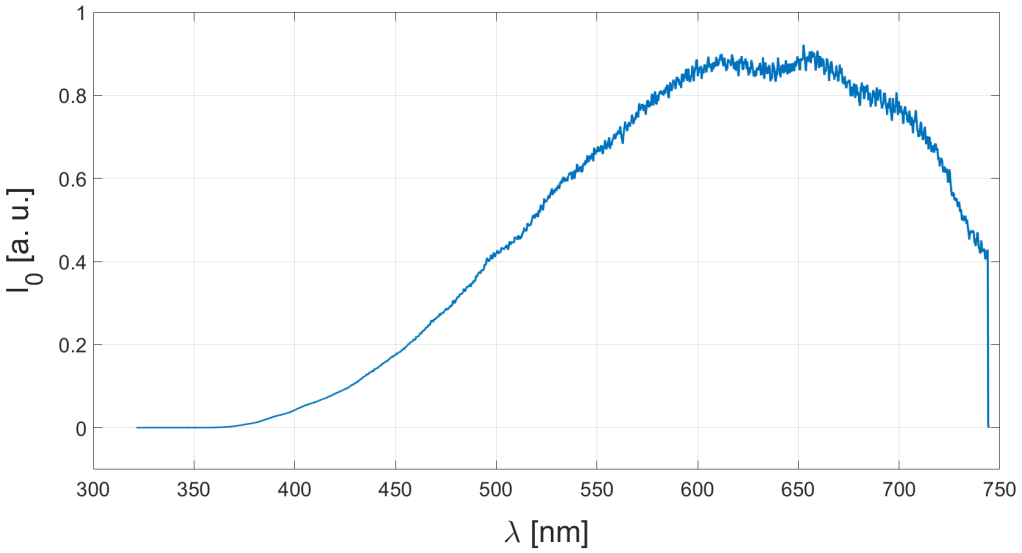

Figure 4.15: Raw lamp spectrum acquired with the *CCS100/M* spectrometer. The intensity is reported in arbitrary units (a.u.).

4.4.2 α evaluation

The same facility used for the curvature evaluation (represented in Figure 4.12) can also be exploited to measure the thermal expansion coefficient (α_c) of a coating. In this case the sample is kept in a horizontal position by a clamp. It is sufficient to add an heater near the sample, a thermometer and a thermal shield as represented in Figure 4.16.

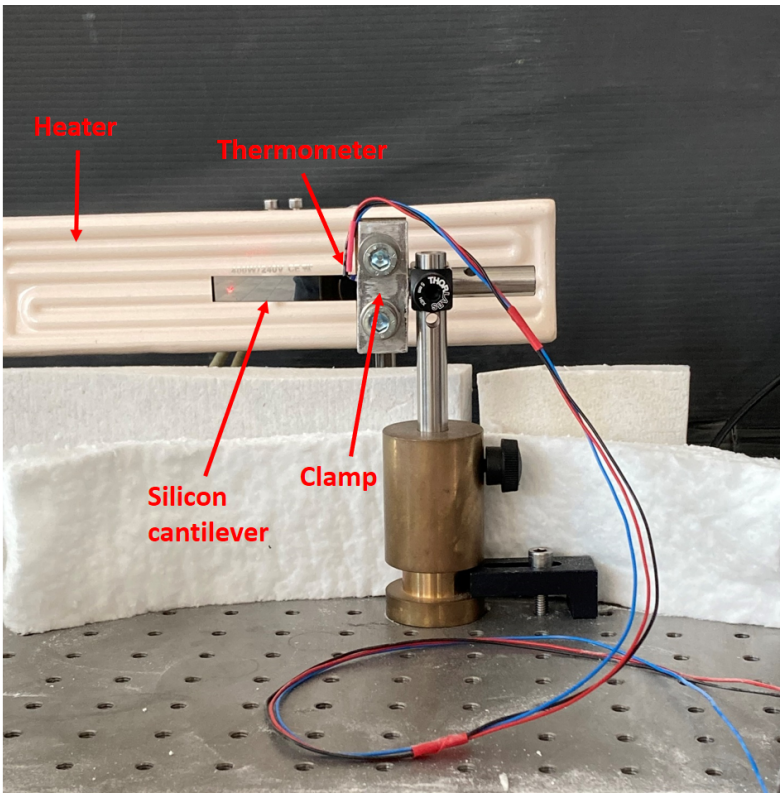

Figure 4.16: Experimental setup used for α evaluation of a coating. The coated cantilever is kept in a horizontal position by a clamp. A laser beam is reflected by the cantilever on a screen while the temperature is increased using the heater visible in the background. The sample temperature is measured using a Pt-100 thermometer between the cantilever and the clamp.

In this way it is possible to measure the overall curvature of a coated sample as a function of temperature [52]. As explained in section 3.2.2 it is possible to obtain the thermal expansion coefficient of the coating, knowing its thickness and some substrate parameters. From an experimental point of view, it is convenient to deposit the coating on a silicon cantilever with already known properties (instead of a silicon disk).

Chapter 5

Experimental results

"A scientist in his laboratory is not a mere technician:
he is also a child confronting natural phenomena that
impress him as though they were fairy tales."

Marie Curie
A Biography dy Eve Curie, 1937

Our research activities are developed within the Coating Research and Development (CRD) and inside the Virgo Coating Research and Development (VCR&D) collaborations, involving Italian and foreign universities and laboratories as represented in Figure 5.1. The aim of VCR&D is to develop new coating materials for the mirrors of future detectors, working in parallel on different research lines and following several strategies as summarized in Figure 5.2.

The Firenze/Urbino group is involved in several research lines:

- Fluorides
- Mechanical loss metrology
- Nanocoatings
- Controlled crystallization
- High coordination number glasses
- Two level systems (TLS) distribution

During my PhD I gave my contribution to some of those research lines, and the results are reported in this chapter.

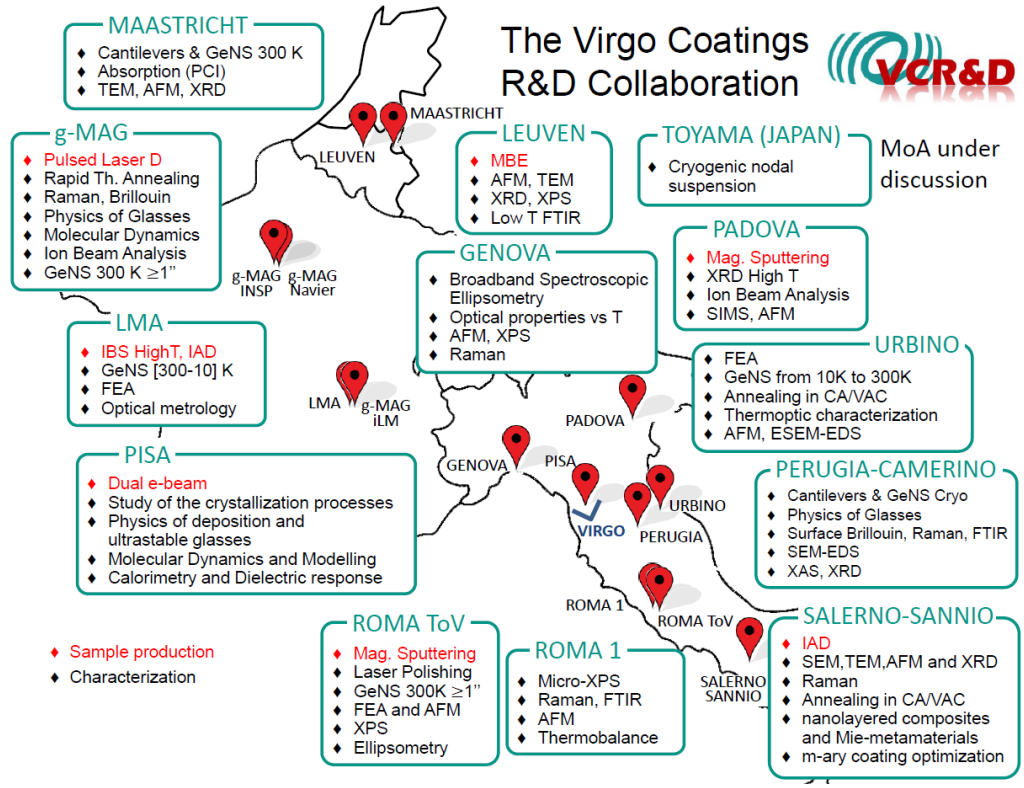

Figure 5.1: Map of the VCR&D collaboration with a list of each laboratory's facilities.

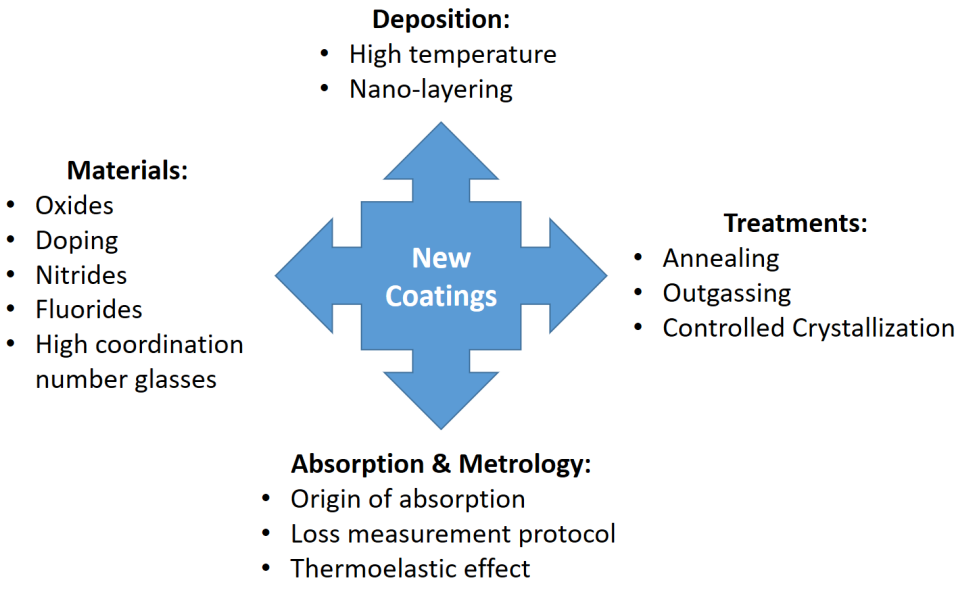

Figure 5.2: Research lines developed inside the VCR&D collaboration.

5.1 Brownian thermal noise evaluation using GeNS

As reported in section 4.1 the Gentle Nodal Suspension System (GeNS) is the preferred solution of Virgo and LIGO collaborations for performing internal friction measurements for the evaluation of Brownian thermal noise as explained in section 3.1.1.

5.1.1 Mechanical loss metrology

There are several unsolved issues related to loss angle measurements performed with a GeNS facility. The *metrology* research line was created to solve those problems and to establish a common protocol for all laboratories.

Measurement repeatability

Repeated measurements of the same sample can produce different results, probably due to a non-optimal cleaning procedure or to differences in the suspension point. Applying a cleaning protocol (using a spin coater, propanol, de-ionized water and q-tips) to remove dust and suspending the sample in its centre (using water as horizontal reference) it is usually assumed that measurement repeatability is in the range of 10% for bare substrates (with very low intrinsic losses) and 5% for coated disks 4.1. Performing ring-down experiments inside a clean room can improve the repeatability, avoiding particle deposition on the disk surface during the suspension procedure. In Figure 5.3 are reported three measurements of the same sample (a silica substrate with a diameter of 50 mm and a thickness of 0.35 mm) with error bars of 10%. Only a few resonant modes are outside the error bar, probably due to the presence of dust in a surface region involved in the oscillation of that particular resonance mode.

Dilution factor evaluation

As explained in section 3.1.1 it is possible to measure intrinsic losses of a coating material ϕ_c comparing the sample losses before and after the coating deposition, using Equation 3.11, while the Dilution Factor value for each resonant mode is obtained from Equation 3.12. A small experimental error in the mass or frequency measurement could produce a quite big error on the dilution factor and hence on the evaluation of the coating loss angle, as reported in Figure 5.4. As it can be seen in the coloured scale, it is possible

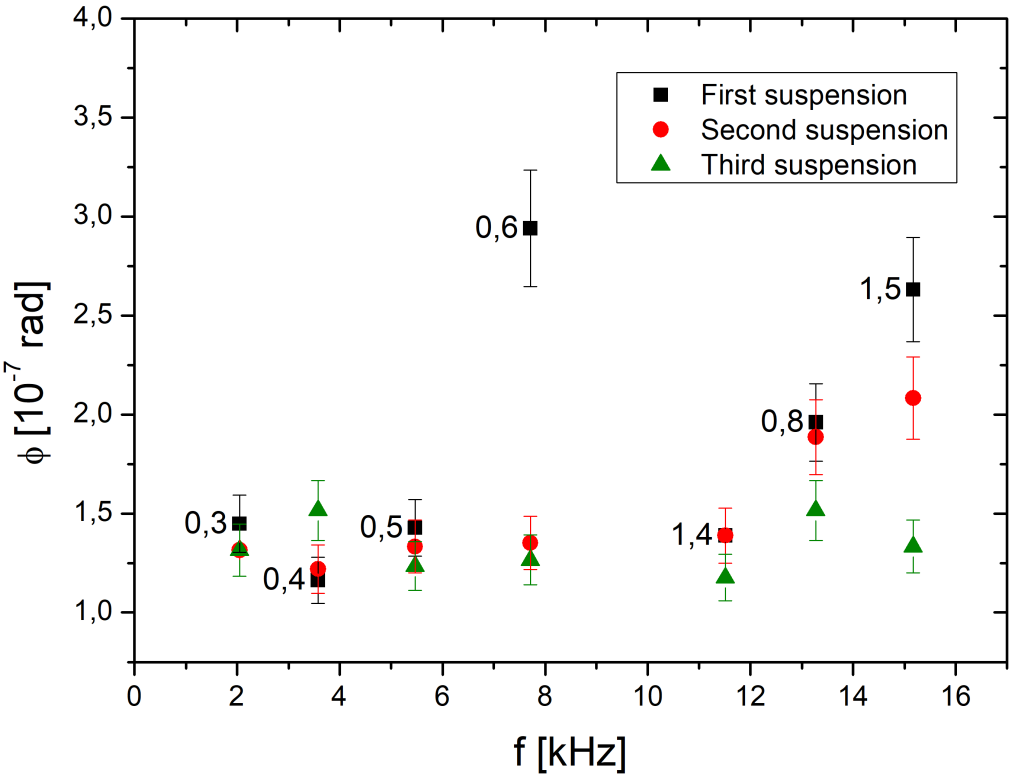

Figure 5.3: Three loss angle measurements performed on the same sample. After each measurement the disk is cleaned and suspended again. 10% error bars are reported. Those measurements were not performed inside a clean room.

to have an error as big as 15% on the dilution factor starting from an experimental error of 0.01% on both mass and resonant frequency. To overcome this problem it is necessary to use an analytic scale with a precision of 0.1 mg and a spectrum analyzer to measure the frequency of each resonant peak with high accuracy. Moreover, the substrate properties must be stable in time: the strong assumptions of equations 3.11 and 3.12 are that the variations between ϕ and ϕ_s, f and f_s and m and m_s are due only to the coating deposition. Actually, there are a lot of factors that can produce variations in the substrate properties that are not linked to the coating deposition: for example the ageing of silica material, resulting in a slow degradation of its mechanical quality over time (in particular if the disk is not kept under vacuum or its edges are not well polished [57]); a change in the disk curvature or in the temperature within subsequent measurements could produce additional frequency shifts that must be avoided or corrected *a posteriori*.

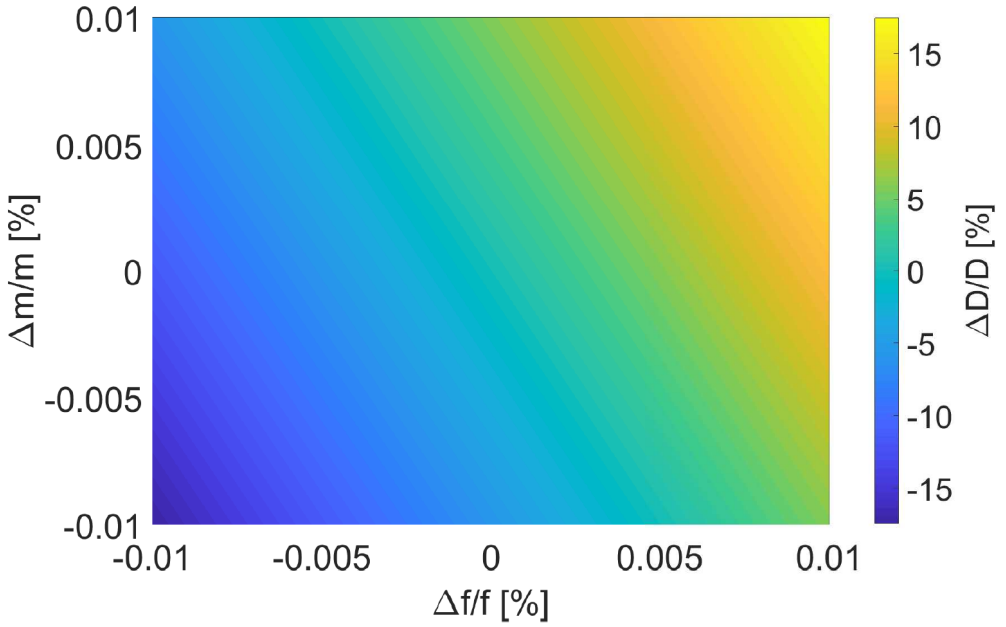

Figure 5.4: Percentage error on dilution factor ΔD/D[%] as a function of percentage errors on frequency Δf/f [%] and mass Δm/m[%].

Frequency shifts induced by temperature variations

One common issue related to the dilution factor evaluation is that the resonant frequencies of the coated substrate (f) are measured days or months after the resonant frequencies of the bare substrate (f_s) or, in some cases,

in different laboratories. In addition to the frequency shift due to the coating deposition, a frequency shift due to a temperature variation inside the laboratory can be observed. It is important to evaluate the amount of the latter shift and to subtract it *a posteriori*. For this purpose we installed a twin sample suspended on another GeNS inside the vacuum chamber with a thermometer fixed on its surface as described in section 4.1.1. In this way we can measure each resonant frequency with the corresponding sample temperature.

It is known that the Young's modulus (Y) depends on temperature following the relation [58]:

$$\frac{1}{Y}\frac{dY}{dT} = k \tag{5.1}$$

where k is a characteristic constant of each material. So, it is possible to write that $Y = Y_0 e^{kT}$. Moreover, resonant frequencies are linked to the Young's modulus by the relation $f \sim \sqrt{Y}$ [59] and so:

$$f = f_0 e^{kT/2} \tag{5.2}$$

where f_0 represents the starting frequency. It is possible to express the same dependence by the equation:

$$ln\left(\frac{f}{f_0}\right) = \frac{kT}{2} \tag{5.3}$$

Thus it is necessary to evaluate experimentally the value of k, measuring the variation of a resonant frequency with temperature. For this purpose we installed a heating strip around the vacuum chamber, then we identified the resonant frequency of the first butterfly mode (at 2486 Hz) of a fused silica disk and we followed the peak evolution with temperature. The experimental result is reported in Figure 5.5 in a semi-logarithmic scale. According to equation 5.3 a linear trend is expected with a slope equal to $k/2$.

From the linear regression we have found that the value of the k constant for a fused silica sample is:

$$k = 1.49 \cdot 10^{-4}\ \frac{1}{K} \tag{5.4}$$

In this way, it is possible to evaluate the frequency correction (Δf) associated to a resonant mode with frequency f when there is a temperature variation (ΔT) between two subsequent measurements of the same sample:

$$\Delta f = \frac{k}{2} f \Delta T \tag{5.5}$$

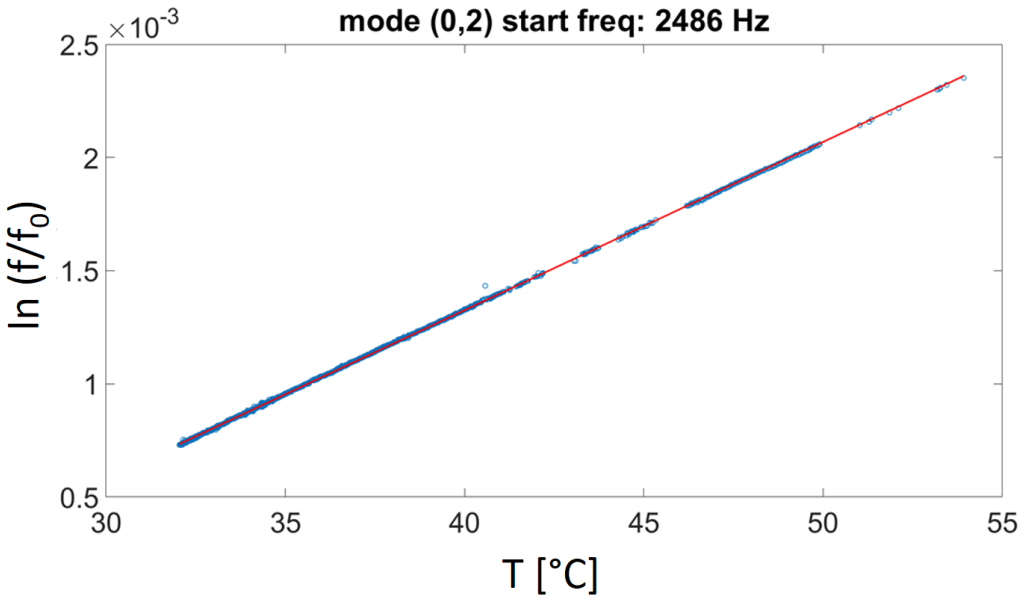

Figure 5.5: Resonant frequency dependence of the first butterfly mode (0,2) with temperature reported in a semi-logarithmic scale. The blue dots and the red line represent the experimental data and the linear fit respectively.

Frequency shifts induced by annealing treatments

Annealing treatments could produce frequency shifts and curvature variations of the substrate. We performed a set of annealing treatments, followed by frequencies measurements, curvature evaluations and finite element analysis (FEA) simulations in order to understand the physical origin of frequency shifts, to minimize the curvature and to establish an experimental procedure to stabilize the substrate resonant frequencies.

A set of samples with a diameter of 2 inches and a thickness of 0.1 mm is used. Annealings are performed using the facility reported in section 4.2 and samples are kept inside a sapphire box with rectified surfaces during the treatments. Resonant frequencies and curvature are measured before and after each treatment using the facilities described in 4.1 and 4.3 respectively. Results are reported in the following.

- **Treatments at** 900°C

  Sample A was treated in air at $T_a = 900$°C, with a duration at the plateau temperature $\Delta t_a = 20$ hours. The temperature was increased by 100°C every hour from room temperature to plateau temperature as explained in section 4.2. Resonant frequencies and curvature of

Sample A were measured before and after the annealing treatment. The percentage variation of resonance frequencies is reported in Figure 5.6.

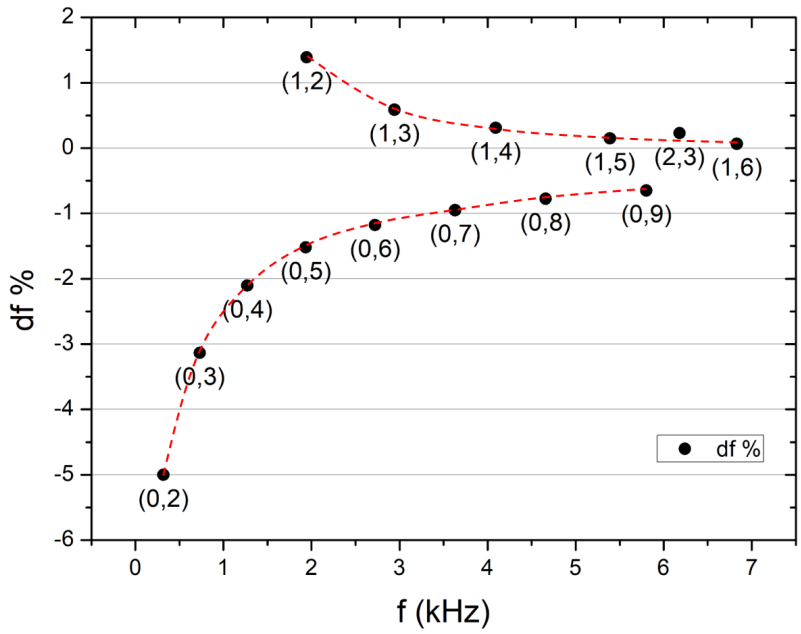

Figure 5.6: Sample A. Percentage frequency shift after the annealing at 900°C for 20 hours. Red dashed lines indicate the different behaviour of butterfly and mixed modes.

It is clear that resonant frequencies of all butterfly modes are decreased after the annealing, but at the same time resonant frequencies of all mixed modes are increased. The silica sample was nearly flat before the annealing, but after the thermal treatment on a flat sapphire surface, the sample results curved (like a dome) with a radius of curvature $R \simeq 4$ m. This effect could be due to internal stresses that are not completely released during the annealing treatment or due to a too fast cooling. Moreover the substrate seems to have become very fragile and shows some deformations on the surface that are visible with the naked eye. This particular frequency shift, with family separation, was also observed in other laboratories after annealings at high temperatures. The main problem is that this shift continues to evolve after subsequent annealings at 900°C, like observed in preliminary measurements at the Institut Lumière Matière (ILM) in Lyon. The frequency variation seems not linked to the induced curvature: in fact, flipping the disk over and repeating the annealing reduces the overall curvature, but produces a frequency shift in the same direction. Moreover, FEA

simulations predict that an increase in curvature is associated with an increment of all resonant frequencies. This prediction is confirmed by an experiment on another sample (later in this section), measuring the frequency shift of a disk that was macroscopically curved during the annealing treatment. FEA simulations predict that a variation in the Poisson ratio can produce a frequency shift that is very similar to the one observed experimentally in Figure 5.6. The frequency shift simulated changing the value of the Poisson ratio from 0.16 to 0.25 is reported in Figure 5.7.

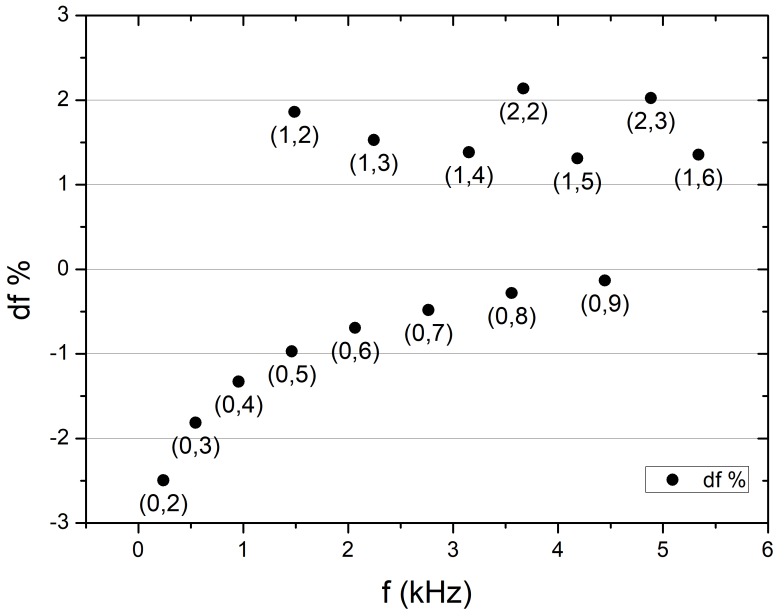

Figure 5.7: FEA simulation of a frequency shift produced by a variation of the Poisson ratio from 0.16 to 0.25.

Sample B was treated in air at $T_a = 900$°C, with a duration at plateau temperature $\Delta t_a = 10$ hours. In this case the temperature was increased by 50°C every hour from the room temperature to the plateau temperature (instead of 100°C every hour). The measured frequency shift has the same shape observed for the previous sample, reported in Figure 5.6, but the percentage frequency shift is smaller in amplitude ($\sim 1.8\%$ for the first butterfly mode and $\sim 0.8\%$ for the first mixed mode). The sample results to be nearly flat after the annealing, but shows some scratches near the edges. It is possible to conclude that measured frequency shifts are not due to a thermal shock in the sample during heating or cooling processes. It is also possible to conclude that

the plateau time (Δt_a) is an important parameter: longer plateau time produces bigger frequency shifts, and 10 hours at the plateau temperature are not sufficient to reach an equilibrium inside the material (as observed by the ILM group).

Sample C was treated in a controlled argon atmosphere (with an overpressure of 0.4 mbar) at $T_a = 900$°C, with a duration at the plateau temperature $\Delta t_a = 20$ hours. The aim of this treatment is to understand if the frequency shift is influenced by the atmosphere composition during the annealing. Argon is chosen as it is an inert gas. The measured frequency shift has the same trend as the previous samples, reported in Figure 5.6, but the percentage frequency shift is smaller in amplitude ($\sim 1.7\%$ for the first butterfly mode and $\sim 0.6\%$ for the first mixed mode).

In conclusion, there seems to be no way to avoid the frequency shift after the first annealing at 900°C. Its origin seems to be linked to a variation of the Poisson ratio and the Young's modulus of the material. Moreover, as measured by the Institut Lumière Matière (ILM), the sample has not reached a stability: resonant frequencies continue to evolve after subsequent annealings following the same trend reported in Figure 5.6.

- **Treatments at** 1000°C

  Sample D was treated in air at $T_a = 1000$°C, with a duration at the plateau temperature $\Delta t_a = 20$ hours in equilibrium on a sapphire hemisphere. Resonant frequencies and curvature of Sample D were measured before and after the treatment. The sample is maintained in equilibrium on a sapphire hemisphere during the process in order to produce a consistent curvature and understand its effect on resonant frequencies. As expected, after the thermal treatment the sample shows a macroscopic curvature, like a paraboloid. The percentage variation of resonance frequencies is reported in Figure 5.8. After the annealing all resonant frequencies are increased as predicted by FEA simulations. This experiment confirms that frequency shifts observed after annealings at 900°C are not linked to a curvature variation of the substrate, but might be associated to a variation in the Poisson ratio and Young's modulus (as predicted by FEA simulations).

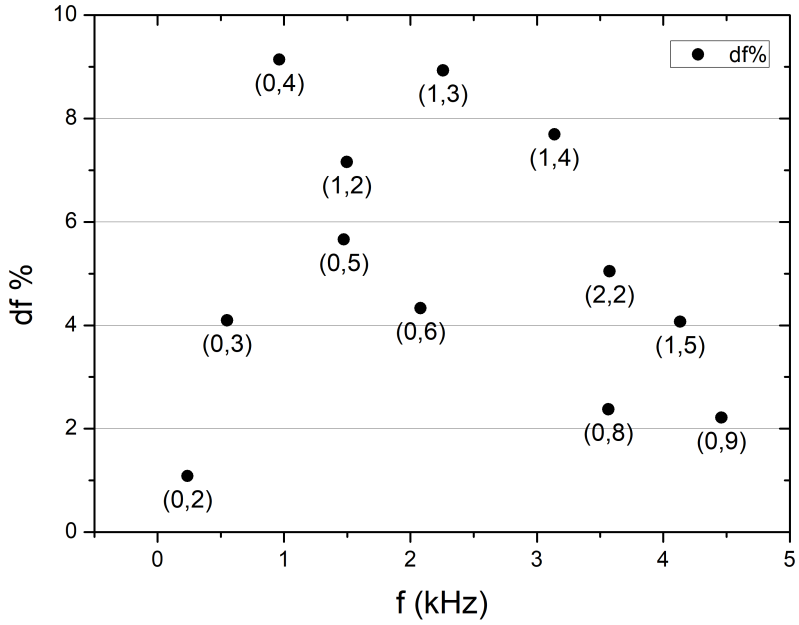

Figure 5.8: Sample D. Percentage frequency shift after the annealing at 1000°C for 20 hours in equilibrium on a sapphire sphere.

Sample E and **Sample F** were treated in air at $T_a = 1000$°C, with a duration at the plateau temperature $\Delta t_a = 20$ hours. The temperature was increased by 100°C every hour from room temperature to plateau temperature. The percentage variation of resonant frequencies of those two samples have the same trend: the variation measured on sample E is reported in Figure 5.9. It is evident that the behaviour observed after annealings at 1000°C is very different from what is measured after treatments at 900°C. Moreover, the two samples don't show cracks or deformations with the naked eye (as observed after annealing at 900°C). Sample E was nearly flat after the annealing and sample F shows a radius of curvature of 20 m along one diameter and of 3.3 m along the orthogonal direction.

Sample F was measured again after one month to evaluate if the ageing process has an impact on resonant frequencies. The sample was not stored in vacuum, but remained in air. The percentage variation of resonant frequencies due to ageing is reported in Figure 5.10. The impact of ageing on resonant frequencies is small compared to the one measured after the previous annealing treatment, but it is not negligible. Moreover, the ageing process produces a decrease in frequencies

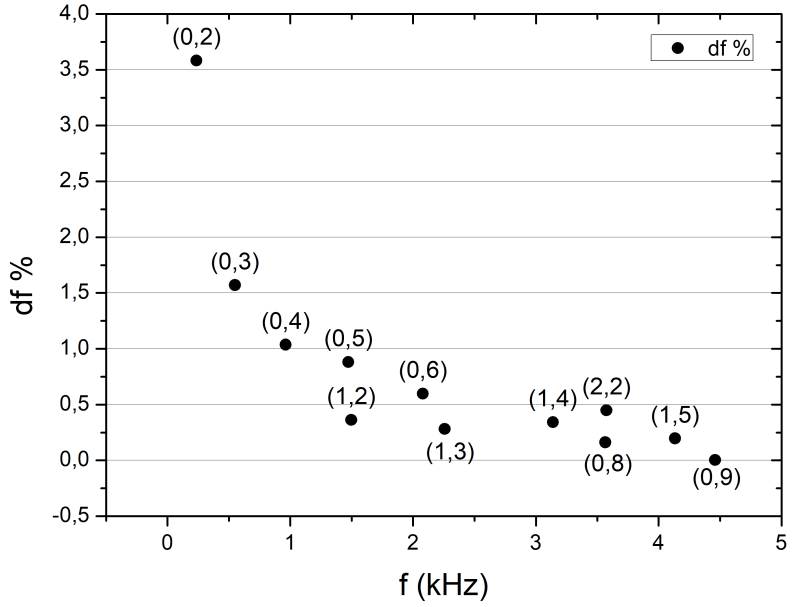

Figure 5.9: Sample E. Percentage frequency shift after the annealing at 1000°C for 20 hours on a flat surface.

that is bigger for butterfly modes and follows a similar pattern to that observed after treatments at 900°C. The origin of this shift could be the absorption of humidity by the sample surface and edges.

Sample F was annealed again in air at 1000°C, with a duration at the plateau temperature of 10 hours in order to evaluate if subsequent annealings produce another frequency shift or if the sample has reached a stability. Results are reported in Figure 5.11 and Figure 5.12. In the first graph the comparison is made between resonant frequencies measured after the first annealing and after the second treatment; in the second graph the comparison is made between resonant frequencies measured after the ageing process and after the second annealing treatment. It seems that the second annealing treatment produces a frequency shift in the opposite direction to the one observed after the ageing process (Figure 5.10). However, it is then possible to conclude that the second annealing treatment at 1000°C with a duration of 10 hours produces a small additional frequency shift: the percentage variation is less than 0.1% for almost all resonant frequencies. Moreover the shift is in the opposite direction with respect to the one produced by the ageing in air.

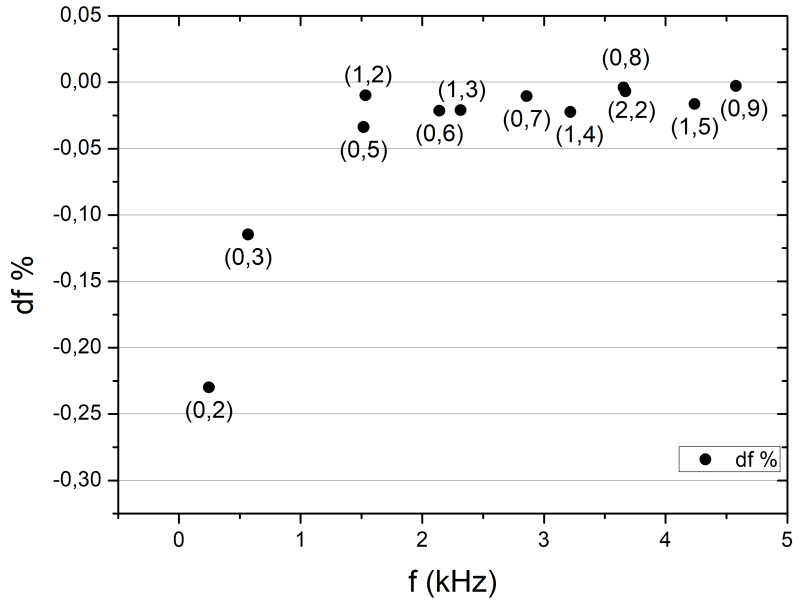

Figure 5.10: Sample F. Percentage frequency shift after one month in air due to the ageing process.

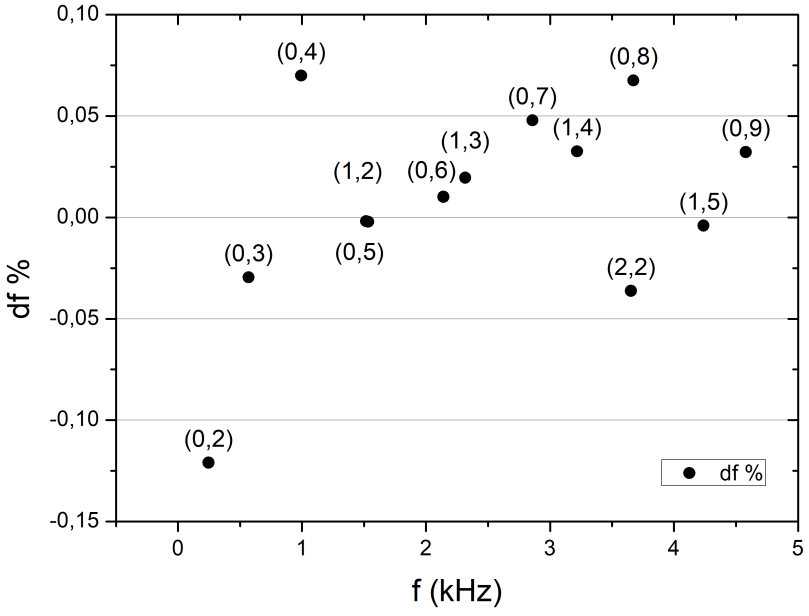

Figure 5.11: Sample F. Percentage variation of resonance frequencies of sample F after the second annealing compared to frequencies measured after the first treatment.

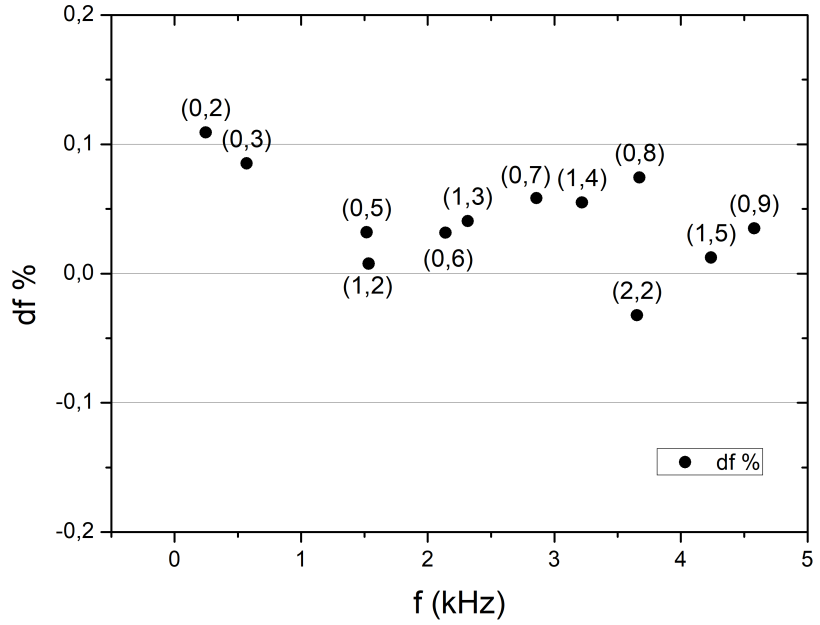

Figure 5.12: Sample F. Percentage variation of resonance frequencies of sample F after the second annealing compared to frequencies measured after the ageing.

- **Treatments at** 1100°C

  Sample G was treated in air at $T_a = 1100$°C, with a duration at the plateau temperature $\Delta t_a = 20$ hours. The temperature was increased by 100°C every hour from room temperature to plateau temperature. After the annealing the silica box used inside the oven was damaged. This effect could be due to a thermal shock during the heating or cooling process or to the presence of impurities in the silica box that were released at the plateau temperature. The sample was intact, but its surface was deformed macroscopically as reported in Figure 5.13. The percentage variation of resonant frequencies is reported in Figure 5.14. The separation between butterfly and mixed modes appears again, but every mode shows a positive shift. It is different from what is observed after the annealing at 900°C in Figure 5.6, where butterfly modes show a negative shift. It is possible to conclude that a temperature of 1100°C is too high for the treatment of silica substrates.

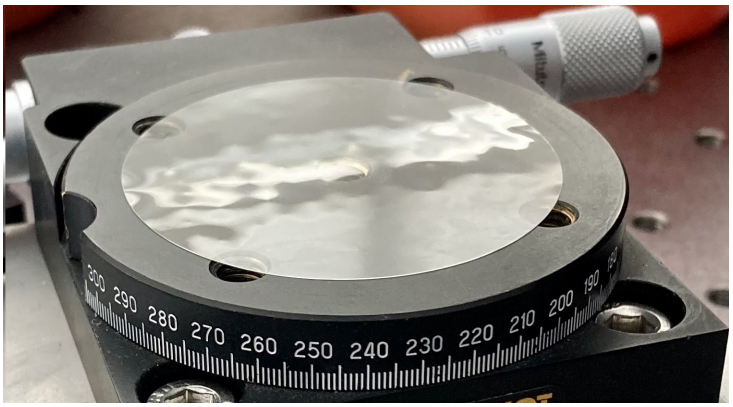

Figure 5.13: Sample G after the annealing at 1100°C. The surface shows macroscopic deformations caused by the thermal treatment.

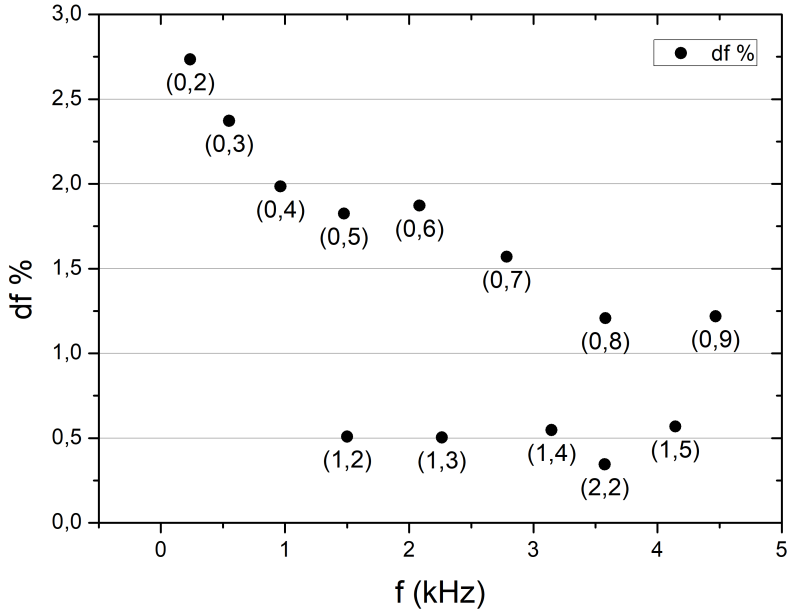

Figure 5.14: Sample G. Percentage frequency shift after the annealing at 1100°C for 20 hours. A separation between butterfly and mixed modes can be observed.

5.1.2 Fluoride coatings

In the last two decades, a lot of effort has been committed to find an alternative high refractive index material [38], that is the most dissipative one at room temperature. However, for present and future cryogenic GWDs like KAGRA [24], Einstein Telescope [26], and Cosmic Explorer [28] there is a need to find an alternative low refractive index material as well. In fact, the currently available data on ion-beam-sputtered (IBS) silica show a dramatic increase of dissipation below 30 K as reported in Figure 3.2, so silica layers should be replaced by another low refractive index material featuring low mechanical and optical losses. Because of their low refractive index [60, 61, 62, 63] and potentially low mechanical losses at low temperature [64, 59], fluoride coatings like MgF_2 and AlF_3 represent a valid option for use in cryogenic GWDs. So far, however, fluoride coatings have never been considered for implementation in GWDs, so that a characterization of their properties is needed. As a first step, in this thesis I report on the measured mechanical properties of IBS aluminium fluoride (AlF_3) and IBS magnesium fluoride (MgF_2) thin films measured at room temperature.

AlF_3 coatings

A thin layer of AlF_3 has been deposited by ion beam sputtering (IBS) at the Laser Zentrum Hannover [65] on both sides of fused silica disk substrates ($\varnothing = 50$ mm, thickness $= 1$ mm) for mechanical characterization and on one side of silicon substrates ($\varnothing$ 75 mm) for optical characterization. The coating is deposited on both sides of fused silica substrates in order to have balanced stresses and avoid deformations of the disk that could produce a variation in resonant frequencies and affect the evaluation of the frequency-dependent dilution factor. Prior to deposition, the silica disks have been annealed in air at 900°C for 10 hours to release the internal stress due to manufacturing; their masses, resonant frequencies and mechanical losses were measured at LMA [66]. Other measurements of optical absorption α, resonant frequencies, mechanical losses ϕ_c and masses of the coated samples were performed after the deposition at LMA and repeated after each thermal treatment at Urbino. Since the temperature in the two laboratories is different, a correction on measured mode frequencies is necessary for a proper evaluation of the frequency-dependent dilution factor, as explained in section 5.1.1. In order to minimize coating mechanical losses ϕ_c and optical absorption α, we tested different plateau temperatures T_a and durations Δt_a. During the annealing treatments, the samples were hold in a quartz box inside the furnace and maintained in a controlled argon atmosphere during the entire process

as explained in section 4.2. In between measurements, the samples were stored under primary vacuum ($10^{-2} - 10^{-1}$ mbar) to avoid oxidation from air exposure.

Two nominally identical silica disks (A and B) were used for the characterization of the coating mechanical properties. We measured resonant modes from ∼2.5 to ∼50 kHz for each sample, in a frequency band partially overlapping with the detection band of ground-based GWDs ($10 - 10^4$ Hz). Before and after each treatment (coating deposition, annealing runs) we measured the mass of the disks with an analytical balance and we observed the surface with an optical microscope (Olympus IX51 equipped with e ToupCam camera) to check if the coating surface was deteriorated by each treatment. Their properties are summarized in Table 5.1.

	sample A	sample B
diameter [mm]	49.94 ± 0.02	49.79 ± 0.02
thickness [mm]	1.0 ± 0.1	1.0 ± 0.1
mass before coating [mg]	4647.3 ± 0.1	4612.3 ± 0.1
mass after coating [mg]	4649.1 ± 0.1	4613.9 ± 0.1
coating thickness on each side [nm]	211 ± 6	211 ± 6

Table 5.1: Measured properties of samples A and B for the characterization of mechanical losses.

The results of the two samples *as deposited* (before the first annealing treatment) are shown in Figure 5.15. Those measurements were performed by LMA in Lyon. It is possible to describe the frequency-dependent behaviour of the coating loss angle fitting a power-law model to our data via least-squares linear regression [67, 68, 69]:

$$\phi_c(f) = a \left(\frac{f}{10 \text{ kHz}} \right)^b \tag{5.6}$$

In Table 5.2 the mechanical properties of as-deposited IBS AlF_3 (estimated by fitting finite-element simulations to measured dilution factors via least-squares numerical regression [56]) and the best-fit parameters (a,b) of the power-law model of Equation 5.6 for each sample are reported.

The two samples were then shipped to Urbino, measured again and annealed using different temperatures and times as described in Table 5.3 and Table 5.5. After each annealing we measured the loss angle ϕ of the coated disk and applying equations 3.11 and 3.12 we could measure the frequency-dependent dilution factor and extract the coating loss angle ϕ_c.

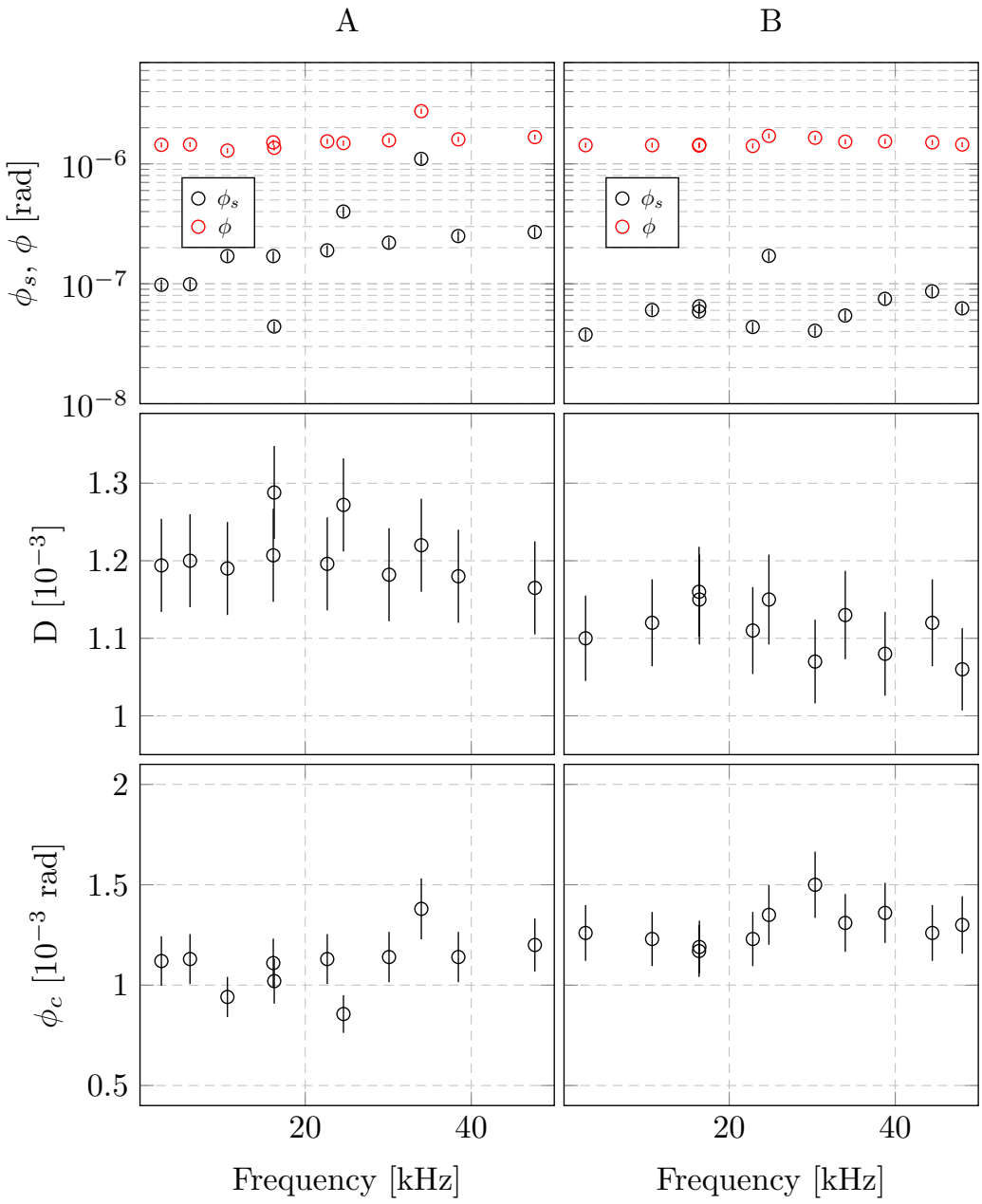

Figure 5.15: Characterization of mechanical losses, as function of frequency, of sample A (*left column*) and sample B (*right column*). **Top row:** measured losses of the bare substrate ϕ_s (in black) and coated substrate ϕ (in red). **Middle row:** frequency-dependent dilution factor. **Bottom row:** coating loss angle (ϕ_c) of as-deposited IBS AlF_3. The black dashed line represent the best fit of the power-law model. All measurements were performed by LMA.

	Y [GPa]	σ	a [10^{-3} rad]	b
disk A	78 ± 2	0.27 ± 0.02	1.06 ± 0.06	0.02 ± 0.06
disk B	72 ± 1	0.22 ± 0.03	1.25 ± 0.04	0.03 ± 0.03

Table 5.2: Measured mechanical properties of as-deposited IBS AlF_3 thin films: Young's modulus Y, Poisson ratio σ and best-fit parameters a and b of the power-law model of equation 5.6.

- **Sample A** underwent a series of annealing treatments of equal Δt_a but of increasing T_a (Table 5.3) following the procedure described in section 4.2.

run	#1	#2	#3	#4	#5	#6	#7
T_a[°C]	120	200	285	330	373	462	550
Δt_a [h]	10	10	10	10	10	10	10

Table 5.3: Annealing treatments applied to sample A.

The variations of the dilution factor and coating loss angle with annealing temperature are reported in Figure 5.16. The first set of data (reported arbitrarily at $T_a = 0$°C) represents the measured values (at Urbino laboartory) before the first annealing. The (r, a) notation denotes different vibrational modes with r radial and a azimuthal nodes.

From Figure 5.16 it is possible to see that the dilution factor increases until the treatment at 373°C and that the coating loss angle decreases after each annealing until the treatment at 373°C. The annealing temperature that minimizes the coating loss angle is between 285°C and 373°C. The mass of the sample remains unchanged until the treatment at 373°C then starts to decrease of 0.3 mg after the annealing at 462°C and 0.4 mg after the last annealing at 550°C. So, after the last treatment, we have lost 0.7 out of 2 mg of coating material. Moreover, using the optical microscope, we started to observe some round structures on the surface of the coating after the treatment at 330°C. An example is reported in Figure 5.17. After the treatment at 550°C the appearance of the coating changed: the side in contact with the quartz box used inside the furnace during the annealing looked opaque in the centre as shown in the right side of Figure 5.17. The morphology of the coating, measured with an atomic force microscope (AFM), appeared very different on the two sides of the sample: the roughness of the side in

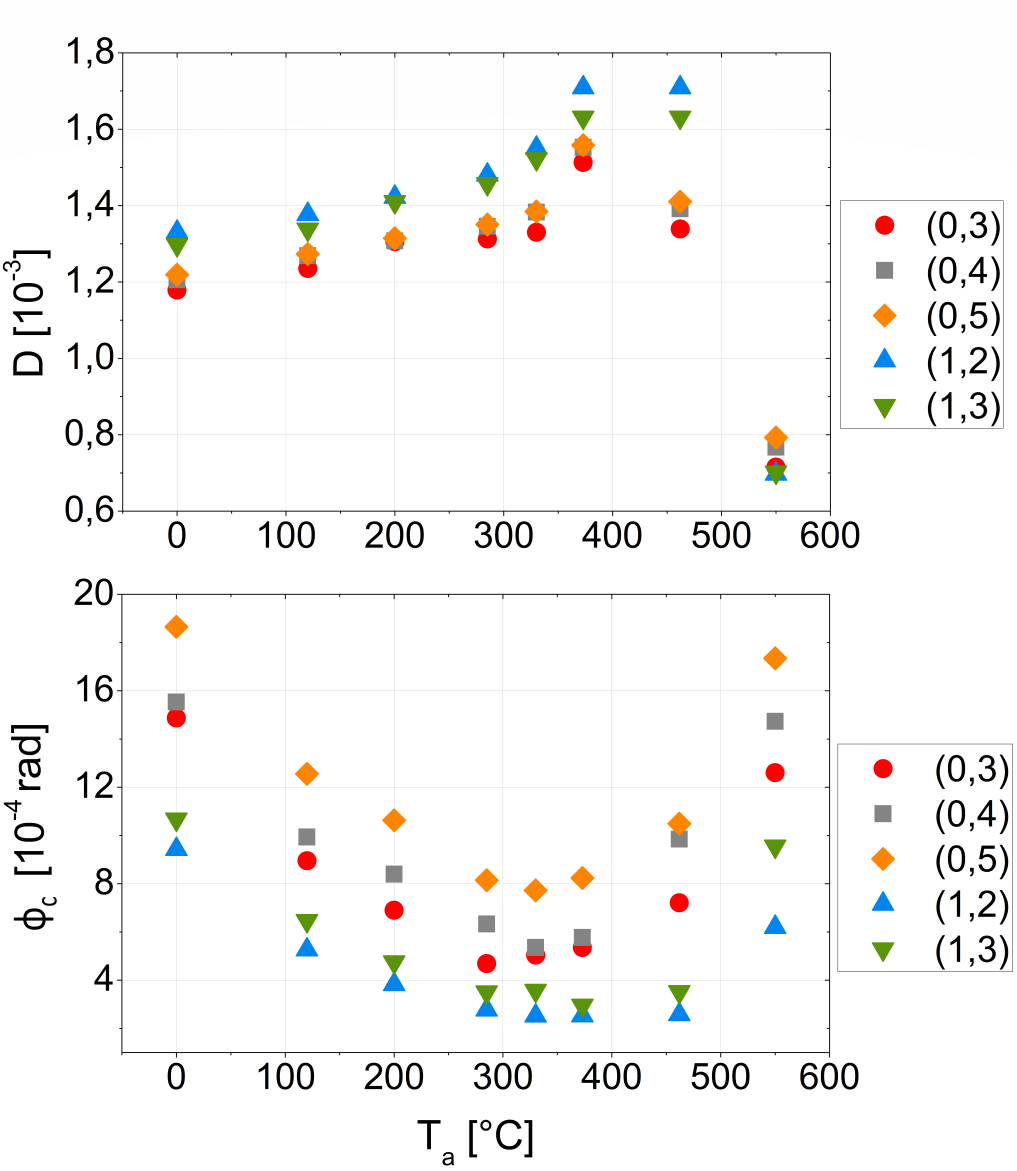

Figure 5.16: Sample A. Evolution of the dilution factor (top) and coating loss angle (bottom) with different annealing temperatures for some resonant modes. Error bars are $\sim 5\%$ in dilution factor measurements and $\sim 8\%$ in loss angle measurements.

contact with the quartz box is reported in the left side of Figure 5.18.

Moreover, we observed the surface and chemical composition of the sample with an enviromental scanning electron microscope (ESEM) *FEI quanta 200 FEG* equipped with a spectrometer. On the bottom row of Figure 5.18 it is possible to observe the formation of crystals on both sides of the sample. Crystals on side (a), on the left, are coarser than on side (b), on the right. In Table 5.4 we reported the chemical compositions of the two sides measured with the spectrometer. Stoichiometry of AlF_3 is not respected: there is a deficiency of fluorine on both sides of the sample. The presence of silicon and oxygen is due to the silica substrate under the coating. It seems that fluoride reacted with the silicon contained in the quartz box during the thermal treatment at 550°C producing a volatile compound (SiF_4): this can explain the loss of mass, the defects formation on the surface and the deficiency of fluoride.

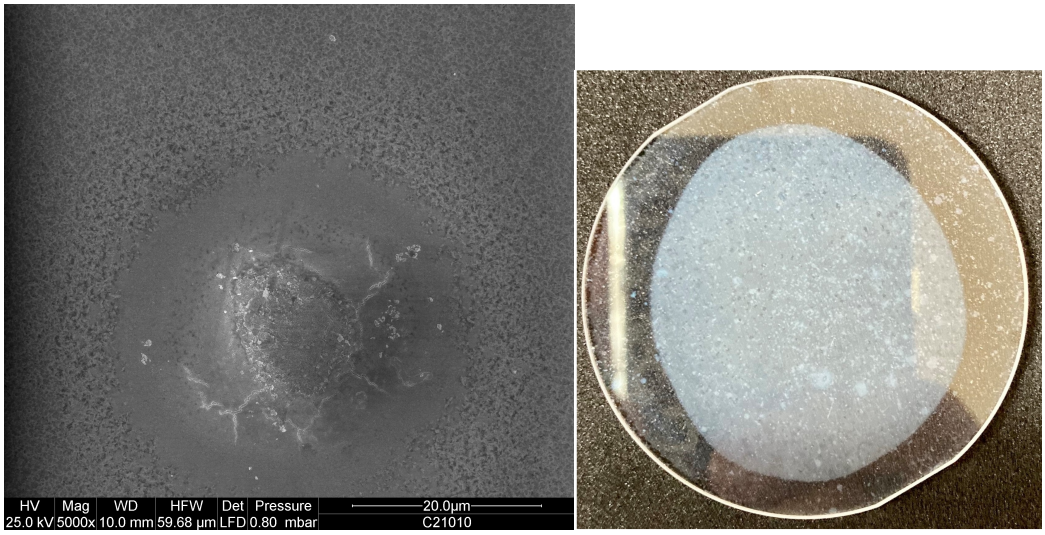

Figure 5.17: On the left: defect formation on the coating surface of sample A after the annealing at 330°C acquired with the ESEM *FEI quanta 200 FEG* with a magnification of 5000x. **On the right:** coating surface in contact with the quartz box after the annealing at 550°C.

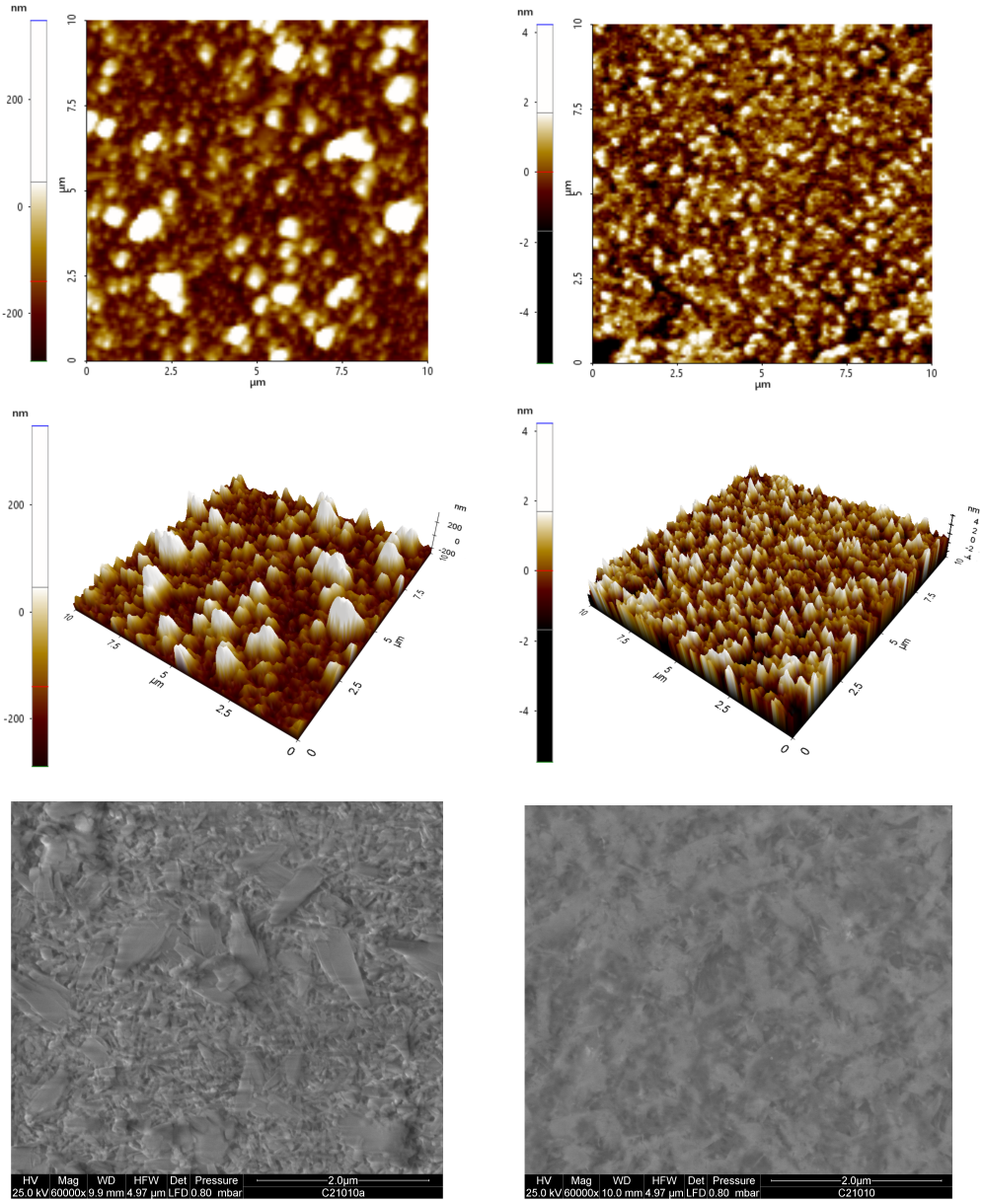

Figure 5.18: Top and middle rows: morphology of the two sides of Sample A measured with AFM *XE100 Park System Inc.* Side (a), on the left, was in contact with the quartz box during the annealing at 550°C and has a mean roughness of 67.21 nm; side (b), on the right, has a mean roughness of 0.614 nm. **Bottom row:** crystals formation observed on the two sides of sample A using the ESEM *FEI quanta 200 FEG* equipped with a spectrometer with a magnification of 60000x. Side (a), on the left, was in contact with the quartz box during the annealing at 550°C.

Element	Atomic % side(a)	Atomic % side(b)
O	55.3 ± 0.6	52.6 ± 0.6
F	4.4 ± 0.2	7.5 ± 0.4
Al	24.8 ± 0.6	30.8 ± 0.5
Si	15.5 ± 0.9	9.1 ± 0.7

Table 5.4: Chemical composition of sample A measured with the spectrometer after the annealing at 550°C.

- **Sample B**, nominally identical to disk A, underwent a series of annealing treatments of equal T_a but of increasing Δt_a (Table 5.5). "Cumulative duration" indicates the total amount of time at the plateau temperature.

run	#1	#2	#3
T_a [°C]	285	285	285
Δt_a [h]	10	20	30
Cumulative duration [h]	10	30	60

Table 5.5: Annealing treatments applied to sample B.

From the results on Sample A, 285°C was chosen as the best annealing temperature, because it minimizes the coating loss angle and seems not to produce defects on its surface. The results are reported in Figure 5.19. The first set of data ($\Delta t_a = 0$°C) represents the measured values (in the Urbino laboratory) before the first annealing. The coating loss angle decreased after the first treatment, but no more improvements were observed after subsequent annealings. The mass of the sample remained unchanged after all thermal treatments. No defects or crystals were observed using the optical microscope and the ESEM.

The chemical compositions of the two sides measured with the spectrometer are reported in Table 5.6. In this case, there is more fluoride than aluminium as expected, but the stoichiometry is not respected.

In conclusion, from a mechanical point of view, the best annealing temperature is found to be 285°C (from the analysis of *Sample A*) and a duration of 10 hours at the plateau temperature is sufficient to reach a minimum in the coating loss angle (from the analysis of *Sample B*). Higher annealing temperatures could produce defects on the coating surface, induce a crystallization process or a chemical reaction between the fluoride of the coating

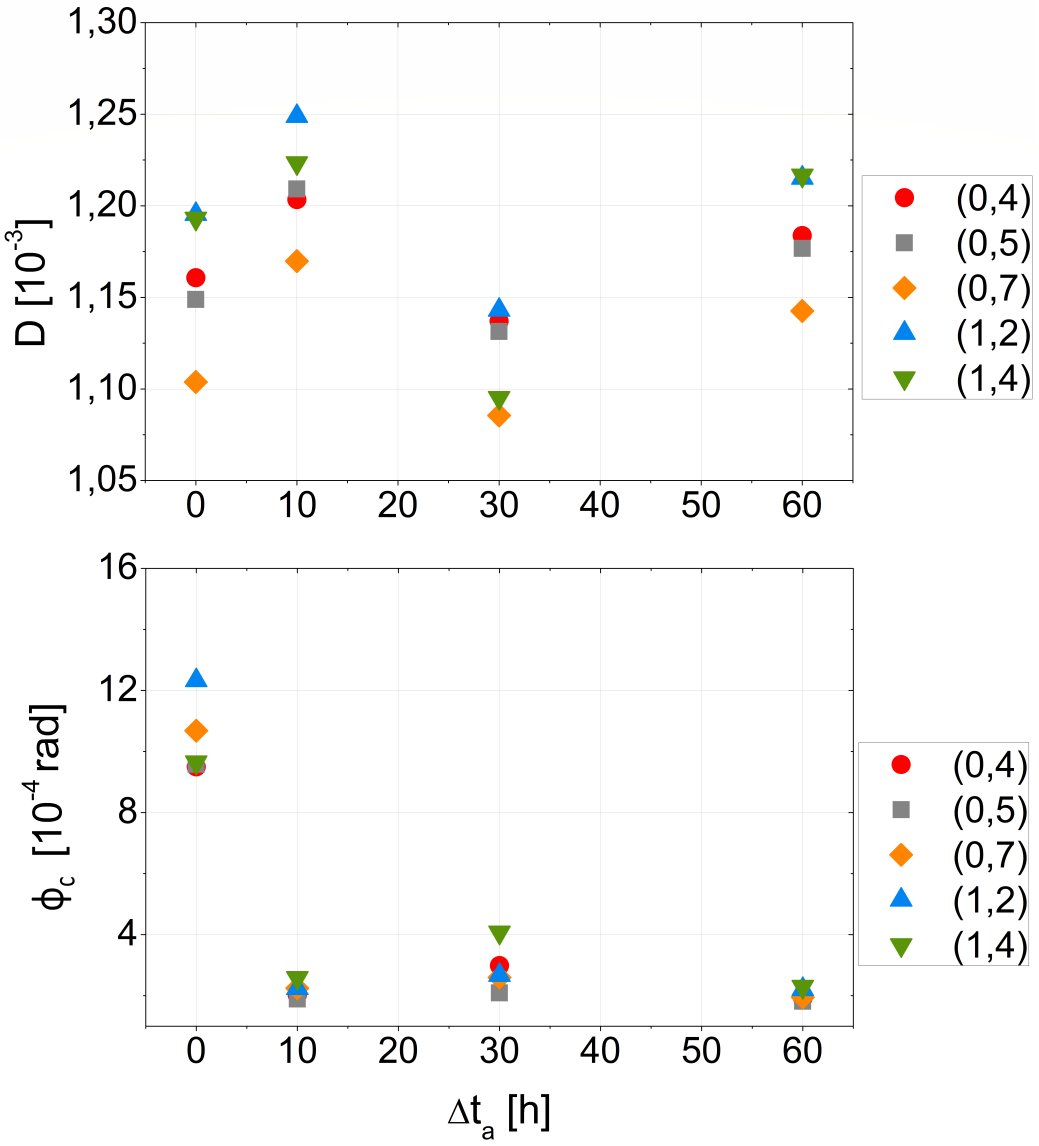

Figure 5.19: Sample B. Evolution of the dilution factor (top) and coating loss angle (bottom) with annealing cumulative time for some resonant modes. Error bars are $\sim 5\%$ in dilution factor measurements and $\sim 8\%$ in loss angle measurements.

Element	Atomic % side(a)	Atomic % side(b)
O	19.1 ± 0.4	15.2 ± 0.5
F	50.8 ± 0.4	56.1 ± 0.5
Al	28.7 ± 0.3	27.5 ± 0.4
Si	1.4 ± 0.3	1.2 ± 0.2

Table 5.6: Chemical composition of sample B measured with the spectrometer after the last annealing at 285°C

and the silicon contained in the substrate. However, mechanical losses of AlF_3 coatings at room temperature are still too high compared to those of silica coatings [38]. Further tests will be carried out in the future to explore the mechanical behaviour of AlF_3 coatings at low temperatures, where the silica loss angle increases and should be replaced by another low refractive index material as reported in Figure 3.2.

From an optical point of view, measurements performed at LMA show that the extinction coefficient increases after each annealing and is orders of magnitude higher than what is tolerable for GWDs applications [38]. In the future, efforts will be made to optimise the quality of the coating material in order to decrease the optical absorption.

MgF_2 coatings

A similar characterization to that of AlF_3 was performed on magnesium fluoride coatings. Two nominally identical silica disks (A and B) were used for the mechanical characterization and their properties are summarized in Table 5.7.

	sample A	sample B
diameter [mm]	49.77 ± 0.03	49.92 ± 0.01
thickness [mm]	1.0 ± 0.1	1.0 ± 0.1
mass before coating [mg]	4615.8 ± 0.1	4634.8 ± 0.1
mass after coating [mg]	4618.0 ± 0.1	4636.9 ± 0.1
coating thickness on each side [nm]	206 ± 2	206 ± 2

Table 5.7: Measured properties of samples A and B for the characterization of mechanical losses.

Results for the two samples *as deposited* (before the first annealing treatment) are shown in Figure 5.20. Those measurements were performed by LMA in Lyon.

In Table 5.8 are reported the mechanical properties of as-deposited IBS MgF_2 (estimated by fitting finite-element simulations to measured dilution factors via least-squares numerical regression [56]) and the best-fit parameters (a,b) of the power-law model of equation 5.6 for each sample.

	Y [GPa]	σ	a [10^{-4} rad]	b
disk A	115 ± 3	0.28 ± 0.02	6.4 ± 0.1	0.09 ± 0.02
disk B	115 ± 3	0.26 ± 0.02	5.9 ± 0.1	0.10 ± 0.02

Table 5.8: Measured mechanical properties of as-deposited IBS MgF_2 thin films: Young's modulus Y, Poisson ratio σ and best-fit parameters a and b of the power-law model of equation 5.6.

The two samples were then shipped to Urbino, measured again and annealed using different temperatures and times as described in Table 5.9 and Table 5.10. After each annealing we measured the loss angle ϕ of the coated disk and applying equations 3.11 and 3.12 we could measure the frequency-dependent dilution factor and extract the coating loss angle ϕ_c.

- **Sample A** underwent a series of treatments with increasing temperature, each one with the same plateau duration. Parameters used for the annealing treatments are reported in Table 5.9.

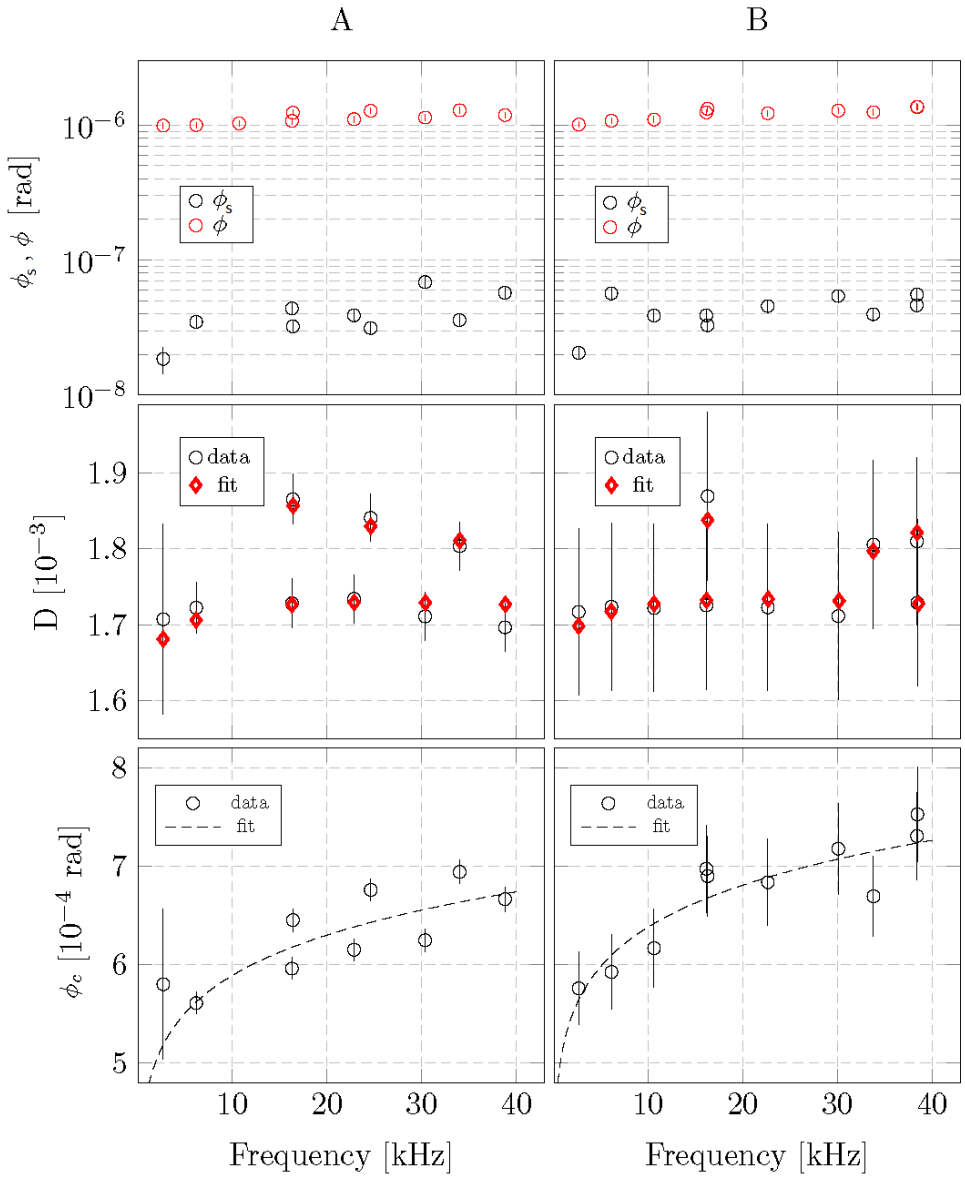

Figure 5.20: Characterization of mechanical losses, as function of frequency, of sample A (*left column*) and sample B (*right column*). **Top row:** measured losses of the bare substrate ϕ_s (in black) and coated substrate ϕ (in red). **Middle row:** frequency-dependent dilution factor. Measured values and the best fit are reported in black and in red respectively. **Bottom row:** coating loss angle ϕ_c of as-deposited IBS MgF_2 coating. The black dashed line represent the best fit of the power-law model. All measurements were performed by LMA.

run	#1	#2	#3	#4	#5
T_a[°C]	120	200	285	311	373
Δt_a [h]	10	10	10	10	10

Table 5.9: Annealing treatments applied to sample A.

The evolution of the coating loss angle of sample A is reported in Figure 5.21. The average loss angle values between the measured modes is reported. The first value ($T_a = 0$°C) represents the measured loss angle at Urbino laboratory before the first annealing treatment. The mass of the sample remained unchanged after all thermal treatments.

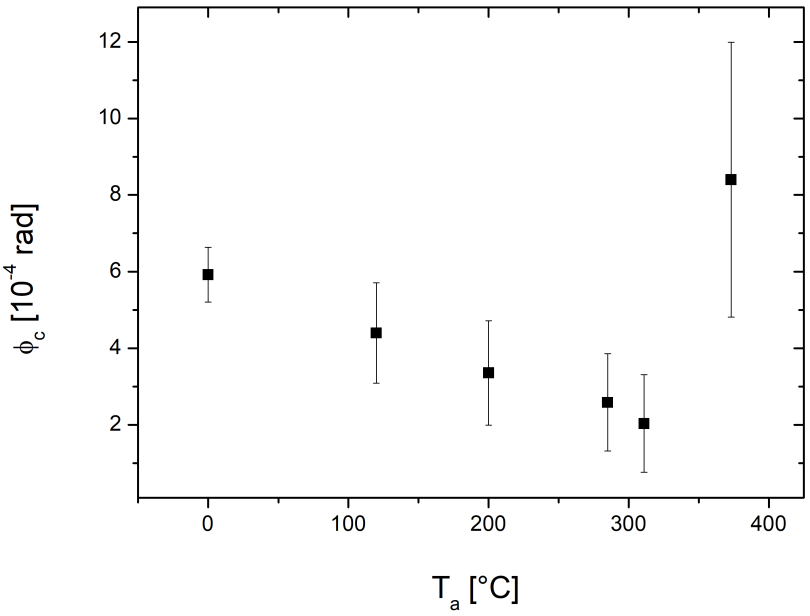

Figure 5.21: Sample A. Evolution of the coating loss angle with annealing temperature. The average value of the loss angle between the measured modes is reported.

As we increased the annealing temperature up to $T_a = 311$°C, the average coating loss angle of Sample A monotonically decreased from the initial value of $(5.9 \pm 0.7) \cdot 10^{-4}$ rad to $(2.0 \pm 1.3) \cdot 10^{-4}$ rad. After the treatment at $T_a = 373$°C, however, its average loss angle increased to $(8.4 \pm 3.6) \cdot 10^{-4}$ rad. Moreover, after the annealing at $T_a = 373$°C some cracks were observed on the coating surface with an optical mi-

croscope (reported in Figure 5.22). They might be due to the fact that SiO_2 substrate and the MgF_2 coating have different thermal expansion coefficients.

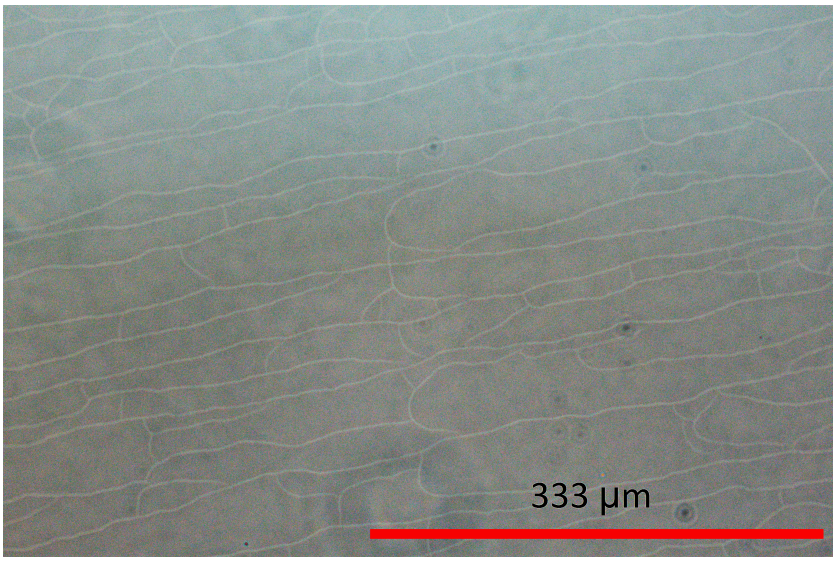

Figure 5.22: Cracks over the coating surface of sample A, observed after the annealing at 373°C.

- **Sample B**, nominally identical to disk A, underwent a series of treatments with increasing time, but at the same plateau temperature. Parameters used for the annealing tests are reported in Table 5.10. From the results on Sample A, 285°C was chosen as the best annealing temperature, because it minimizes the coating loss angle and seems not to produce cracks on the coating surface.

run	#1	#2	#3	#4
T_a [°C]	285	285	285	285
Δt_a [h]	10	20	30	64
Cumulative time [h]	10	30	60	124

Table 5.10: Annealing treatments applied to sample B.

The evolution of the coating loss angle of Sample B is reported in Figure 5.21. The first value ($t_a = 0$ h) represents the measured loss angle at UniUrb laboratory before the first annealing treatment. We reported the average loss angle value between the measured modes.

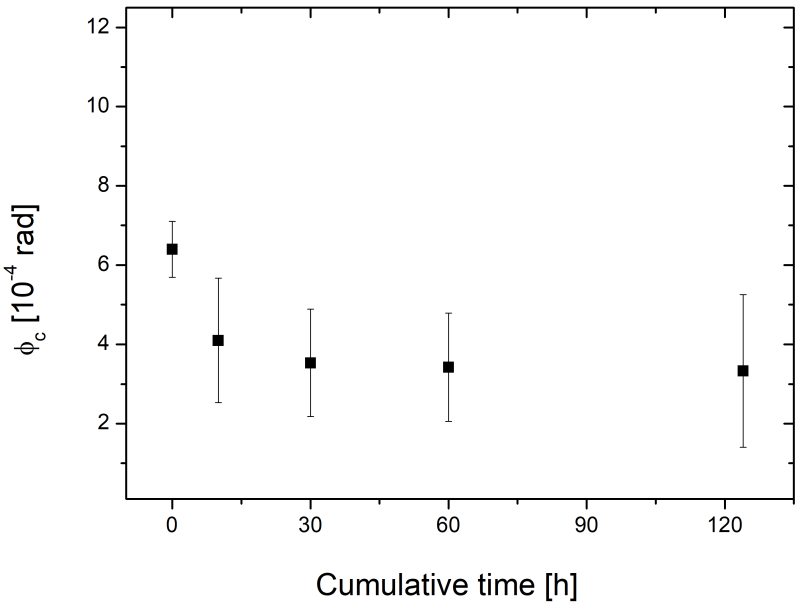

Figure 5.23: Sample B. Evolution of the coating loss angle with annealing cumulative time. The average value of the loss angle between the measured modes is reported.

The average coating loss angle of Sample B decreased after each step until the cumulative time of treatment amounted to 30 hours, where $\phi_c = (3.5 \pm 1.4) \cdot 10^{-4}$ rad. However, the variation in coating losses between a cumulative time of 10 hours and 30 hours is negligible, when compared to the measurement uncertainty.

In conclusion, from a mechanical point of view, we found that the best annealing temperature is 285°C (from the analysis of Sample A) and a duration of 10 hours at the plateau temperature is sufficient to reach a minimum in the coating loss angle (from the analysis of Sample B). Higher annealing temperatures could produce cracks on the coating surface. However, mechanical losses of MgF_2 coatings at room temperature is still too high compared to those of silica coatings [38]. From an optical point of view, measurements performed at LMA show that the extinction coefficient has a minimum after the annealing at 200°C, but is still orders of magnitude higher than what is tolerable for GWDs applications [38]. The optimization of the coating growth conditions and the measurement of the low-temperature mechanical loss of IBS MgF_2 coatings will be the object of future studies.

5.1.3 Cryogenic measurement of a silicon disk

A measurement of the loss angle of a silicon disk as a function of temperature was performed using the cryogenic GeNS facility reported in 4.1.2, using liquid nitrogen (LN) as a cooling agent. Silicon properties are already known in literature [70], so this kind of measurement was used as a test for our experimental setup. For this characterization, we have measured several times some resonant modes of the silicon disk from LN temperature ($\sim$ 77 K) to room temperature ($\sim$ 290 K). It is known [71] that near 18 K and 120 K the coefficient of thermal expansion of silicon goes to zero, implying that the thermoelastic noise should also go to zero, leaving as the main noise source the intrinsic thermal noise in silicon. As expected, a minimum in the mechanical losses is observed near 120 K as reported in Figure 5.24, measuring three resonant modes.

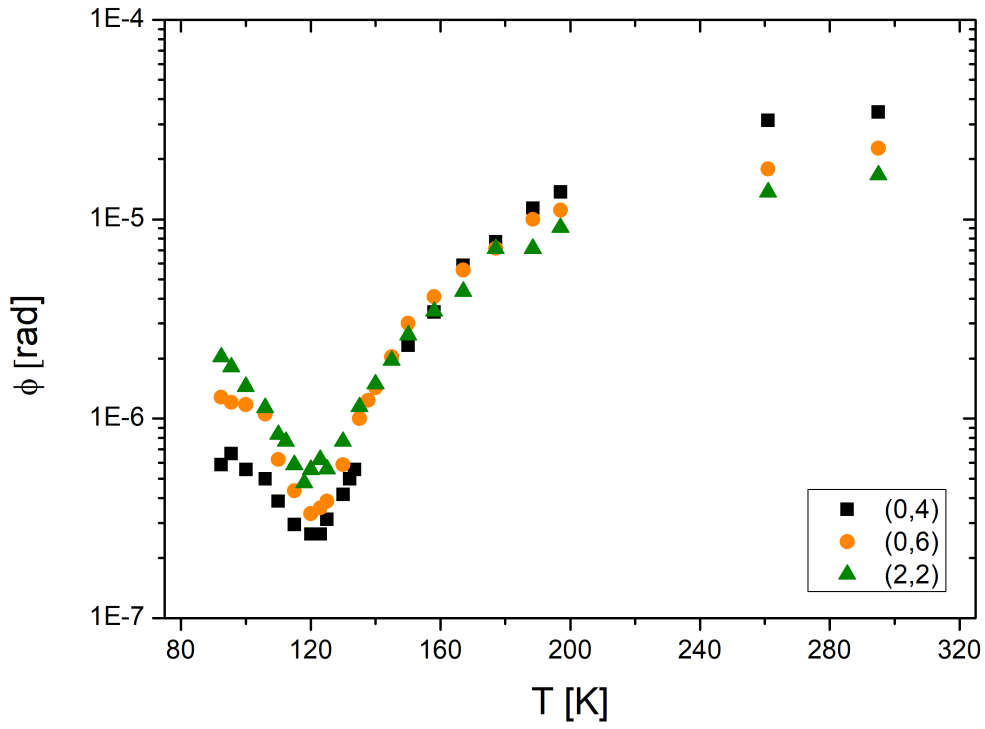

Figure 5.24: Measured loss angle of three resonant modes of a silicon disk as a function of temperature. As expected, a minimum is observed around 120 K.

5.2 Thermo-optic parameters evaluation

As explained in sections 3.2.1 and 3.2.2 it is possible to use our facilities reported in section 4.4 to evaluate the thermo-optic parameters α and β of a coating.

5.2.1 Reference Ta_2O_5 coating on a silica disk

First of all, we have tested our facility using a sample already measured by Gretarsson [50]: a tantala coating with a nominal thickness $D = (5000 \pm 300)$ nm deposited on a silica substrate. Transmitted spectra are acquired from 210°C to 80°C every 10°C and at room temperature. Each transmitted spectrum is normalized using the lamp spectrum and then, as explained in section 3.2.1, the optical length is calculated from the location of maxima and minima. The coating's optical length dependence with temperature is reported in Figure 5.25. Red stars represents the experimental data and the blue solid line is the best linear fit.

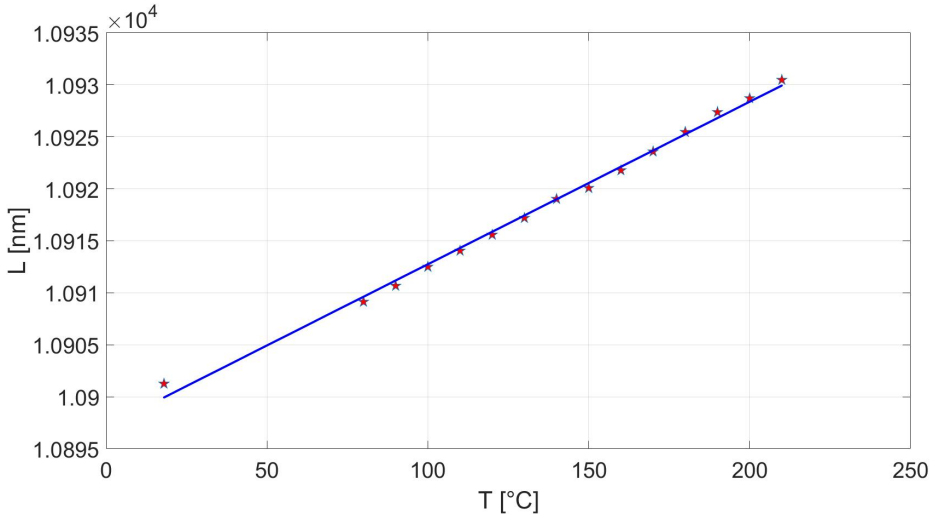

Figure 5.25: Optical length (red stars) as a function of temperature. The blue solid line represents the best linear fit.

From the slope of the linear fit we have a linear combination of the thermo-optic parameters:

$$\frac{1}{L}\frac{dL}{dT} = \alpha + \frac{\beta}{n} = (1.43 \pm 0.05) \times 10^{-5}\ K^{-1}$$

This result is compatible with the one measured by Gretarsson on the same sample [50].

From the value of the coating nominal thickness D provided by the developer (estimated from the deposition time) and from the value of the coating optical thickness L measured at room temperature it is possible to obtain the refractive index of the thin film. For this sample with a tantala coating we have:

$$n = \frac{L}{D} = 2.18 \pm 0.13$$

The refractive index is in good agreement with the value known in literature [72].

5.2.2 SiO_2 coating on a silicon disk

Another test was performed using a coating on a silicon disk, measuring the reflected spectrum instead of the transmitted one. We used a silica coating with a nominal thickness $D = (1501 \pm 20)$ nm deposited on a silicon disk. Reflected spectra are acquired from 300°C to 100°C every 10°C and at room temperature. Each spectrum is normalized using the lamp spectrum and then the optical length is calculated from the location of maxima and minima. The coating's optical length dependence with temperature is reported in Figure 5.26.

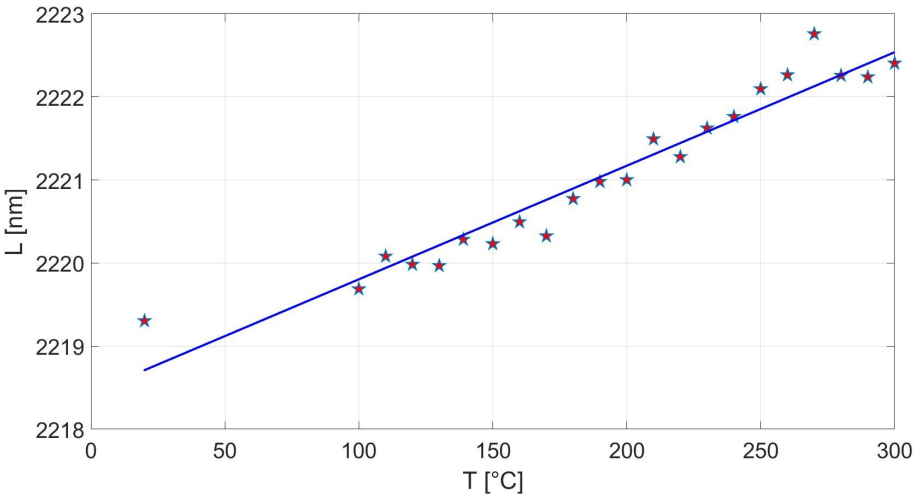

Figure 5.26: Optical length vs temperature and linear fit for SiO_2 coating.

From the slope of the linear fit we have:

$$\frac{1}{L}\frac{dL}{dT} = \alpha + \frac{\beta}{n} = (0.62 \pm 0.08) \times 10^{-5}\ K^{-1}$$

The linear fit is not good as the one reported in Figure 5.25 because, in this case, the coating thickness is smaller. However, the obtained value is in quite good agreement with α, β and n values found in literature [73]. Moreover, the quality of the reflected spectra is higher compared to the transmitted ones, so we decided to use this technique in future and deposit the coating on silicon substrates for this kind of experiments.

From the value of the coating nominal thickness D provided by the developer (estimated from the deposition time) and the value of the coating optical length L measured at room temperature, the refractive index of the coating results to be:

$$n = \frac{L}{D} = 1.5 \pm 0.2$$

The refractive index is in good agreement with the value known in literature [74].

5.2.3 SiNx coating on a silicon disk

One of the most promising material for future GWDs mirrors is the silicon nitride and so we decided to measure its thermo-optic parameters for the first time in our collaboration. In order to do so, a silicon nitride coating with a nominal thickness $D = (4200 \pm 100)\ nm$ was deposited on a silicon disk. The reflected spectrum is acquired from 290°C to 100°C every 10°C. The raw reflected spectrum at room temperature is reported in Figure 5.27. The coating's optical length dependence with temperature is reported in Figure 5.28. Red stars represents the experimental data and the blue solid line is the best linear fit. From the slope of the linear fit we have:

$$\frac{1}{L}\frac{dL}{dT} = \alpha + \frac{\beta}{n} = (1.64 \pm 0.02) \times 10^{-5}\ K^{-1}$$

From the value of the coating's nominal thickness D provided by the developer (estimated from the deposition time) and the value of the coating's optical thickness L measured at room temperature, the refractive index of the coating results to be:

$$n = \frac{L}{D} = 2.06 \pm 0.07$$

The refractive index is in good agreement with the value known in literature [75].

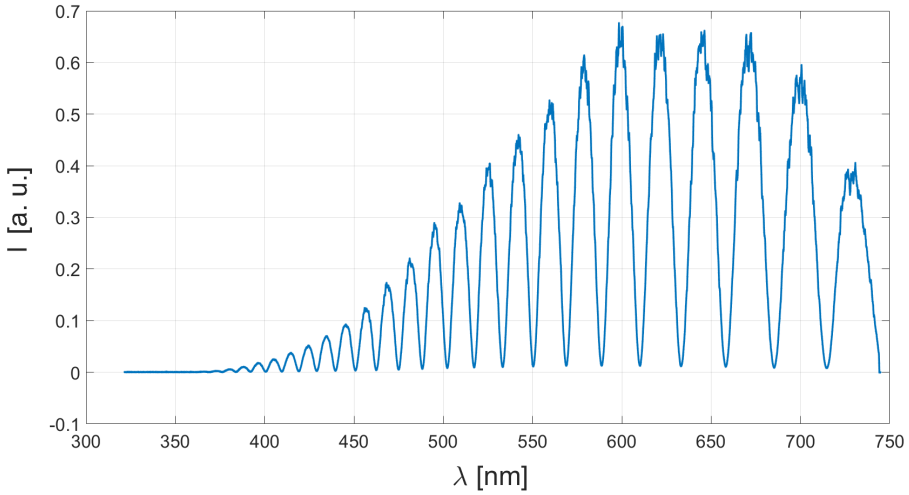

Figure 5.27: Reflected spectrum from $\sim$ 4200 nm of silicon nitride deposited on a silicon disk.

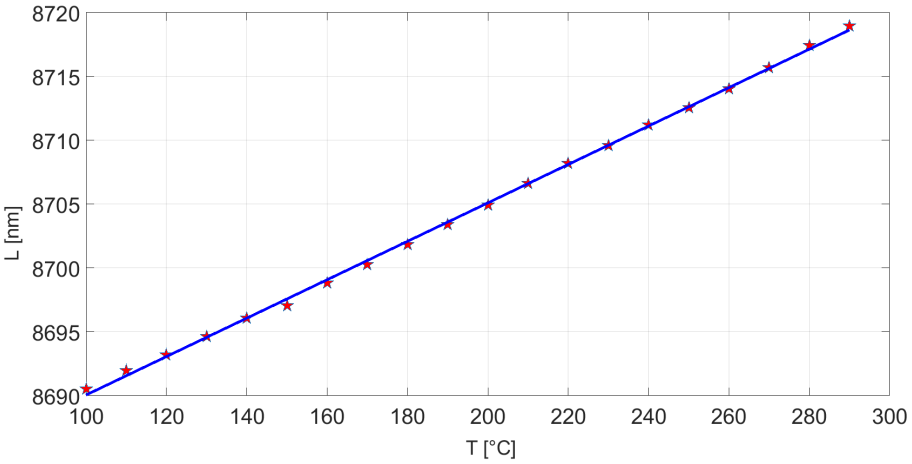

Figure 5.28: Optical length (red stars) as a function of temperature. The blue solid line represents the best linear fit.

5.2.4 Ta_2O_5 coating on silicon slab

As explained in section 3.2.2 it is possible to calculate the coating thermal expansion coefficient α_c measuring the curvature variation of a coated silicon cantilever with temperature and knowing some parameters reported in Table 5.11.

Symbol	Name	Value
x [cm]	Distance between the clamp and the laser spot	5.0 ± 0.2
L [m]	Distance from the sample to the screen)	12.00 ± 0.03
t_s [mm]	Silicon substrate thickness	0.110 ± 0.004
t_c [μm]	Tantala coating thickness	4.8 ± 0.3
α_s [K^{-1}]	Thermal expansion coefficient of silicon	$2.62 \cdot 10^{-6}$
σ_s	Poisson ratio of the silicon cantilever	0.278
σ_c	Poisson ratio of the tantala coating	0.28
Y_s [N/m^2]	Young's modulus of the silicon cantilever	$1.3 \cdot 10^{11}$
Y_c [N/m^2]	Young's modulus of the tantala coating	$1.17 \cdot 10^{11}$

Table 5.11: Parameters used to derive the thermal expansion coefficient of a tantala coating. Mechanical parameters used for the Ta_2O_5 coating are taken from [38].

Figure 5.29 shows the variation of the laser position reflected by the coated cantilever, with respect to a reference spot on a screen, with temperature (black dots) and its best linear fit (red line). Using equation 4.5 it is possible to evaluate the variation of the cantilever radius of curvature with temperature, that is linked to the variation of the coating stress with temperature (equation 3.32). Finally, using 3.33 it is possible to derive the coating thermal expansion coefficient, that results to be:

$$\alpha_c = (3.6 \pm 0.5) \cdot 10^{-6}\ K^{-1} \tag{5.7}$$

This result is in very good agreement with the value accepted by the LIGO community [76, 77]. In this way, knowing the value of the linear combination of thermo-optic parameters ($\alpha_c + \beta_c/n$) for a tantala coating, it is possible to derive the value of the thermo-optic coefficient.

$$\beta_c = (2.2 \pm 0.1) \cdot 10^{-5}\ K^{-1} \tag{5.8}$$

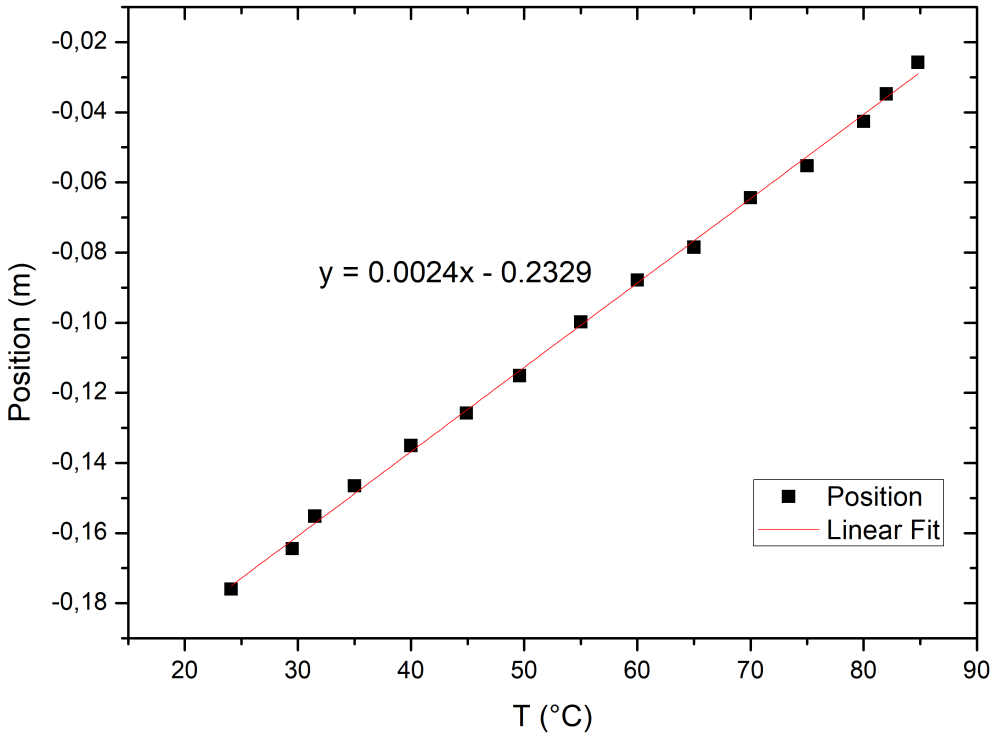

Figure 5.29: Position of the laser spot reflected by the coated silicon slab in function of temperature.

Chapter 6

Finite element analysis using COMSOL Multiphysics®

"La sapienza è figliola della sperienzia."

Leonardo da Vinci
Codice Forster III

Finite Element Analysis (FEA) consists of a simulation of a physical phenomenon by numerically solving differential equations arising in engineering and mathematical modeling. To solve a problem, the FEA subdivides a large system into smaller, simpler parts that are called finite elements. Simple equations that model these finite elements are then assembled into a larger system of equations that models the entire problem. COMSOL Multiphysics® is one of the most commonly used FEA software.

6.1 FEA simulations for the identification of resonance frequencies

For our purpose FEA are used to solve structural analysis problems, in particular to identify and recognize resonant modes of a sample, an information that is particularly useful during loss angle measurements. Using COMSOL it is possible to draw the geometry of a sample, to impose a constraint in the centre (where it is suspended), to specify a material (for example fused silica), to subdivide the sample in elements (implemented by the construction of a *mesh* of the object) and finally to solve differential equations associated with the structural analysis. As a result, values and shapes of sample resonant modes are simulated as represented in Figure 4.2.

6.2 FEA simulations of substrates not completely covered by a coating at Caltech

To evaluate the film loss angle from ringdown measurements performed with GeNS, it is useful to perform a finite element simulation. First of all, loss angles and resonant frequencies of the bare substrate are measured from ringdown experiments, then the sample is covered with a coating and measured again. In particular, frequency shifts before and after the coating deposition are evaluated and fitted in order to extract the Young's modulus (Y) and Poisson ratio (ν) of the film [46], [78], [79]. A COMSOL simulation could help to evaluate those parameters, but it must be able to reproduce frequency shifts between the uncoated and coated substrate with a precision below 1 Hz at 20 kHz. In a FEA a set of continuous partial differential equation are solved numerically. To do that, the space is discretised using tetrahedral or similar cells, that all together form the *mesh*. It is already known that the precision of COMSOL simulations could vary using different meshes [80]. So, first of all it is important to understand if and how the choice of the mesh could have an impact on the prediction of resonant frequencies, on frequency shifts and on the evaluation of dilution factors. Moreover, some laboratories are able to produce coatings on the whole substrate surface with uniform thickness; other facilities can deposit the film only in the internal part of the substrate, leaving an uncoated external ring about 0.5 - 1 mm in size (due to technical issues). The presence of this uncoated part could have an impact on frequency shifts and so on the evaluation of the Young's modulus, Poisson's ratio and also on the value of dilution factors. The following work was carried out during my stay in Pasadena at Caltech under the RISE-NEWS project. One goal was to evaluate the impact of the uncoated edge on frequency shifts and on dilution factors; another goal was to see if, knowing the size of the uncoated edge, it was possible to reproduce frequency shifts and dilution factors. In the following sections results of some COMSOL simulations are presented. In each paragraph a different configuration (geometry) is used for the substrate and the coating, starting from the simplest and ideal case of a substrate completely covered by a thin film. First of all, it was necessary to verify that the choice of a mesh has not a significant impact on frequency shifts for the simplest case (section 6.2.1) then a different configuration with an edge is considered (sections 6.2.2, 6.2.3). At the end, some simulations are performed varying the size of the uncoated edge and its impact on frequency shifts and dilution factors are analysed (sections 6.2.4, 6.2.5).

6.2.1 First configuration: cylindrical substrate completely covered by a coating

The first configuration consists of a silica substrate completely covered by a tantala coating as represented in Figure 6.1. Geometrical parameters and material parameters are listed in Table 6.1 and 6.2.

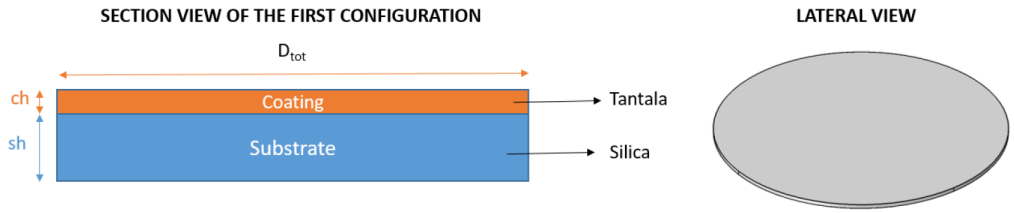

Figure 6.1: Geometry of the first configuration. D_{tot} represents the disk diameter, *ch* and *sh* indicate the coating and substrate heights respectively.

Variable	Value	Description
D_{tot}	75 mm	Diameter
sh	1 mm	Substrate thickness
ch	500 nm	Coating thickness
mesh_size	1/1.5/2/3 mm	Maximum element size
mesh_n_coating	3	Number of layers in the coating
mesh_n_substrate	5	Number of layers in the substrate

Table 6.1: Model parameters for the first configuration.

	Silica	Tantala
Density (ρ) $[Kg/m^3]$	2220	6700
Poisson Ratio (ν)	0.164	0.2
Young's Modulus (E) $[GPa]$	73.2	120

Table 6.2: Material parameters.

The mesh of the bare substrate is built using the following procedure:

- A face (boundary) of the disk is chosen and subdivided using a free triangular mesh. The *mesh_size* parameter sets the maximum element size of this planar mesh.

- The triangular mesh is swept through the substrate. The *mesh_n_substrate* parameter sets the number of layers created inside the substrate.

An example of a mesh of this kind is reported in Figure 6.2: the surface is meshed with triangles and five layers are noticeable.

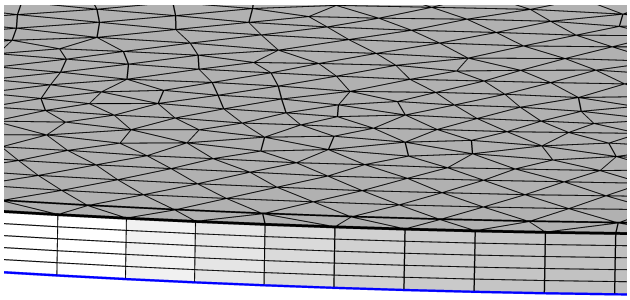

Figure 6.2: Lateral view of the substrate with five layers of triangular mesh.

First of all it is possible to evaluate the dependence of resonance frequencies on the mesh size choice. For this purpose, simulation of the resonance frequencies of the substrate (without the coating) are repeated changing only the *mesh_size* parameter. The result is shown in Figure 6.3.

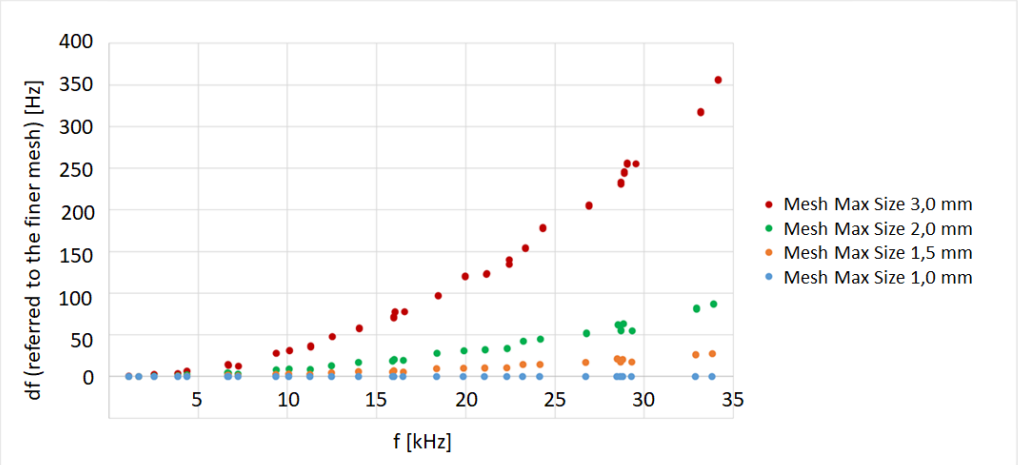

Figure 6.3: Resonant frequencies of the bare substrate for various mesh sizes. The plot shows the difference between mode frequencies for a given mesh size taking those of the finest mesh as a reference (blue dots).

It is clear that the choice of the maximum element size of the mesh has an impact on the evaluation of substrate resonance frequencies. This result was

also observed in [80]. The choice of the number of layers inside the substrate produces smaller variations and it's not considered here [80].

The mesh of the coated substrate is built using the following procedure:

- The same procedure used for the bare substrate is repeated
- The same triangular mesh is then swept through the coating, using another number of layers determined by the *mesh_n_coating* parameter.

An important result is that frequency shifts between the coated and uncoated substrate are not significantly affected by the mesh size choice. The effect is so small that it is better to compare frequency shifts for each mesh size to frequency shifts of the finest mesh as reported in Figure 6.4.

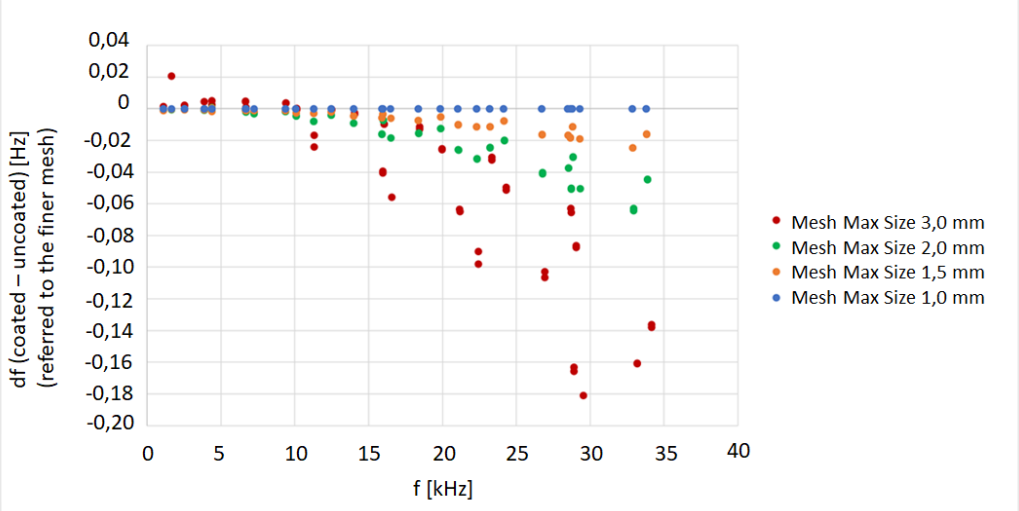

Figure 6.4: Frequency shifts between the coated and uncoated substrate for various mesh sizes. The plot shows the difference between frequency shifts for a given mesh size taking those of the finest mesh as a reference (blue dots).

It is possible to conclude that, for this configuration, absolute values of mode frequencies are affected by the mesh size choice (differences in Figure 6.4 up to hundreds of hertz), but frequency shifts are not significantly changed: differences in Figure 6.4 are always under 0.2 Hz. The conclusion is that COMSOL can evaluate frequency shifts with enough accuracy only if we use exactly the same mesh for the substrate and the coating.

6.2.2 Second configuration: substrate with an external edge completely covered by a coating

The next step is the introduction of an edge in the substrate geometry. First of all, it is necessary to make a comparison with the previous case, so a substrate (with an edge) that is completely covered by a coating is designed. This second configuration is physically identical to the first one (Section 6.2.1), but the geometry implementation in COMSOL is a bit different. A comparison between the two types of geometries used in sections 6.2.1 and 6.2.2 is reported in Figure 6.5.

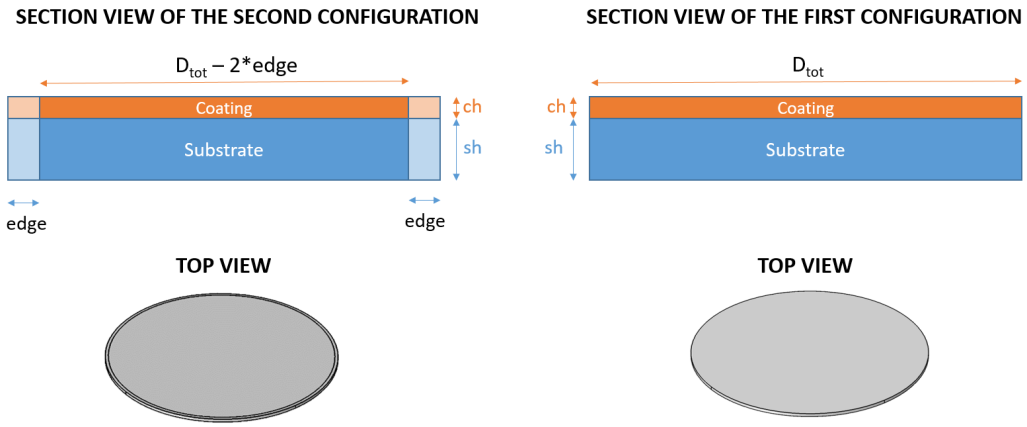

Figure 6.5: Comparison between the second and the first configurations. In both cases the silica substrate is completely covered by a tantala coating.

The purpose of this section is to verify if a variation of the starting geometry can affect the evaluation of frequency shifts or if we obtain the same results. Then, in the next section, the coating will be removed from the external ring. A triangular mesh with a maximum element size of 1 mm is used on both regions (in the inner part and in the external ring) and the mesh is swept through the substrate and the coating. The resulting mesh is shown in Figure 6.6.

Frequency shifts (df) simulated using the new geometry are very similar to the one obtained with the previous geometry. For clarity, it is possible to compare frequency shifts obtained from the second configuration taking the first one as a reference, as reported in Figure 6.7.

It is possible to conclude that frequency shifts of the first and second configurations are almost identical (within an error of 0.0015 Hz).

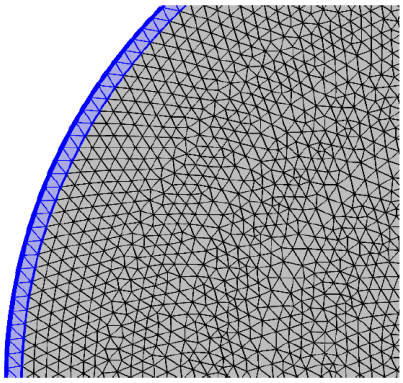

Figure 6.6: A triangular mesh is used in the inner part of the disk and in the external ring.

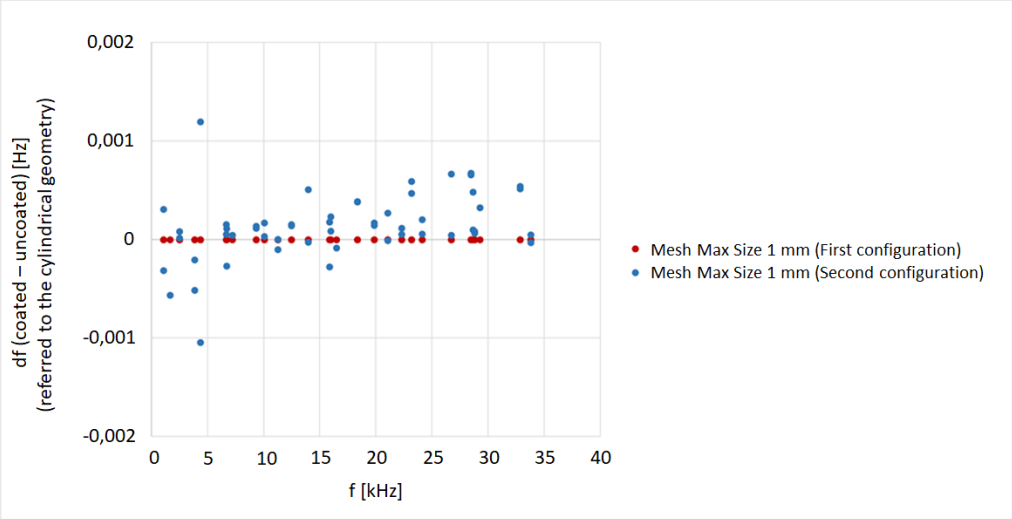

Figure 6.7: Frequency shifts between the coated and uncoated substrate for the two configurations. The plot shows the difference between frequency shifts for the second configuration (blue dots) taking those of the first configuration as a reference (red dots).

6.2.3 Third configuration: substrate with an external edge not completely covered by a coating

In the third configuration the coating is removed from the external part of the substrate as represented in Figure 6.8. Now there is an inner coated region and an external uncoated ring. A lot of measured samples have this kind of geometry due to technical deposition issues.

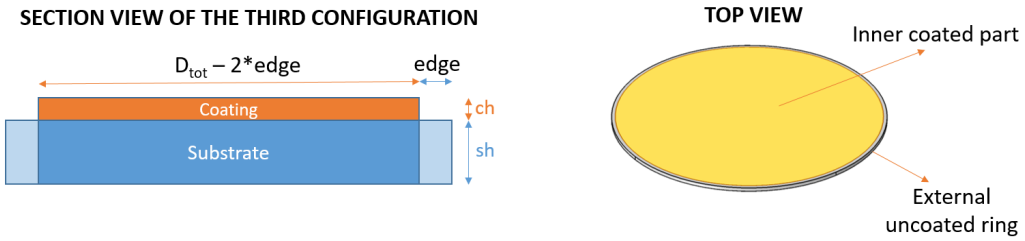

Figure 6.8: Geometry of the third configuration. A silica substrate with a tantala coating in the inner circular region and an uncoated external ring.

Parameters used for the third geometry are reported in Table 6.3.

Variable	Value	Description
D_{tot}	75 mm	Diameter
sh	1 mm	Substrate thickness
ch	500 nm	Coating thickness
edge	1 mm	Size of the uncoated external ring
mesh_size_in	1/1.5/2/3 mm	Max element size in the inner part
mesh_size_ext	0.5/1 mm	Max element size in the external ring
mesh_n_coating	3	Number of layers in the coating
mesh_n_substrate	5	Number of layers in the substrate

Table 6.3: Model parameters for the third configuration

It is possible to use different meshes in the internal (covered) part and in the external ring. However, it is important that the mesh in the inner region of the substrate is identical to the mesh of the coating to have a proper evaluation of frequency shifts (as reported in section 6.2.1). First of all, we have to verify that frequency shifts are not affected by the mesh choice in the internal region, using the same mesh in the outer ring, keeping the *mesh_size_ext* parameter constant and varying the *mesh_size_in* parameter.

In Figure 6.9 it is possible to see that the mesh size choice in the inner

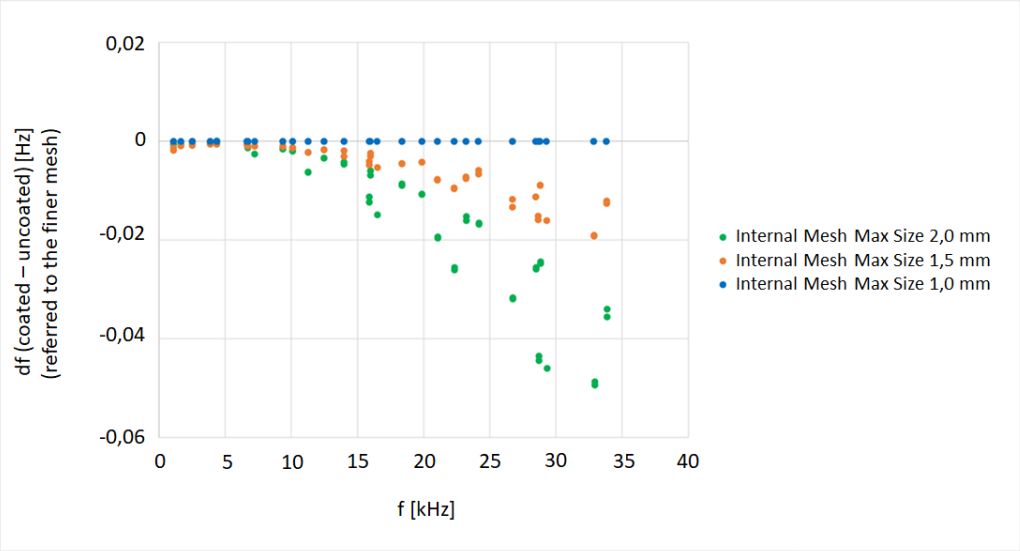

Figure 6.9: Frequency shifts between the coated and uncoated substrate changing the mesh size in the inner region. The plot shows the difference between frequency shifts for a given mesh size taking those of the finest mesh as a reference (blue dots).

region has a small impact on the evaluation of frequency shifts (always less than 0.05 Hz).

Then it is possible to check if variations of meshes in the external ring have an impact on frequency shifts (using the same mesh in the inner coated region). Moreover, it is also possible to change the shape of mesh elements (triangular, quadrangular, mapped) as well as the size as shown in Figure 6.10.

A comparison between frequency shifts obtained with meshes of different sizes and shapes is reported in Figure 6.11.

There seems to be no significant differences between frequency shifts obtained using different meshes in the outer uncoated ring. The *mapped mesh* is probably the best one to use for this kind of geometry, because in the next section the uncoated ring size will be varied and it is better to fix a number of rings in the mapped mesh instead of the maximum element size of a triangular mesh.

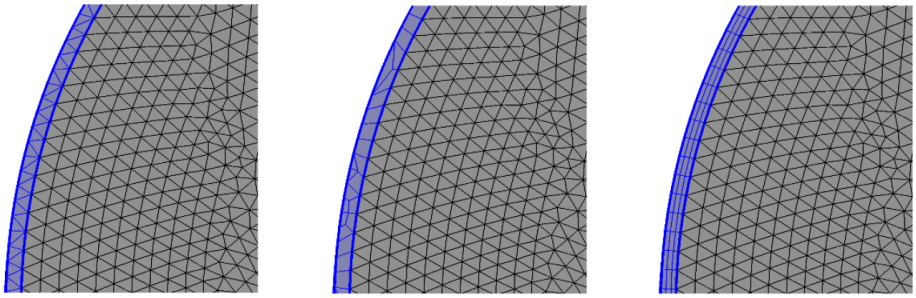

Figure 6.10: Comparison between different meshes in the outer ring: a triangular mesh on the left, a quadrangular mesh in the centre and a mapped mesh on the right.

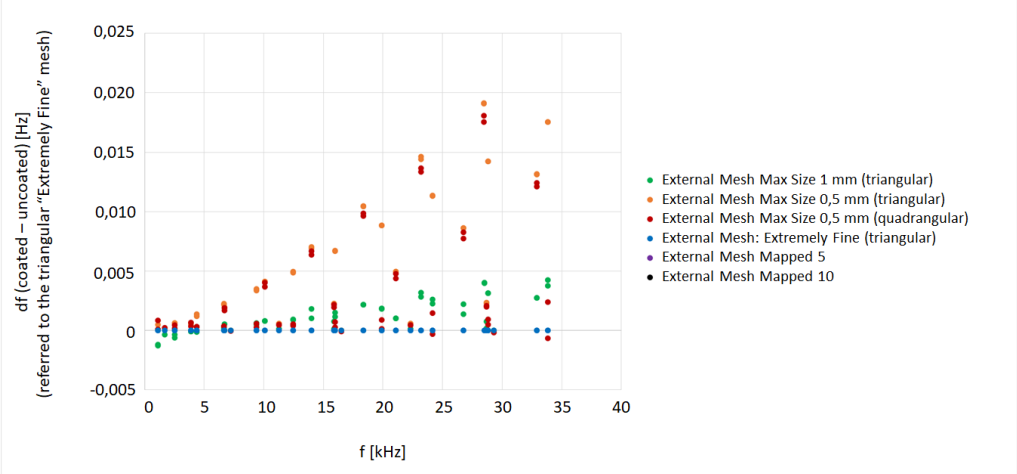

Figure 6.11: Frequency shifts between the coated and uncoated substrate changing the mesh size and shape in the external ring. The plot shows the difference between frequency shifts for a given mesh taking those of the finest mesh as a reference (blue dots).

6.2.4 Simulations varying the size of the uncoated ring

From simulations reported in previous sections it is possible to conclude that neither the mesh size in the internal coated region, neither the mesh size or type in the external uncoated part can produce a significant variation of frequency shifts. From now on, the mesh type is fixed and COMSOL simulations are repeated varying the *edge* parameter from 0 mm (a completely covered substrate) to 1 mm (that is a maximum reasonable value of the uncoated region) with steps of 0.1 mm. A mapped mesh in the external ring is used. Model parameters used for simulations in this section are reported in Table 6.4.

Variable	Value	Description
D_{tot}	75 mm	Diameter
sh	1 mm	Substrate thickness
ch	500 nm	Coating thickness
mesh_size_in	1 mm	Max element size in the inner part
mesh_n_mapped	3	Number of rings in the mapped mesh
mesh_n_coating	3	Number of layers in the coating
mesh_n_substrate	5	Number of layers in the substrate
edge	1.0/.../0.0 mm	Width of the uncoated external ring

Table 6.4: Model parameters, varying the uncoated edge width from 1.0 mm to 0.0 mm with steps of 0.1 mm

When a coating is deposited on a substrate there is always a frequency shift of its resonant modes. The presence of un uncoated external ring will produce an additional shift. Simulation results are reported in Figure 6.12: frequency shifts corresponding to each *edge* parameter are referred to the ideal case of a completely covered substrate (corresponding to *edge* = 0 mm). It is possible to note that there are two branches for each *edge* value: the first one corresponds to *butterfly modes*, the second one corresponds to other resonant modes (*mixed modes* and modes that are not measurable with GeNS). This effect is emphasized in Figure 6.13, where only two *edge* values are shown (1 mm and 0 mm) and different resonant mode families are represented with various symbols.

It is also useful to make a comparison between frequency shifts of the same resonant mode with different edge values. Figure 6.14 shows the behaviour of two mixed modes (1;2) and (2;2): in both cases frequency shifts are increasing with the *edge* parameter. Figure 6.15 shows the behaviour of four butterfly modes: here frequency shifts have a different behaviour vary-

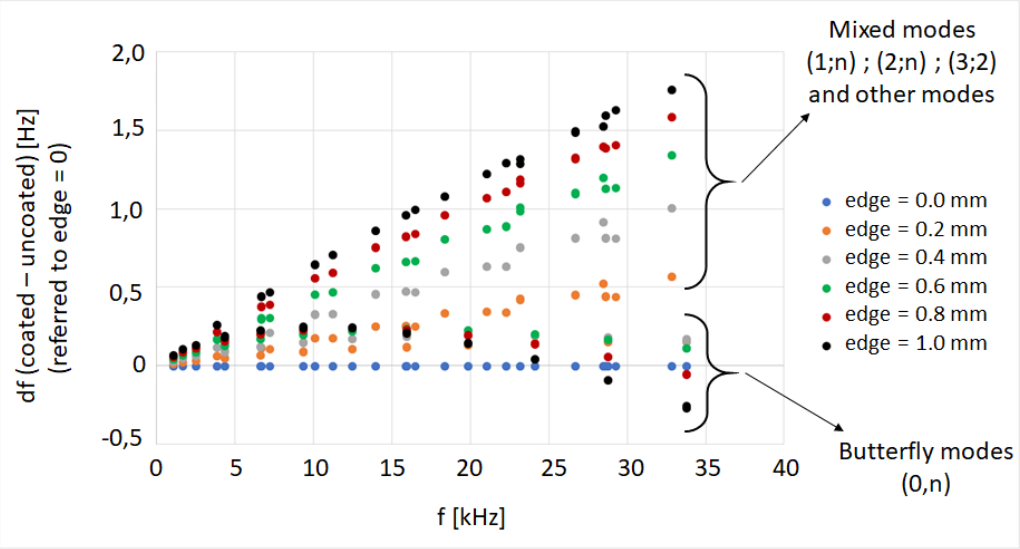

Figure 6.12: Frequency shifts between the coated and uncoated substrate changing the *edge* parameter. The plot shows the difference between frequency shifts for a certain *edge* value taking those of the completely covered substrate as a reference (*edge* = 0 mm). There are two branches, linked to different resonant modes, reported on the right.

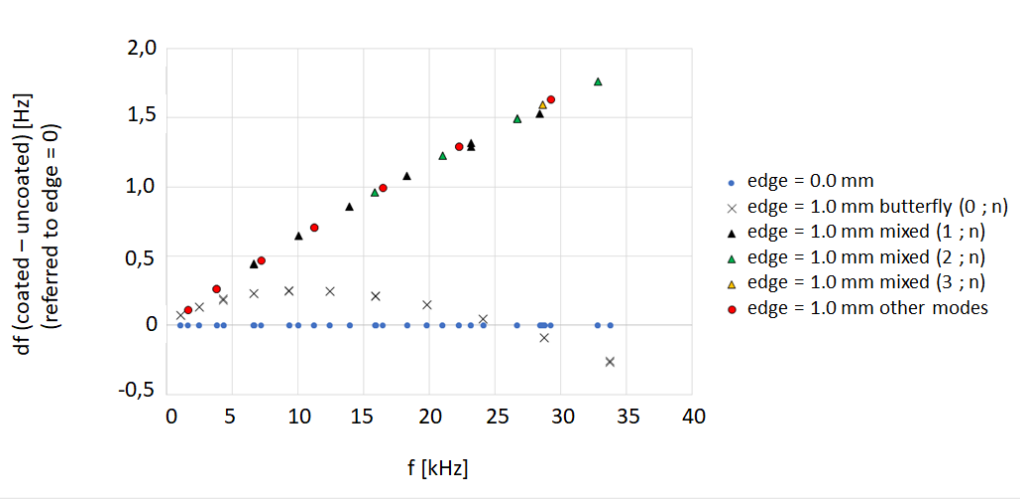

Figure 6.13: Frequency shifts between the coated and uncoated substrate for two edge parameters. The plot shows the difference between frequency shifts for an edge of 1 mm taking those with an edge of 0 mm as a reference (blue dots). Different symbols represent various resonant modes.

ing the *edge* parameter. In the second row of Figure 6.15 the frequency shift value corresponding to an edge of 0.4 mm seems not to follow the trend of others frequency shifts. This could be due to a small error in the COMSOL simulation and not linked to a physical effect.

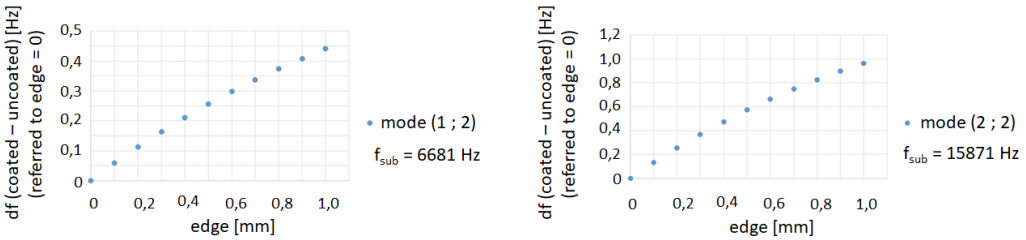

Figure 6.14: Frequency shifts between the coated and uncoated substrate changing the *edge* parameter. The plot shows the difference between a frequency shift for a certain mode referred to the ideal case of *edge* = 0 mm. In this figure two *mixed modes* are represented.

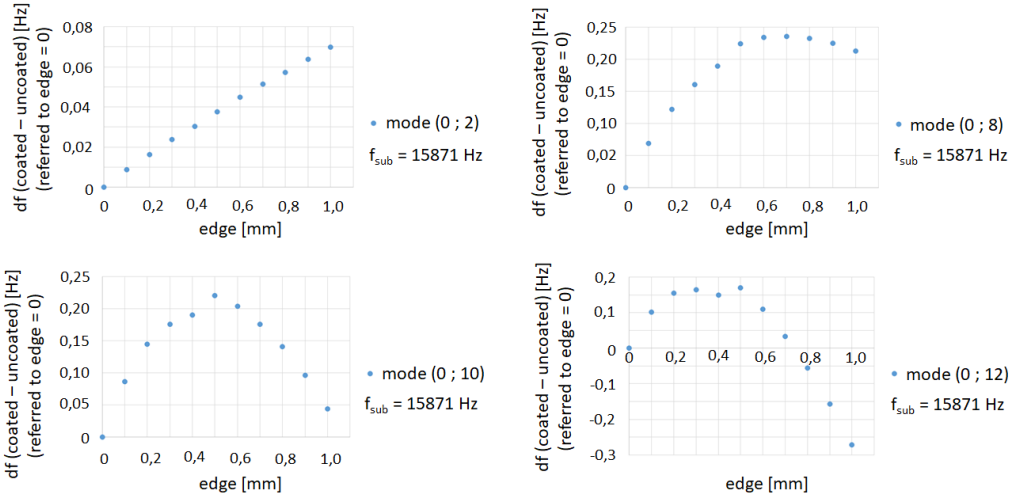

Figure 6.15: Frequency shifts between the coated and uncoated substrate changing the *edge* parameter. The plot shows the difference between a frequency shift for a certain mode referred to the case of *edge* = 0 mm. In this figure four *butterfly modes* are represented.

It seems that if the resonant mode has a substantial oscillation amplitude in the inner part of the disk (like *mixed modes*), frequency shifts increase as the size of the uncoated edge, compared to the configuration without

edge (Figure 6.14). In this case, the absence of coating in the external ring produces an effect similar to a coating on the whole substrate surface with lower density (Figure 6.16). The standard density for tantala is 6700 kg/m^3. The value for the lower density configuration is set equal to 6338 kg/m^3 (5.4% lower, that is the volume variation between a coating deposited on the whole substrate and a coating deposited leaving and edge on 1 mm).

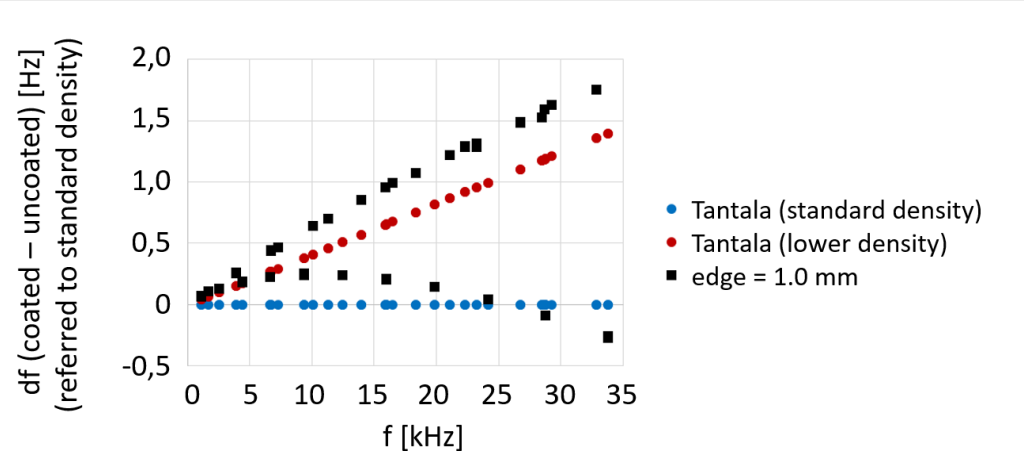

Figure 6.16: Frequency shifts between the coated and uncoated substrate changing the coating density. The plot shows the difference between frequency shifts for a lower density coating (red dots) referred to the same mode for a standard tantala coating (blue dots) and compared to frequency shifts of a sample with an edge of 1 mm (black dots).

It seems that if the resonant mode has a substantial oscillation amplitude on the edge of the disk (like *butterfly modes* with a lot of longitudinal nodes), the frequency shifts have a different behaviour: a sum of the previous effect (less coating mass) and another negative contribution that becomes predominant when the *edge* parameter is increasing. If there is no coating at all, frequency shifts must be zero; so if most of the oscillations occur on the uncoated ring, frequency shifts should be lower than a completely covered substrate. It is possible to simulate the negative contribution comparing two samples with the same edge (1 mm): the first has a tantala coating of standard density; the second has a tantala coating with 5.4% higher density. Results are shown in Figure 6.17.

The sum of the two contributions is shown in Figure 6.18. This is not so similar to the behaviour predicted in Figure 6.13. Maybe there are other physical mechanisms involved that are not included in these two simulations.

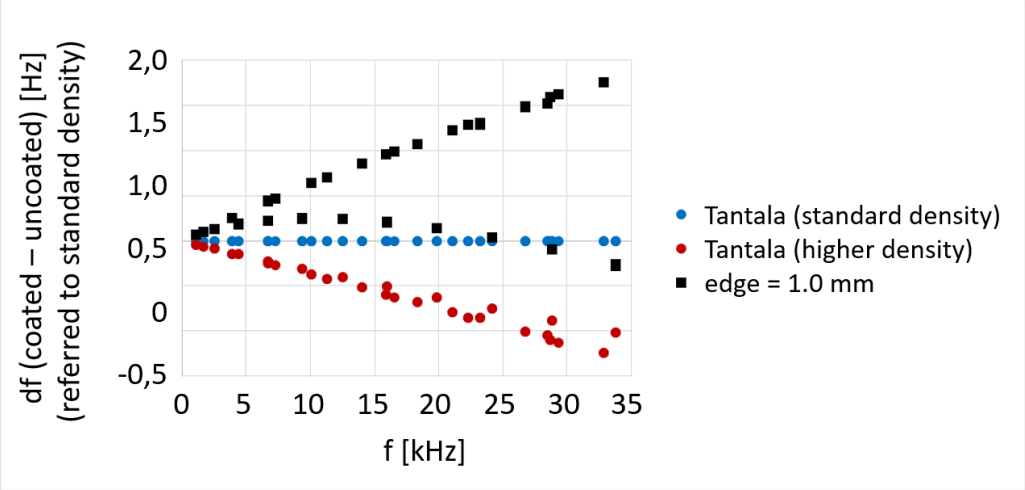

Figure 6.17: Frequency shifts between the coated and uncoated substrate changing the coating density. The plot shows the difference between frequency shifts for a higher density coating (red dots) referred to the same mode for a standard tantala coating (blue dots) and compared to frequency shifts of a disk with an edge of 1 mm (black dots).

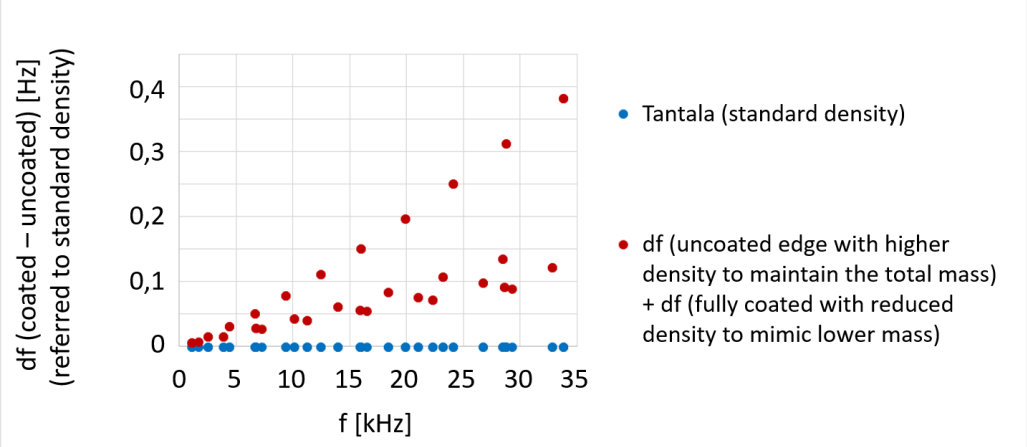

Figure 6.18: Sum of frequency shifts due to a sample with an uncoated edge with higher tantala density and a fully coated sample with lower tantala density. These two contributions are shown separately in the previous two figures.

6.2.5 Dilution Factor variations

As reported in section 6.2.4, variations of the size of the uncoated ring produce small changes in frequency shifts (always under 2 Hz at 30 kHz). It is useful to check which is the impact of these variations on dilution factors. The total dilution factor could be divided in two components: bulk and shear [79]. Figure 6.19 shows the simulated dilution factors (total, bulk and shear) for some values of the *edge* parameter. There are substantial variations of dilution factors as the *edge* parameter varies from 0 to 1 mm.

Figure 6.20 shows the relative variation of simulated dilution factors (total, bulk and shear), taking the complete coated configuration as a reference.

Figure 6.19 and Figure 6.20 show two branches in dilution factors: one resonant family mode is quite constant varying the edge parameter, while the other shows bigger variations. It is useful to make a comparison between dilution factors of the same resonant mode with different *edge* values. Figure 6.21 shows two mixed modes (1;2) and (2;2): in both cases the dilution factor is quite constant with the amplitude of the edge parameter. This is due to the fact that mixed modes have a substantial oscillation amplitude in the coated part of the disk, so the coating energy (directly linked to the dilution factor) is almost unaltered.

Figure 6.22 shows the behaviour of two butterfly modes (0;8) and (0;12): in both cases the dilution factor is decreasing with the amplitude of the edge parameter. This is due to the fact that butterfly modes have a substantial oscillation amplitude in the external part of the disk, so the coating energy (directly linked to the dilution factor) decreases with the *edge* parameter.

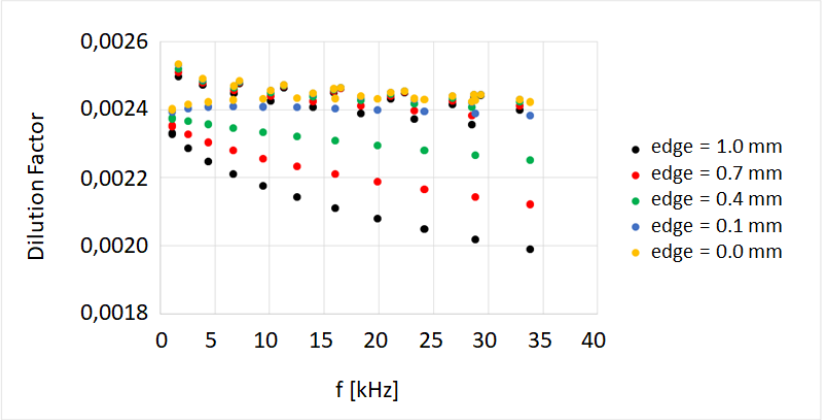

(a) *dilution factor (total)*

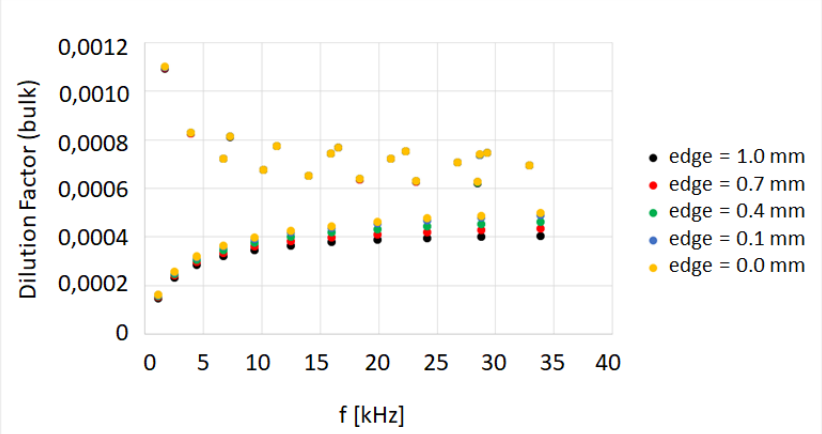

(b) *dilution factor (bulk)*

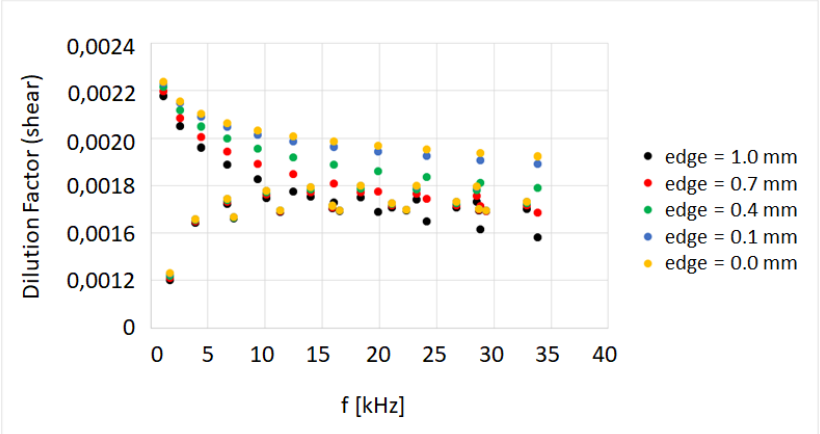

(c) *dilution factor (shear)*

Figure 6.19: Effect of *edge* parameter variation on the simulated dilution factors (total, bulk, shear).

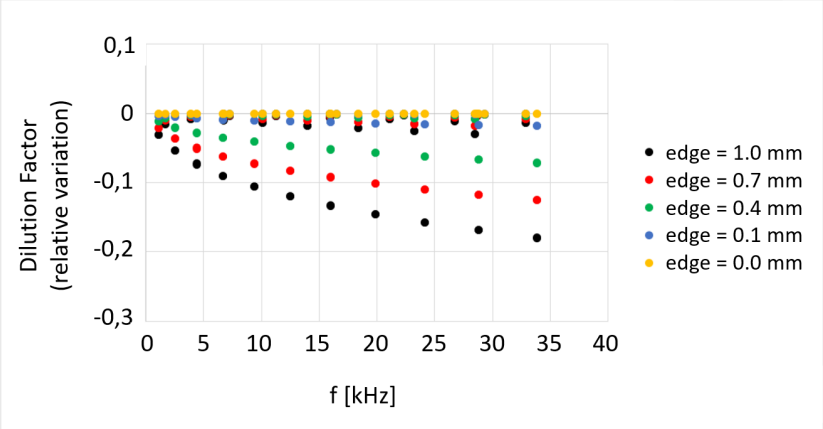

(a) *dilution factor (total)*

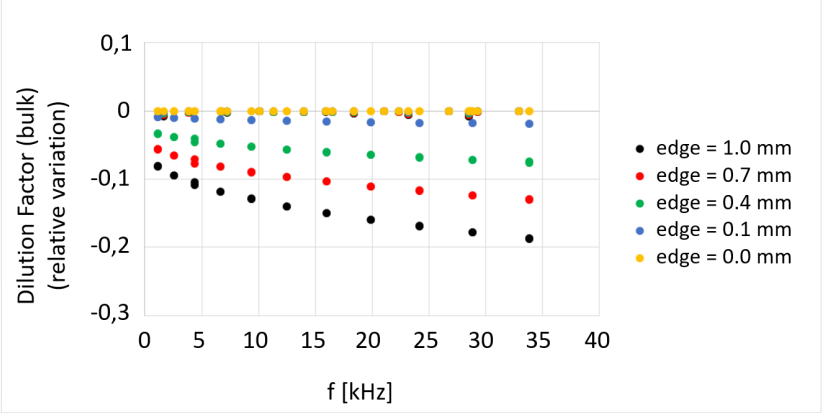

(b) *dilution factor (bulk)*

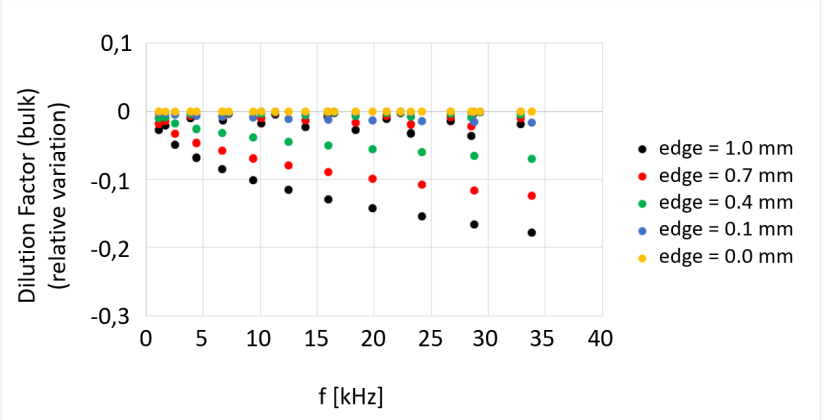

(c) *dilution factor (shear)*

Figure 6.20: Effect of *edge* parameter variation on the simulated dilution factors (total, bulk, shear). Relative variations (referred to the completed coated configuration) are reported.

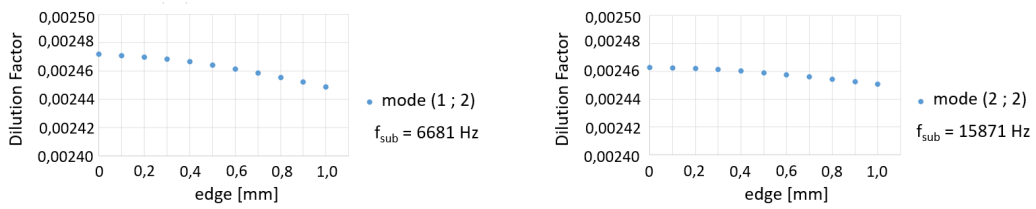

(a) *dilution factor (total)*

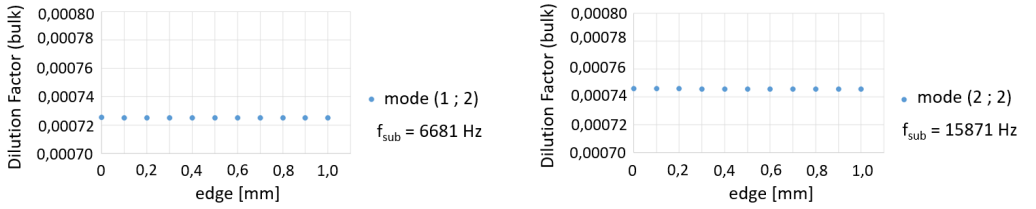

(b) *dilution factor (bulk)*

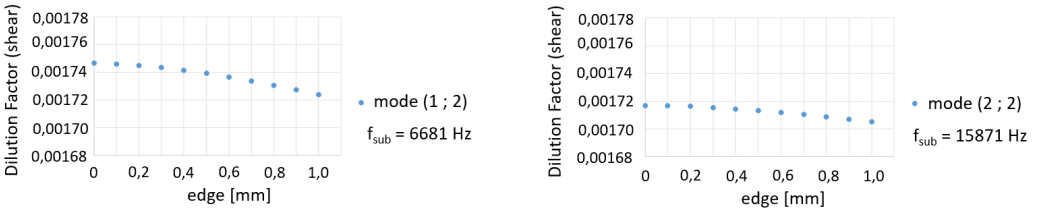

(c) *dilution factor (shear)*

Figure 6.21: Dilution factors dependence (total, bulk, shear) on the *edge* parameter for two mixed modes.

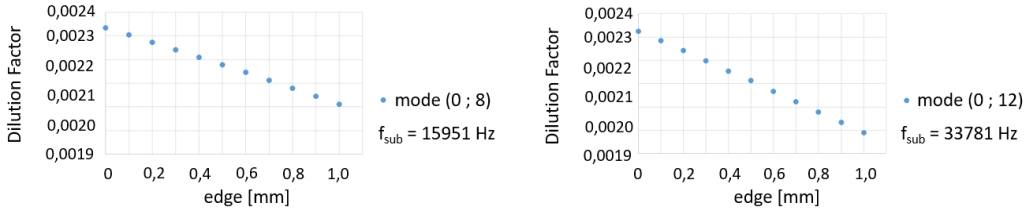

(a) *dilution factor (total)*

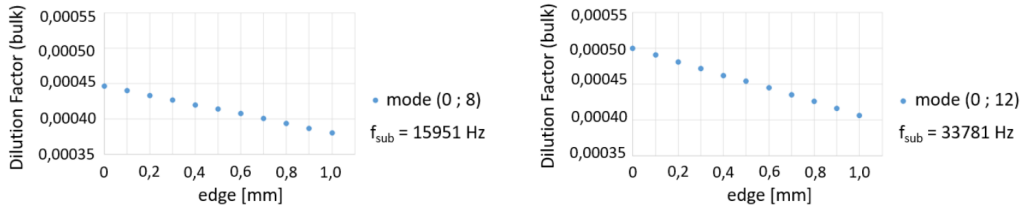

(b) *dilution factor (bulk)*

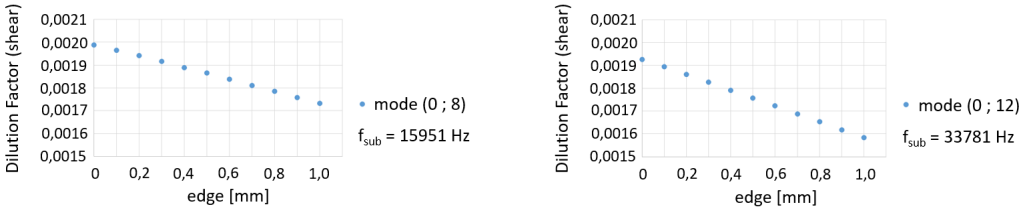

(c) *dilution factor (shear)*

Figure 6.22: Dilution factor dependence (total, bulk, shear) on the *edge* parameter for two butterfly modes.

6.2.6 MATLAB® simulation and Python™ fit

COMSOL simulations are then exported to a MATLAB® script which generates random values for some coating parameters (Young's modulus, Poisson Ratio, thickness, density and edge amplitude) within a reasonable range and use them to run COMSOL simulations. In particular, each set of coating parameters is used for two simulations: one for the bare substrate and another one for the coated substrate. In this way, after hundreds of simulations automatically generated, it is possible to have a great number of frequency shift values associated with each set of five randomly generated parameters. Finally, a Python™ code reads the results of previous simulations and performs a polynomial fit with five input variables. In this way, it is possible to associate an experimentally measured frequency shift with a set of five coating parameters. Up to now, this process was carried out with four parameters, without taking the *edge* parameter into account.

6.2.7 Summary and conclusions on simulation results

From the results presented in section 6.2.1 it is possible to conclude that absolute values of mode frequencies are affected by the mesh size choice, but frequency shifts are not significantly changed if the same mesh is used for the bare substrate and for the coated substrate. Moreover, from section 6.2.2, it is possible to conclude that changing the initial geometry from a uniform cylinder to a cylinder with an external edge has no impact on the evaluation of frequency shifts when the coating is still covering the entire surface: having an edge in the geometry only affects the mesh. From what explained in section 6.2.3 it is clear that variations of shape and dimension of the mesh in the internal and external part of the cylinder produce negligible variations in frequency shifts and so it is possible to conclude that COMSOL has enough accuracy to simulate the effect of an uncoated edge, provided that the same mesh is used for coated and uncoated substrates. In section 6.2.4 COMSOL simulations are repeated varying the amplitude of the uncoated edge from 0 to 1 mm with steps of 0.1 mm. Frequency shifts can vary up to 2 Hz (at 35 kHz) with respect to frequency shifts calculated in the completed coated case. Those variations show two different trends: one for mixed modes (1;n), (2;n), etc... a linear trend with positive slope; another one for butterfly modes (0;n) following a curved behaviour. Up to now we have a qualitative explanation for these behaviours, based on the shape and amplitude of oscillations in the uncoated edge for each family mode, but quantitative simulations could not reproduce the two trends with a good accuracy. The main idea is that if most of the motion is situated in the uncoated ring (that is the

case of butterfly modes at high frequencies) frequency shifts should tend to zero as the *edge* parameter increases. In section 6.2.5 COMSOL simulations are used in order to evaluate variations of dilution factors (total, bulk, shear) changing the uncoated edge amplitude from 0 mm to 1 mm. The result is that dilution factors can vary up to 20% respect to dilution factors calculated in the completed coated case. Those variations are divided in two main branches: the one associated to mixed modes shows values very similar to the completed coated case (differences are lower than 3% for each frequency and edge amplitude); the other one associated to butterfly modes shows bigger variations compared to the completed coated case (differences are up to 20% at 35 kHz). These two behaviours are linked to the shape and the amplitude of oscillations in the uncoated edge for each family mode. If most of the motion is situated in the uncoated ring (that is the case for butterfly modes at high frequencies) variations on the energy ratio (energy of the coating divided by the total energy) are bigger. This effect seems not linked to the fact that there is less coating material, because mixed modes are constant and only butterfly modes are affected. A last important issue that will be checked in the future is to quantify the impact on the estimated coating parameters (Young's modulus, Poisson's ratio, dilution factors and loss angle of the coating) taking the *edge* parameter into account. Experimentally the coating loss angle is estimated as follows:

1. Frequency shifts and Q values are measured by ringdown experiments (measuring the substrate before and after the coating deposition).

2. Frequency shifts are fitted to Y and ν, assuming known values for the density and thickness and ignoring the uncoated edge ($edge = 0$).

3. Dilution factors (total, bulk and shear) are computed using estimated values for Y and ν.

4. Computed dilution factors are used to extract coating loss angles (total, bulk and shear)

The main question is how much the final result can change by considering a wrong value of the *edge* parameter (or not considering it at all). It is possible to compare results obtained from an experimental set of frequency shifts using a certain value of the edge amplitude (that is directly measurable on the sample surface) and results obtained from the same set of frequency shifts using the model for a completely coated substrate and we can evaluate the differences in Y, ν and dilution factors. Files used for this note (COMSOL simulations, graphs, MATLAB and Python codes) are deposited on *GitLab* [81].

Conclusions

"What we know is a drop,
what we don't know is an ocean."

Isaac Newton

During my PhD studies a lot of experimental facilities have been built and tested in the Urbino physics laboratory. One GeNS facility has been assembled during the first year, using an already existing vacuum chamber and progressively updated over time to work with cryogenic liquids. The oven has been updated to perform thermal treatments in different conditions (in air, in vacuum and in a controlled atmosphere). Another GeNS facility has been designed, build and tested during the second year, in order to improve the quality of measurements and make them faster. Two facilities for the measurement of the coating thermo-optic parameters and sample curvature have been developed and tested during the last year, after the pause forced by the lockdown. Moreover, at the end of 2021, a clean room has been designed and installed inside our laboratory in order to minimize dust contamination during experiments. The facilities mentioned above allowed me to perform measurements within some of the research lines of the VCR&D project:

- **Mechanical loss metrology.** It covers several topics of interest to all laboratories performing loss angle measurements. The measurement repeatability (tested suspending the same sample multiple times) results to be in the range of 10% for bare substrates and 5% for coated disks. A new campaign of measurements will be performed inside the new clean room, where an improvement in repeatability is expected.

  A study of the experimental evaluation of the dilution factor was carried on, finding very stringent conditions on both mass and resonant frequency measurements. In particular, resonant frequencies are very sensitive to temperature variations. This effect can be corrected *a posteriori* measuring the temperature on a twin sample installed inside

the vacuum chamber. The frequency correction can be evaluated using a simple equation, but depends on a parameter that I've measured for a silica substrate.

Moreover, I've tested different annealing procedures in order to find out what the best temperature and duration are, producing substrates with stable frequencies over time and with the least possible curvature effects. The best thermal treatment results to be at 1000°C for 20 hours. However, frequency shifts that arise after the first treatment seem to be very sensitive to the annealing temperature and to be linked to variations of the Young's modulus and Poisson ratio, according to FEA simulations. Further research is needed to understand the origin of frequency shifts associated with each annealing temperature.

- **Fluoride coatings.** MgF_2 and AlF_3 were characterized in our laboratory from a mechanical point of view. The evolution of their losses as a function of thermal treatment temperatures and durations was studied. The result is that both coating materials reach a minimum in their mechanical losses after a thermal treatment of 10 hours at 285°C. However, their losses at room temperature are still too high compared to those of silica coatings. The optimization of the coating growth parameters and loss angle measurements at low temperature will be object of future studies.

- **Cryogenic loss angle measurements.** A preliminary measurement of a silicon disk was performed using liquid nitrogen. As expected, the loss angle shows a minimum near 120 K. This result confirms that our cryogenic GeNS is working properly, but needs some improvements in order to ensure a better sample stability on the hemisphere and to reach lower temperatures ($\sim$ 2 K) using liquid helium. This kind of measurements will be carried out in the future and will be of crucial importance in identifying new coating materials for the next generation of cryogenic GWDs.

- **Thermo-optic parameters evaluation.** A linear combination of thermal expansion and thermo-refractive coefficients (α and β) of different coating materials was measured. First of all, we have tested our facility using a tantala sample already measured by Gretarsson at the Embry-Riddle Aeronautical University. Our results are in good agreement, so we decided to characterized also a silica sample and a silicon nitride coating, that is a promising material for the next generation of mirrors. The knowledge of coating thermo-optic parameters is useful

to estimate the amount of thermo-optic noise that can arise from that kind of materials. Moreover, we find out that performing this measurements in reflection (instead of in transmission) can improve the acquired spectrum quality and hence the parameter evaluation.

Moreover, at the end of 2019, I spent a period of time in the United States. During my short stay in Prescott (Arizona) I have learned a lot about the thermo-optic noise and experimental issues linked to its evaluation. During my stay at Caltech (California) I learned to perform FEA simulations to predict the behaviour of coating materials. In particular, FEA simulations were used to understand the impact of coatings that are not deposited on the whole substrate on frequency shifts and dilution factors. The result is that frequency shifts are not significantly affected by the presence of an uncoated external edge (only 2 Hz at 35 kHz) but, on the other hand, dilution factors can vary up to 20%. This effect has a considerable impact on the evaluation of coating loss angles and mechanical properties and should be taken into account for future measurements.

Appendix A

Acronyms

AdV Advanced Virgo.

AFM Atomic Force Microscopy.

aLIGO Advanced LIGO.

A.U. Arbitrary Units.

BBH Binary Black Holes.

BH Black Hole.

BNS Binary Neutron stars.

CRD Coating Research and Development.

CTN Coating Thermal Noise.

ESEM Environmental Scanning Electron Microscope.

ET Einstein Telescope.

ETM End Test Mirror.

FEA Finite Element Analysis.

GeNS Gentle Nodal Suspension.

GR General Relativity.

GW Gravitational-Wave.

GWDs Gravitational-Wave Detectors.

HR High Reflective.

HV High Voltage.

IBS Ion Beam Sputtering.

ITM Input Test Mirror.

KAGRA Kamioka Gravitational-Wave Detector.

LabVIEW Laboratory Virtual Instrumentation Engineering Workbench.

LIGO Laser Interferometer Gravitational-Wave Observatory.

LMA Laboratoire des Matériaux Avancés.

NS Neutron Star.

RMS Root Mean Square.

SEM Scanning Electron Microscopy.

TLS Two Level System.

VCR&D Virgo Coating Research and Development.

Appendix B

Symbols

Symbol	Name	SI unit
k_b	Boltzmann's constant	J/K
c	Speed of light	m/s
T	Temperature	K
ω	Angular frequency	rad/s
f	Frequency	Hz
C	Heat capacity per volume	J/Km^3
k	Thermal conductivity	W/mK
n	Refractive index	
α	Thermal expansion coefficient	$1/K$
β	Thermo-optic coefficient	
Y	Young's Modulus	N/m^2
σ	Poisson ratio	
ϕ	Loss angle	rad
λ	Wavelength	m
w_m	Laser radius	m
P	Laser power	W
d	Coating thickness	m
m	Mass	Kg
ρ	Density	Kg/m^3
D	Dilution Factor	

Table B.1: Frequently used symbols, physical constants, and their units in the International System (SI) .

Bibliography

[1] A. Einstein. "Die Grundlage der allgemeinen Relativitätstheorie". In: *Annalen der Physik* 354.7 (1916), pp. 769–822. DOI: https://doi.org/10.1002/andp.19163540702.

[2] I. Newton. *Philosophiae Naturalis Principia Mathematica*. Iussu Societatis regiae ac Typis Josephi Streater, Londini, 1687.

[3] John Archibald Wheeler and Kenneth Ford. *Geons, black holes and quantum foam: a life in physics*. 2000.

[4] Joseph H Taylor and Joel M Weisberg. "A new test of general relativity-Gravitational radiation and the binary pulsar PSR 1913+ 16". In: *The Astrophysical Journal* 253 (1982), pp. 908–920.

[5] Joel M Weisberg, David J Nice, and Joseph H Taylor. "Timing measurements of the relativistic binary pulsar PSR B1913+ 16". In: *The Astrophysical Journal* 722.2 (2010), p. 1030.

[6] B. P. Abbott et al. "Observation of Gravitational Waves from a Binary Black Hole Merger". In: *Physical Review Letters* 116.6 (Feb. 2016). ISSN: 1079-7114. DOI: 10.1103/physrevlett.116.061102. URL: http://dx.doi.org/10.1103/PhysRevLett.116.061102.

[7] R Abbott et al. "GWTC-3: Compact binary coalescences observed by LIGO and Virgo during the second part of the third observing run". In: *arXiv preprint arXiv:2111.03606* (2021).

[8] *O1/O2 Catalog*. 2021. URL: https://www.ligo.org/detections/O1O2catalog.php.

[9] Alexandre Le Tiec and Jerome Novak. "Theory of Gravitational Waves". In: (July 2016).

[10] P.R. Saulson. *Fundamentals of Interferometric Gravitational Wave Detectors*. World Scientific, 1994. ISBN: 9789810218201. URL: https://books.google.it/books?id=4JyGQgAACAAJ.

[11] *Gravitational wave spectrum*. 2021. URL: https://lisa.nasa.gov/.

[12] *Sources of Gravitational Waves*. 2021. URL: https://www.ligo.org/science/GW-Sources.php.

[13] Brnard F Schutz. "Gravitational-wave sources". In: *Classical and Quantum Gravity* 13.11A (1996), A219.

[14] L Ju, D G Blair, and C Zhao. "Detection of gravitational waves". In: *Reports on Progress in Physics* 63.9 (Aug. 2000), pp. 1317–1427. DOI: 10.1088/0034-4885/63/9/201. URL: https://doi.org/10.1088/0034-4885/63/9/201.

[15] Matthew Pitkin et al. "Gravitational Wave Detection by Interferometry (Ground and Space)". In: *Living Reviews in Relativity* 14.1 (July 2011). ISSN: 1433-8351. DOI: 10.12942/lrr-2011-5. URL: http://dx.doi.org/10.12942/lrr-2011-5.

[16] Adrian Cho. "Gravitational waves serve up a mystery". In: *Science* 351.6275 (2016), pp. 796–797. ISSN: 0036-8075. DOI: 10.1126/science.351.6275.796. eprint: https://science.sciencemag.org/content/351/6275/796.full.pdf. URL: https://science.sciencemag.org/content/351/6275/796.

[17] Junaid Aasi et al. "Advanced ligo". In: *Classical and quantum gravity* 32.7 (2015), p. 074001.

[18] Fet al Acernese et al. "Advanced Virgo: a second-generation interferometric gravitational wave detector". In: *Classical and Quantum Gravity* 32.2 (2014), p. 024001.

[19] Yoichi Aso et al. "Interferometer design of the KAGRA gravitational wave detector". In: *Physical Review D* 88.4 (2013), p. 043007.

[20] Hartmut Grote, LIGO Scientific Collaboration, et al. "The GEO 600 status". In: *Classical and Quantum Gravity* 27.8 (2010), p. 084003.

[21] *LIGO Caltech website*. 2021. URL: https://www.ligo.caltech.edu/news/ligo20191004.

[22] *Virgo status Web Site*. 2021. URL: https://www.virgo-gw.eu/status.html.

[23] Aaron Buikema et al. "Sensitivity and performance of the Advanced LIGO detectors in the third observing run". In: *Physical Review D* 102.6 (2020), p. 062003.

[24] KAGRA Collaboration. *Advanced LIGO, Advanced Virgo and KAGRA observing run plans*. 2019.

[25] LIGO Scientific Collaboration, Virgo Collaboration, et al. "Multi-messenger observations of a binary neutron star merger". In: (2017).

[26] Bangalore Sathyaprakash et al. "Scientific objectives of Einstein telescope". In: *Classical and Quantum Gravity* 29.12 (2012), p. 124013.

[27] *The ET (Einstein Telescope) project Web Site*. 2021. URL: http://www.et-gw.eu/index.php/etimages.

[28] Benjamin P Abbott et al. "Exploring the sensitivity of next generation gravitational wave detectors". In: *Classical and Quantum Gravity* 34.4 (2017), p. 044001.

[29] *Cosmic Explorer Web Site*. 2021. URL: https://cosmicexplorer.org/.

[30] David Reitze et al. "The US program in ground-based gravitational wave science: contribution from the LIGO Laboratory". In: *arXiv preprint arXiv:1903.04615* (2019).

[31] T Accadia et al. "The seismic Superattenuators of the Virgo gravitational waves interferometer". In: *Journal of low frequency noise, vibration and active control* 30.1 (2011), pp. 63–79.

[32] W A Edelstein et al. "Limits to the measurement of displacement in an interferometric gravitational radiation detector". In: *Journal of Physics E: Scientific Instruments* 11.7 (July 1978), pp. 710–712. DOI: 10.1088/0022-3735/11/7/030. URL: https://doi.org/10.1088/0022-3735/11/7/030.

[33] Richard F Greene and Herbert B Callen. "On a theorem of irreversible thermodynamics. II". In: *Physical Review* 88.6 (1952), p. 1387.

[34] Gregory M Harry et al. "Thermal noise in interferometric gravitational wave detectors due to dielectric optical coatings". In: *Classical and Quantum Gravity* 19.5 (Feb. 2002), pp. 897–917. DOI: 10.1088/0264-9381/19/5/305. URL: https://doi.org/10.1088/0264-9381/19/5/305.

[35] NM Kondratiev, AG Gurkovsky, and ML Gorodetsky. "Thermal noise and coating optimization in multilayer dielectric mirrors". In: *Physical Review D* 84.2 (2011), p. 022001.

[36] VB Braginsky, ML Gorodetsky, and SP Vyatchanin. "Thermo-refractive noise in gravitational wave antennae". In: *Physics Letters A* 271.5-6 (2000), pp. 303–307.

[37] Francesco Piergiovanni et al. "The dynamics of monolithic suspensions for advanced detectors: a 3-segment model". In: *Journal of Physics: Conference Series*. Vol. 228. 1. IOP Publishing. 2010, p. 012017.

[38] Massimo Granata et al. "Amorphous optical coatings of present gravitational-wave interferometers". In: *Classical and Quantum Gravity* 37.9 (2020), p. 095004.

[39] F Travasso and. "Status of the Monolithic Suspensions for Advanced Virgo". In: *Journal of Physics: Conference Series* 957 (Feb. 2018), p. 012012. DOI: 10.1088/1742-6596/957/1/012012. URL: https://doi.org/10.1088/1742-6596/957/1/012012.

[40] Herbert B Callen and Theodore A Welton. "Irreversibility and generalized noise". In: *Physical Review* 83.1 (1951), p. 34.

[41] Peter R Saulson. "Thermal noise in mechanical experiments". In: *Physical Review D* 42.8 (1990), p. 2437.

[42] Arthur S Nowick, Brian Shepherd Berry, and J Lawrence Katz. *Anelastic relaxation in crystalline solids*. Acedemic Press Inc., 1975.

[43] KA Topp and David G Cahill. "Elastic properties of several amorphous solids and disordered crystals below 100 K". In: *Zeitschrift für Physik B Condensed Matter* 101.2 (1996), pp. 235–245.

[44] *The "Q" factor of an oscillating system*. 2021. URL: http://spiff.rit.edu/classes/phys283/lectures/forced_ii/forced_ii.html.

[45] Tianjun Li et al. "Measurements of mechanical thermal noise and energy dissipation in optical dielectric coatings". In: *Physical Review D* 89.9 (2014), p. 092004.

[46] G. Vajente. *Notes on measuring coatings with a nodal suspension*. Tech. rep. LIGO-T1900276. Caltech, 2019.

[47] Erika D'Ambrosio et al. "Reducing thermoelastic noise in gravitational-wave interferometers by flattening the light beams". In: *arXiv preprint gr-qc/0409075* (2004).

[48] GN Sharma, T Sundararajan, and S Singh Gautam. "Thermoelastic Damping Based Design, Sensitivity Study and Demonstration of a Functional Hybrid Gyroscope Resonator for High Quality Factor". In: *Gyroscopy and Navigation* 12.1 (2021), pp. 69–85.

[49] Gregory Harry, Timothy P Bodiya, and Riccardo DeSalvo. *Optical coatings and thermal noise in precision measurement*. Cambridge University Press, 2012.

[50] Elizabeth M Gretarsson and Andri M Gretarsson. "Three methods for characterizing thermo-optic noise in optical cavities". In: *Physical Review D* 98.12 (2018), p. 122004.

[51] George Gerald Stoney. "The tension of metallic films deposited by electrolysis". In: *Proceedings of the Royal Society of London. Series A, Containing Papers of a Mathematical and Physical Character* 82.553 (1909), pp. 172–175.

[52] Matthew R Abernathy et al. "Investigation of the Young's modulus and thermal expansion of amorphous titania-doped tantala films". In: *Applied Optics* 53.15 (2014), pp. 3196–3202.

[53] Tameson. *How Bimetallic Thermometers work*. 2021. URL: https://tameson.com/bimetallic-thermometer.html.

[54] Elisabetta Cesarini et al. "A "gentle" nodal suspension for measurements of the acoustic attenuation in materials". In: *The Review of scientific instruments* 80 (June 2009), p. 053904. DOI: 10.1063/1.3124800.

[55] G Vajente et al. "A high throughput instrument to measure mechanical losses in thin film coatings". In: *Review of Scientific Instruments* 88.7 (2017), p. 073901.

[56] M Granata et al. "Amorphous optical coatings of present gravitational-wave interferometers". In: *Classical and Quantum Gravity* 37.9 (Apr. 2020), p. 095004. DOI: 10.1088/1361-6382/ab77e9. URL: https://doi.org/10.1088%2F1361-6382%2Fab77e9.

[57] Diana Lumaca, Virgo Coating R&D Collaboration, et al. "Thermal noise reduction for future gravitational wave detectors". In: *Journal of Physics: Conference Series*. Vol. 1226. 1. IOP Publishing. 2019, p. 012023.

[58] JB Wachtman Jr et al. "Exponential temperature dependence of Young's modulus for several oxides". In: *Physical review* 122.6 (1961), p. 1754.

[59] Christian Schwarz et al. "Mechanical loss of calcium fluoride at cryogenic temperatures". In: *physica status solidi (a)* 208.12 (2011), pp. 2719–2723.

[60] Jurgen Kolbe et al. "Optical properties and damage thresholds of dielectric UV/VUV coatings deposited by conventional evaporation, IAD, and IBS". In: *Laser-Induced Damage in Optical Materials: 1991*. Vol. 1624. International Society for Optics and Photonics. 1992, pp. 221–235.

[61] Jurgen Kolbe and Harald Schink. "Optical losses of dielectric VUV-mirrors deposited by conventional evaporation, IAD, and IBS". In: *Thin Films for Optical Systems*. Vol. 1782. International Society for Optics and Photonics. 1993, pp. 435–446.

[62] Bo-Huei Liao et al. “Optical and mechanical properties of AlF 3 films produced by pulse magnetron sputtering of Al targets with CF 4/O 2 gas”. In: *Optical review* 16.4 (2009), pp. 505–510.

[63] Aiko Ode. “Ion beam sputtering of fluoride thin films for 193 nm applications”. In: *Applied optics* 53.4 (2014), A330–A333.

[64] K Yamamoto et al. “Mechanical loss of the reflective coating and fluorite at low temperature”. In: *Classical and Quantum Gravity* 21.5 (2004), S1075.

[65] *Laser Zentrum Hannover*. 2021. URL: https://www.lzh.de/de.

[66] Laboratoire des Matériaux Avancés. 2021. URL: http://lma.in2p3.fr/.

[67] KS Gilroy and WA Phillips. “An asymmetric double-well potential model for structural relaxation processes in amorphous materials”. In: *Philosophical Magazine B* 43.5 (1981), pp. 735–746.

[68] F Travasso et al. “Low-frequency internal friction in silica glass”. In: *EPL (Europhysics Letters)* 80.5 (2007), p. 50008.

[69] G Cagnoli et al. “Mode-dependent mechanical losses in disc resonators”. In: *Physics Letters A* 382.33 (2018), pp. 2165–2173.

[70] Ronny Nawrodt et al. “Investigation of mechanical losses of thin silicon flexures at low temperatures”. In: *Classical and Quantum Gravity* 30.11 (2013), p. 115008.

[71] Sheila Rowan et al. “Test mass materials for a new generation of gravitational wave detectors”. In: *Gravitational-Wave Detection*. Ed. by Peter Saulson and Adrian M. Cruise. Vol. 4856. International Society for Optics and Photonics. SPIE, 2003, pp. 292–297. DOI: 10.1117/12.459019. URL: https://doi.org/10.1117/12.459019.

[72] Trevor J Bright et al. “Infrared optical properties of amorphous and nanocrystalline Ta2O5 thin films”. In: *Journal of Applied Physics* 114.8 (2013), p. 083515.

[73] Gregory H Ogin. *Measurement of thermo-optic properties of thin film dielectric coatings*. California Institute of Technology, 2013.

[74] Ian H Malitson. “Interspecimen comparison of the refractive index of fused silica”. In: *Josa* 55.10 (1965), pp. 1205–1209.

[75] Kevin Luke et al. “Broadband mid-infrared frequency comb generation in a Si 3 N 4 microresonator”. In: *Optics letters* 40.21 (2015), pp. 4823–4826.

[76] M Evans et al. "Thermo-optic noise in coated mirrors for high-precision optical measurements". In: *Physical Review D* 78.10 (2008), p. 102003.

[77] MM Fejer et al. "Thermoelastic dissipation in inhomogeneous media: loss measurements and displacement noise in coated test masses for interferometric gravitational wave detectors". In: *Physical Review D* 70.8 (2004), p. 082003.

[78] G. Vajente. *How the loss angle is extracted from the Gentle Nodal Suspension measurements*. Tech. rep. LIGO-T1900554. Caltech, 2019.

[79] G. Vajente. *Bulk and Shear mechanical loss angles from Gentle Nodal Suspension measurements*. Tech. rep. LIGO-T1900567. Caltech, 2019.

[80] G. Vajente. *Convergence of COMSOL models of the C. Ri. Me. resonators*. Tech. rep. LIGO-T1900724-v1. Caltech, 2019.

[81] M. Bischi and G. Vajente. *Notes on COMSOL models for simulations of substrates not completely covered by a coating*. Tech. rep. LIGO-T1900882-v1. Caltech, 2019.